

ABSTRACT

Title of thesis: DROPLET DYNAMICS IN MICROFLUIDIC JUNCTIONS

Navadeep Boruah, Master of Science, 2012

Thesis directed by: Professor Panagiotis Dimitrakopoulos
Department of Chemical and Biomolecular Engineering

The dynamics of droplets in confined microfluidic geometries is a problem of fundamental interest as such flow conditions occur in multiphase flows in porous media, biological systems, microfluidics and material science applications. In this thesis, we investigate computationally the dynamics of naturally buoyant droplets, with constant surface tension, in cross-junctions and T-junctions constructed from square microfluidic channels. A three-dimensional fully-implicit interfacial spectral boundary element method is employed to compute the interfacial dynamics of the droplets in the junctions and investigate the problem physics for a wide range of flow rates, viscosity ratios and droplet sizes.

Our investigation reveals that as the flow rate or the droplet size increases, the droplets show a rich deformation behavior as they move inside the microfluidic devices. In the cross-junction, after obtaining a bullet-like shape before the flow intersection, the droplet become very slender inside the junction (to accommodate the intersecting flows), then it obtains an inverse-bullet shape as it exits the junction which reverts to a more pointed bullet-like shape far downstream. In the T-junction, the droplet obtains a skewed-bullet shape and a highly deformed slipper shape after entering the flows intersection. The viscosity ratio also has strong effects on the droplet deformation especially for high-viscosity droplets which do not have the time to accommodate the much slower deformation rate during their channel motion. Our results are in agreement with experimental findings, and provide physical insight on the confined droplet deformation.

DROPLET DYNAMICS IN MICROFLUIDIC JUNCTIONS

by

Navadeep Boruah

Thesis submitted to the Faculty of the Graduate School of the
University of Maryland, College Park in partial fulfillment
of the requirements for the degree of
Master of Science
2012

Advisory Committee:

Professor Panagiotis Dimitrakopoulos, Chair/Advisor
Professor Jeffery B. Klauda
Professor Kyu Yong Choi

© Copyright by
Navadeep Boruah
2012

Acknowledgements

I owe my sincere gratitude to all the people who have made this thesis possible. First of all, I would like to thank my advisor, Professor Panagiotis Dimitrakopoulos, for his guidance, help and tremendous support in my research during my Master's program and in my thesis preparation. I am also indebted to my labmate Sun Young Park, for all the help and suggestions on many occasions and in many ways. My thanks also to all my teachers at the University of Maryland, who made studying here such a wonderful experience.

A very special thanks to my friend and mentor Mr. Sourabh Bora who has been motivating me since my early days as an undergraduate student. Without his help, constant motivation and persuasions, graduate studies in the US would have remained a dream unfulfilled.

I would also like to take this opportunity to thank my friends Dhrubajyoti, Anurag and Shibu for all the support that they have provided me ever since I have known them.

I am also thankful to the staff of the Department of Chemical and Biomolecular Engineering for their kind assistance in myriad things in the last two years.

I owe my gratitude to my parents, Mr. Chandra Boruah and Mrs. Bharati Gogoi Boruah and my brother Mr. Nilotpal Boruah for having trust in me through all these years.

Acknowledgment is made to the Donors of the American Chemical Society Petroleum Research Fund for partial support of this research. Most computations were performed on multiprocessor computers provided by the Extreme Science and Engineering Discovery Environment (XSEDE) which is supported by the National Science Foundation.

Table of Contents

List of Figures	v
1 Introduction	1
1.1 Droplet motion in microfluidic channels	2
1.2 Review of past work	3
1.3 Overview of present research	4
2 Droplet dynamics in a microfluidic cross-junction	7
2.1 Introduction	7
2.2 Mathematical Formulation and Computational Method	9
2.2.1 Problem Description	9
2.2.2 Fluid Dynamics	11
2.3 Implicit Interfacial Spectral Boundary-Element Method	14
2.4 Results	17
2.4.1 Effect of flow rate	20
2.4.2 Effect of droplet size	31
2.4.3 Effect of viscosity ratio	42
2.5 Conclusion	55
3 Droplet dynamics in a microfluidic T-junction	58
3.1 Introduction	58
3.2 Mathematical Formulation and Computational Method	60
3.2.1 Problem Description	60
3.2.2 Fluid Dynamics	63
3.3 Implicit Interfacial Spectral Boundary-Element Method	65
3.4 Results	68
3.4.1 Effect of flow rate	71
3.4.2 Effect of droplet size	81
3.4.3 Effect of viscosity ratio	96

3.5 Conclusion	106
Bibliography	110

List of Figures

2.1	Schematic illustration of the geometry of cross-junction.	12
2.2	Three-dimensional figures of an undeformed droplet and the cross-junction used in our computations.	12
2.3	Three-dimensional shapes of a droplet (plotted row-wise) with $Ca = 0.4$, $\lambda = 0.2$, $a = 0.7$, $q = 0.5$ in a cross-junction, as viewed slightly askew from the $-y$ -axis at $x_c = -3.0, -1.5, -0.45, -0.03, 0.51, 1.23, 2.1, 3.83, 5.58, 7.27$	18
2.4	Droplet lengths along the flow direction as a function of the droplet centroid x_c for $\lambda = 0.2$, $a = 0.7$, $q = 0.5$ and capillary number $Ca = 0.01, 0.1, 0.2, 0.4, 0.6$. (a) Droplet length L_x . (b) Downstream droplet length L_x^d . (c) Upstream droplet length L_x^u	21
2.5	Droplet lengths along the y - and z -axes as a function of the droplet centroid x_c for $\lambda = 0.2$, $a = 0.7$, $q = 0.5$ and capillary number $Ca = 0.01, 0.1, 0.2, 0.4, 0.6$. (a) Droplet length along the y -axis $L_y/(2a)$. (b) Droplet length along the z -axis $L_z/(2a)$	23
2.6	Surface area of the droplet (scaled with its undisturbed value) S_d/S_d^0 as a function of the droplet centroid x_c for $\lambda = 0.2$, $a = 0.7$, $q = 0.5$ and capillary number $Ca = 0.01, 0.1, 0.2, 0.4, 0.6$	24
2.7	Curvatures of the downstream droplet tip as a function of the droplet centroid x_c for $\lambda = 0.2$, $a = 0.7$, $q = 0.5$ and capillary number $Ca = 0.01, 0.1, 0.2, 0.4, 0.6$. (a) Curvature of the droplet xz -profile \mathcal{C}_{xz}^d . (b) Curvature of the droplet xy -profile \mathcal{C}_{xy}^d . The curvatures are scaled with the curvature of the undisturbed spherical shape.	25
2.8	Curvatures of the upstream droplet tip as a function of the droplet centroid x_c for $\lambda = 0.2$, $a = 0.7$, $q = 0.5$ and capillary number, $Ca = 0.01, 0.1, 0.2, 0.4, 0.6$. (a) Curvature of the droplet xz -profile \mathcal{C}_{xz}^u . (b) Curvature of the droplet xy -profile \mathcal{C}_{xy}^u . The curvatures are scaled with the curvature of the undisturbed spherical shape.	27

2.9	Droplet velocity and additional pressure difference as a function of the droplet centroid x_c for $\lambda = 0.2$, $a = 0.7$, $q = 0.5$ and capillary number $Ca = 0.01, 0.1, 0.2, 0.4, 0.6$. (a) Droplet velocity U_x . (b) Additional pressure difference ΔP^+	29
2.10	Minimum distance h of the droplet interface from the $z = -l_z$ wall of the junction as a function of the droplet centroid x_c for $\lambda = 0.2$, $a = 0.7$, $q = 0.5$ and capillary number $Ca = 0.01, 0.1, 0.2, 0.4, 0.6$	30
2.11	Droplet lengths along the flow direction as a function of the droplet centroid for $\lambda = 0.2$, $Ca = 0.1$, $q = 0.5$ and droplet size $a = 0.5, 0.6, 0.7, 0.8, 0.9, 0.95$. (a) Droplet length $L_x/(2a)$. (b) Downstream droplet length L_x^d/a and (c) Upstream droplet length L_x^u/a	32
2.12	Droplet lengths along the y - and z -axes as a function of the droplet centroid x_c for $\lambda = 0.2$, $Ca = 0.1$, $q = 0.5$ and droplet size $a = 0.5, 0.6, 0.7, 0.8, 0.9, 0.95$. (a) Droplet length along the y -axis $L_y/2a$. (b) Droplet length along the z -axis $L_z/2a$	35
2.13	Surface area of the droplet (scaled with its undisturbed value) S_d/S_d^0 as a function of the droplet centroid x_c for $\lambda = 0.2$, $Ca = 0.1$, $q = 0.5$ and droplet size, $a = 0.5, 0.6, 0.7, 0.8, 0.9, 0.95$	37
2.14	Curvatures of downstream droplet tip as a function of the droplet centroid x_c for $\lambda = 0.2$, $Ca = 0.1$, $q = 0.5$ and droplet size $a = 0.5, 0.6, 0.7, 0.8, 0.9, 0.95$. (a) Curvature of the droplet xz -profile \mathcal{C}_{xz}^d . (b) Curvature of the droplet xy -profile \mathcal{C}_{xy}^d	38
2.15	Curvatures of the upstream droplet tip as a function of droplet centroid x_c for $\lambda = 0.2$, $Ca = 0.1$, $q = 0.5$ and droplet size $a = 0.5, 0.6, 0.7, 0.8, 0.9, 0.95$. (a) Curvature of the droplet xz -profile \mathcal{C}_{xz}^u . (b) Curvature of the droplet xy -profile \mathcal{C}_{xy}^u	39
2.16	Droplet velocity and additional pressure difference as a function of droplet centroid x_c for $\lambda = 0.2$, $Ca = 0.1$, $q = 0.5$ and droplet size $a = 0.5, 0.6, 0.7, 0.8, 0.9, 0.95$. (a) Droplet velocity U_x . (b) Additional pressure difference ΔP^+	41

2.17	Minimum distance h of the droplet interface from the $z = -l_z$ wall of the junction as a function of the droplet centroid for $\lambda = 0.2$, $Ca = 0.1$, $q = 0.5$ and droplet size $a = 0.5, 0.6, 0.7, 0.8, 0.9, 0.95$	43
2.18	Droplet lengths along the flow direction as a function of the droplet centroid x_c for $Ca = 0.1$, $a = 0.7$, $q = 0.5$ and viscosity ratio $\lambda = 0.01, 0.1, 0.5, 1.0, 10.0, 20.0$. (a) Droplet length $L_x/(2a)$. (b) Downstream droplet length L_x^d/a . (c) Upstream droplet length L_x^u/a	44
2.19	Droplet lengths along the y - and z -axes as a function of the droplet centroid x_c for $Ca = 0.1$, $a = 0.7$, $q = 0.5$ and viscosity ratio $\lambda = 0.01, 0.1, 0.5, 1.0, 10.0, 20.0$. (a) Droplet length along the y -axis $L_y/(2a)$. (b) Droplet length along the z -axis $L_z/(2a)$	47
2.20	Surface area of the droplet (scaled with its undisturbed value) S_d/S_d^0 a function of the droplet centroid x_c for $Ca = 0.1$, $a = 0.7$, $q = 0.5$ and viscosity ratio $\lambda = 0.01, 0.1, 0.5, 1.0, 10.0, 20.0$	48
2.21	Curvatures of the downstream droplet tip as a function of the droplet centroid x_c for $Ca = 0.1$, $a = 0.7$, $q = 0.5$ and viscosity ratio $\lambda = 0.01, 0.1, 0.5, 1.0, 10.0, 20.0$. (a) Curvature of the droplet xz -profile \mathcal{C}_{xz}^d . (b) Curvature of the droplet xy -profile \mathcal{C}_{xy}^d	50
2.22	Curvatures of the upstream droplet tip as a function of the droplet centroid x_c for $Ca = 0.1$, $a = 0.7$, $q = 0.5$ and viscosity ratio $\lambda = 0.01, 0.1, 0.5, 1.0, 10.0, 20.0$. (a) Curvature of the droplet xz -profile \mathcal{C}_{xz}^u . (b) Curvature of the droplet xy -profile \mathcal{C}_{xy}^u	51
2.23	Droplet velocity and additional pressure difference as a function of the droplet centroid x_c for $Ca = 0.1$, $a = 0.7$, $q = 0.5$ and viscosity ratio $\lambda = 0.01, 0.1, 0.5, 1.0, 10.0, 20.0$. (a) Droplet velocity U_x . (b) Additional pressure difference ΔP^+	53
2.24	Minimum distance h of the droplet interface from the $z = -l_z$ wall of the junction as a function of the droplet centroid for $Ca = 0.1$, $a = 0.7$, $q = 0.5$ and viscosity ratio $\lambda = 0.01, 0.1, 0.5, 1.0, 10.0, 20.0$	54

3.1	Schematic illustration of the geometry of T-junction.	62
3.2	Three-dimensional figures of an undeformed droplet and the T-junction used in our computations.	62
3.3	Three-dimensional shapes of a droplet (plotted row-wise) with $Ca =$ 0.4 , $\lambda = 0.2$, $a = 0.7$, $q = 0.5$ in a T-junction at $x_c = -3.0, -1.74,$ $-0.53, -0.37, 0.12, 0.49, 0.90, 1.34, 1.57, 2.26, 3.4, 4.5, 4.9.$	69
3.4	Droplet lengths along the flow direction as a function of the droplet centroid x_c for $\lambda = 0.2$, $a = 0.7$, $q = 0.5$ and capillary number $Ca =$ $0.01, 0.1, 0.2, 0.4.$ (a) Droplet length $L_x.$ (b) Downstream droplet length $L_x^d.$ (c) Upstream droplet length $L_x^u.$	72
3.5	Droplet lengths along the $y-$ and $z-$ axes as a function of the droplet centroid x_c for $\lambda = 0.2$, $a = 0.7$, $q = 0.5$ and capillary number $Ca = 0.01, 0.1, 0.2, 0.4.$ (a) Droplet length along the y -axis $L_y/(2a).$ (b) Droplet length along the z -axis $L_z/(2a).$	74
3.6	Surface area of the droplet (scaled with its undisturbed value) S_d/S_d^0 as a function of the droplet centroid x_c for $\lambda = 0.2$, $a = 0.7$, $q = 0.5$ and capillary number $Ca = 0.01, 0.1, 0.2, 0.4.$	76
3.7	Curvature of the xz -profile at the center of the downstream droplet tip (scaled with its undisturbed value) $C_{xz}^d/C_{xz,0}^d$ as a function of the droplet centroid x_c for $\lambda = 0.2$, $a = 0.7$, $q = 0.5$ and capillary number $Ca = 0.01, 0.1, 0.2, 0.4.$	77
3.8	Curvature of the xz -profile at the center of the upstream droplet rear (scaled with its undisturbed value) $C_{xz}^u/C_{xz,0}^u$ as a function of the droplet centroid x_c for $\lambda = 0.2$, $a = 0.7$, $q = 0.5$ and capillary number $Ca = 0.01, 0.1, 0.2, 0.4.$	79
3.9	Droplet velocities as a function of the droplet centroid x_c for $\lambda = 0.2,$ $a = 0.7$, $q = 0.5$ and capillary number $Ca = 0.01, 0.1, 0.2, 0.4.$ (a) Droplet velocity along the flow direction $U_x.$ (b) Droplet velocity along the z -axis $U_z.$	80

3.10	Minimum distance of the droplet interface, from the $z = -l_z$ wall of the junction, and droplet centroid position along the z -axis as a function of the droplet centroid x_c for $\lambda = 0.2$, $a = 0.7$, $q = 0.5$ and capillary number $Ca = 0.01, 0.1, 0.2, 0.4$. (a) Minimum distance h . (b) Droplet centroid position along the z -axis Z_c	82
3.11	Droplet lengths along the flow direction as a function of the droplet centroid for $\lambda = 0.2$, $Ca = 0.1$, $q = 0.5$ and droplet size $a = 0.5, 0.6, 0.7, 0.8, 0.9$. (a) Droplet length $L_x/(2a)$. (b) Downstream droplet length L_x^d/a and (c) Upstream droplet length L_x^u/a	84
3.12	Droplet lengths along the y - and z -axes as a function of the droplet centroid x_c for $\lambda = 0.2$, $Ca = 0.1$, $q = 0.5$ and droplet size $a = 0.5, 0.6, 0.7, 0.8, 0.9$. (a) Droplet lengths along the y -axis $L_y/2a$. (b) Droplet lengths along the z -axis $L_z/2a$	87
3.13	Surface area of the droplet (scaled with its undisturbed value) S_d/S_d^0 as a function of the droplet centroid x_c for $\lambda = 0.2$, $Ca = 0.1$, $q = 0.5$ and droplet size, $a = 0.5, 0.6, 0.7, 0.8, 0.9$	89
3.14	Curvature of xz -profile at the center of the downstream droplet tip (scaled with its undisturbed value) $\mathcal{C}_{xz}^d / \mathcal{C}_{xz,0}^d$ as a function of the droplet centroid x_c for $\lambda = 0.2$, $Ca = 0.1$, $q = 0.5$ and droplet size $a = 0.5, 0.6, 0.7, 0.8, 0.9$	90
3.15	Curvature of the xz -profile at the center of the upstream droplet rear (scaled with its undisturbed value) $\mathcal{C}_{xz}^u / \mathcal{C}_{xz,0}^u$ as a function of droplet centroid x_c for $\lambda = 0.2$, $Ca = 0.1$, $q = 0.5$ and droplet size $a = 0.5, 0.6, 0.7, 0.8, 0.9$	91
3.16	Droplet velocities as a function of droplet centroid x_c for $\lambda = 0.2$, $Ca = 0.1$, $q = 0.5$ and droplet size $a = 0.5, 0.6, 0.7, 0.8, 0.9$. (a) Droplet velocity along the flow direction U_x . (b) Droplet velocity along the z -axis U_z	93

3.17	Minimum distance of the droplet interface, from the $z = -l_z$ wall of the junction, and droplet centroid along z -axis as a function of the droplet centroid for $\lambda = 0.2$, $Ca = 0.1$, $q = 0.5$ and droplet size $a = 0.5, 0.6, 0.7, 0.8, 0.9$. (a) Minimum distance h . (b) Droplet centroid along z -axis Z_c	95
3.18	Droplet lengths along the flow direction as a function of the droplet centroid x_c for $Ca = 0.1$, $a = 0.7$, $q = 0.5$ and viscosity ratio $\lambda = 0.01, 0.1, 0.5, 1, 10, 20$. (a) Droplet length $L_x/(2a)$. (b) Downstream droplet length L_x^d/a . (c) Upstream droplet length L_x^u/a	97
3.19	Droplet lengths along the y - and z -axes as a function of the droplet centroid x_c for $Ca = 0.1$, $a = 0.7$, $q = 0.5$ and viscosity ratio $\lambda = 0.01, 0.1, 0.5, 1.0, 10.0, 20.0$. (a) Droplet length along the y -axis $L_y/(2a)$. (b) Droplet length along the z -axis $L_z/(2a)$	99
3.20	Surface area of the droplet (scaled with its undisturbed value) S_d/S_d^0 as a function of the droplet centroid x_c for $Ca = 0.1$, $a = 0.7$, $q = 0.5$ and viscosity ratio $\lambda = 0.01, 0.1, 0.5, 1.0, 10.0, 20.0$	101
3.21	Curvature of the xz -profile of the center of the downstream droplet tip (scaled with its undisturbed value) $\mathcal{C}_{xy}^d/\mathcal{C}_{xz,0}^d$ as a function of the droplet centroid x_c for $Ca = 0.1$, $a = 0.7$, $q = 0.5$ and viscosity ratio $\lambda = 0.01, 0.1, 0.5, 1, 10, 20$	102
3.22	Curvature of the xz -profile of the center of the upstream droplet rear (scaled with its undisturbed value) $\mathcal{C}_{xz}^u/\mathcal{C}_{xz,0}^u$ as a function of the droplet centroid x_c for $Ca = 0.1$, $a = 0.7$, $q = 0.5$ and viscosity ratio $\lambda = 0.01, 0.1, 0.5, 1.0, 10.0, 20.0$	104
3.23	Droplet velocities as a function of the droplet centroid x_c for $Ca = 0.1$, $a = 0.7$, $q = 0.5$ and viscosity ratio $\lambda = 0.01, 0.1, 0.5, 1.0, 10.0, 20.0$. (a) Droplet velocity along the flow direction U_x . (b) Droplet velocity along the z -axis U_z	105

3.24 Minimum distance h of the droplet interface, from the $z = -l_z$ wall of the junction, and droplet centroid along z -axis as a function of the droplet centroid for $Ca = 0.1$, $a = 0.7$, $q = 0.5$ and viscosity ratio $\lambda = 0.01, 0.1, 0.5, 1.0, 10.0, 20.0$. (a) Minimum distance h . (b) Droplet centroid along z -axis Z_c 107

Chapter 1

Introduction

In the present thesis we investigate computationally the dynamics of droplets in the intersecting flows of microfluidic junctions. In particular, we consider cross-junctions and T-junctions constructed from square microfluidic channels. The deformation and displacements of droplets in confined microfluidic geometries subjected to intersecting flows is a problem of considerable interest as such flow conditions occur in multi-phase flows in porous media and biological systems. In our study, we consider droplets with constant surface tension, which are naturally buoyant in the surrounding fluid of the microfluidic device. We closely investigate the problem physics for a wide range of capillary numbers Ca , viscosity ratios λ and droplet sizes a .

A three-dimensional fully-implicit interfacial spectral boundary element method is used to determine the droplet dynamics in the cross-junctions and T-junctions used in our computations. We emphasize that this is a challenging computational problem because it requires (i) a highly accurate stable numerical method to capture the interfacial evolution of the very deformed droplets at high flow rates and large droplet sizes, and the close interaction between droplet and solid surfaces of the microfluidic junctions, and (ii) an efficient algorithm for the complicated three-dimensional geometries of the microfluidic junctions. In this chapter, we provide a description of the motivation for our research, a review of the past and current research, as well as an overview of our research on droplet dynamics in microfluidic cross- and T-junctions, described in detail in the following two chapters.

1.1 Droplet motion in microfluidic channels

The study of the dynamics of droplets has been a topic of extensive research for several decades because they are encountered in a large number of physical and chemical processes [42, 43]. There have been extensive experimental, theoretical and computational studies on the behavior of droplets submerged in another fluid. The growing interest in manipulation of microfluidic droplets is because of its applications in numerous areas ranging from direct contact heat/mass exchangers [30], encapsulation of reactants with droplets acting as micro-reactors [39] and improved drug delivery methods [49, 4]. The research on droplets include studies on formation of droplets [46, 27, 50], droplet deformation [19, 31, 20], bursting [3], coalescence of droplets [33, 53], adherence to solid boundaries [12, 13, 14] and splitting of droplets [5, 7]. For a summary on the current research and applications of microfluidics, the reader is referred to the review articles by Baroud, Gallaire and Dangla [2] and Solvas and deMello [38].

Besides microfluidics, understanding the behavior of non-wetting droplets has great importance in other industrial processes. In lubrication processes, lubricants usually contain a small amount of immersed bubbles which alter the performance of journal bearings and squeezing film dampers [37]. In enhanced oil recovery, foam is generated within the underground porous media during the displacement of oil [34]. An accurate estimation of the wetting film thickness between droplets composing the foam and the pore wall is desired in order to accurately predict the percentage of recoverable oil. In coating processes, the wetting film thickness is also a direct measure of the load for coating the inner surface of monolithic channels [21, 22]. The physics of bubbles in microchannels is also essential in the operation design of fuel cells, e.g. the removal of CO_2 bubbles in the anode channel of a direct methanol fuel cell (DMFC) [28]. Understanding how bubbles/drops affect the flow resistance in microchannels is a concern for determining the pumping or energy requirement for portable microfluidic devices involving two-phase flows, such as in a direct methanol fuel cell [10].

1.2 Review of past work

Considerable progress has been made in understanding the deformation a single droplet in shear and extensional flows. Microfluidic cross-junctions are one most commonly used for the generation of uniformly sized droplets [50, 46]. In the past few decades there have been extensive studies on the splitting of droplets in a microfluidic cross-junction [9]. Tan *et al.* [41] designed a microfluidic cross-junction with an expanding downstream section to generate uniformly sized droplets at controlled rates, using flow rates of fluids to control the sizes of droplets generated. Liu *et al.* [27] studied the formation of droplets at very low capillary numbers in different microfluidic cross-junctions, constructed from rectangular channels of different aspect ratios, via Lattice-Boltzmann computations and found the importance of flow rates, capillary number and channel geometry. Cubaud [9] used two cross-junctions in series to experimentally study the formation of droplets of high viscosity fluid in the first junction and the subsequent deformation and breakup of the droplet formed in the second junction. He found the difference in velocity between the rear and the front of the droplets in the second junction to be the reason of the deformation and the subsequent breakup. Mulligan *et al.* investigated the scale-up of microfluidic droplet generation rate by developing a single microfluidic chip consisting of six flow-focusing devices in parallel [32]. Liu *et al.* reviewed interface tracking techniques commonly employed in the modeling of microfluidic droplets [26]. Dupin *et al.* used Lattice-Boltzmann computations to simulate a microfluidic flow focusing device [16]. A review of droplet dynamics in complex flows can be found in the review article by Cristini *et al.* [8].

Microfluidic T-junctions, along with cross-junctions, are one of the most commonly used devices for the production of uniformly sized droplets. T-junctions were first used by Thorsen *et al.* for formation of droplets [44]. Garstecki *et al.* identified a squeezing mechanism for the formation of drops for very low capillary numbers and provided scaling relationships to predict the size of droplets produced [17]. De Menech *et al.* used a phase field model to simulate the flow of two immiscible fluids

and identified three distinct regimes of droplet formation: squeezing, dripping and jetting [11]. Christopher *et al.* experimentally studied the effects of viscosity and channel width ratios on droplet breakup in a T-junction and developed a scaling model. There have been extensive studies on the formation and breakup of droplets in microfluidic T-junctions [1, 25]. The critical parameter in certain microfluidic applications is the shape of the particle being transported. In drug delivery applications the surface area and the local curvature of the particle affects the adsorption of drugs [4]. Parameters like velocity, local curvature, surface area etc. are direct functions of the shape of the droplet.

1.3 Overview of present research

Despite the plethora of studies, there is limited information available on the deformation of a single droplet without breakup in microfluidic junctions. This is in contrast to the current knowledge of droplet formation in microfluidic junctions [50, 46]. Gu *et al.* reviewed the progress in the formation and merging of droplets in two-phase flow microfluidics [18]. The goal of this current study is to develop a better understanding of the dynamics of droplets in a microfluidic junction without interfacial breaking.

To address this issue, we study the dynamics of a single droplet as it moves along a microfluidic cross-junction or T-junction. Our microfluidic junctions are constructed from square microfluidic channels. We release the naturally buoyant microfluidic droplets, smaller in size than the cross-sectional area of the square channels comprising the junction, in the centerline of the horizontal main channel of the junction, upstream of the flow intersection. A three-dimensional fully-implicit spectral boundary element algorithm is used to compute the droplet deformation and motion under Stokes flow conditions in the microfluidic junctions. We compute the interfacial dynamics of the droplets from the time of its release until it reaches well downstream the end of junctions. However, our main interest is on investigating the interfacial dynamics near to the zone where the flow intersection occurs

in the junctions. In our computations, both fluids are considered isothermal and Newtonian. We investigate the effects of flow rate, droplet size and viscosity ratio by determining the evolution of various geometric and physical parameters such as lengths, surface area and curvatures of the droplet as well its velocity and additional pressure difference due to the droplet presence.

We divide the discussion on the microfluidic cross-junctions and T-junctions in two different chapters. Since we want the chapters to be self-containing, there are some repetitions on the junction geometry and the employed computational method in each of these chapters. Thus, each chapter discusses the mathematical formulation of the problem, the junction geometry, the computational method used and the results obtained from our computations in detail.

In chapter 2, we investigate computationally the dynamics of a droplet in the intersecting flows of a microfluidic cross-junction device. Particularly, we consider droplets with constant surface tension which are naturally buoyant in the surrounding fluid, and have size smaller than the cross-section of the square channels comprising the cross-junction. Our work shows that droplet dynamics in the cross-junction depends strongly on the flow rate in the channels, droplet size and viscosity ratio. As the flow rate or the droplet size increases, the droplets show a rich deformation behavior as it moves inside the microfluidic device. After obtaining a bullet-like shape before the cross-junction, the droplet become very slender inside the junction (to accommodate the intersecting flows), then it obtains an inverse-bullet shape as it exits the cross-junction which reverts to a more pointed bullet-like shape far downstream the cross-junction (due to the combined flow rates of all intersecting channels). The viscosity ratio has also strong effects on the droplet deformation. Increasing the droplet viscosity from small values up to $\lambda = O(1)$, the droplet deformation increases monotonically owing to the higher inner hydrodynamic forces. However, for high-viscosity droplets with $\lambda = O(10)$, the droplet deformation decreases significantly inside the cross-junction because the droplet does not have the time to accomodate the much slower deformation rate at high λ as it moves fast inside the microfluidic device.

In chapter 3, we investigate computationally the dynamics of a naturally buoyant droplet with constant surface tension in the intersecting flows of a microfluidic T-junction device. Our work shows that droplet dynamics in the T-junction depends strongly on the flow rate in the channels, droplet size and viscosity ratio. As the flow rate or the droplet size increases, the droplets show a rich deformation behavior as it moves inside the microfluidic device. After obtaining a bullet-like shape before the T-junction, the droplet takes the shape of a bullet skewed to one side (to accommodate the intersecting flow), and then it obtains a slipper shape with a very pointed rear (skewed to one side) as it exits the flow intersection of the T-junction. Further downstream, the T-junction the droplet tries to regain its shape and the rear of the slipper shaped droplet becomes less pointed and finally exits the junction. The viscosity ratio has strong effects on the droplet deformation. Increasing the droplet viscosity from small values up to $\lambda = O(1)$, the droplet deformation increases monotonically owing to the higher inner hydrodynamic forces. However, for high-viscosity droplets with $\lambda = O(10)$, the droplet deformation decreases significantly inside the T-junction because the droplet does not have the time to accommodate the much slower deformation rate at high λ as it moves fast inside the microfluidic device.

Chapter 2

Droplet dynamics in a microfluidic cross-junction

2.1 Introduction

The study of the dynamics of droplets has been a topic of extensive research for several decades because they are encountered in a large number of physical and chemical processes [42, 43]. There have been extensive experimental, theoretical and computational studies on the behavior of droplets submerged in another fluid. The growing interest in manipulation of microfluidic droplets is because of its applications in numerous areas ranging from direct contact heat/mass exchangers [30], encapsulation of reactants with droplets acting as micro-reactors [39] and improved drug delivery methods [49, 4]. The research on droplets include studies on formation of droplets [46, 27, 50], droplet deformation [19, 31, 20], bursting [3], coalescence of droplets [33, 53], adherence to solid boundaries [12, 13, 14] and splitting of droplets [5, 7]. For a summary on the current research and applications of microfluidics, the reader is referred to the review articles by Baroud, Gallaire and Dangla [2] and Solvas and deMello [38].

Besides microfluidics, understanding the behavior of non-wetting droplets has great importance in other industrial processes. In lubrication processes, lubricants usually contain a small amount of immersed bubbles which alter the performance of journal bearings and squeezing film dampers [37]. In enhanced oil recovery, foam is generated within the underground porous media during the displacement of oil [34]. An accurate estimation of the wetting film thickness between droplets composing the foam and the pore wall is desired in order to accurately predict the percentage

of recoverable oil. In coating processes, the wetting film thickness is also a direct measure of the load for coating the inner surface of monolithic channels [21, 22]. The physics of bubbles in microchannels is also essential in the operation design of fuel cells, e.g. the removal of CO_2 bubbles in the anode channel of a direct methanol fuel cell (DMFC) [28]. Understanding how bubbles/drops affect the flow resistance in microchannels is a concern for determining the pumping or energy requirement for portable microfluidic devices involving two-phase flows, such as in a direct methanol fuel cell [10].

Microfluidic cross-junctions, along with T-junctions, are most commonly used for the generation of uniformly sized droplets [50, 46]. Tan *et al.* [41] designed a microfluidic cross-junction with an expanding downstream section to generate uniformly sized droplets at controlled rates, using flow rates of fluids to control the sizes of droplets generated. Liu *et al.* [27] studied the formation of droplets at very low capillary numbers in different microfluidic cross-junctions, constructed from rectangular channels of different aspect ratios, via Lattice-Boltzmann computations and found the importance of flow rates, capillary number and channel geometry. Cubaud [9] used two cross-junctions in series to experimentally study the formation of droplets of high viscosity fluid in the first junction and the subsequent deformation and breakup of the droplet formed in the second junction. He found the difference in velocity between the rear and the front of the droplets in the second junction to be the reason of the deformation and the subsequent breakup. Mulligan *et al.* investigated the scale-up of microfluidic droplet generation rate by developing a single microfluidic chip consisting of six flow-focusing devices in parallel [32]. Liu *et al.* reviewed interface tracking techniques commonly employed in the modeling of microfluidic droplets [26].

The deformation and displacements of droplets in confined microfluidic geometries when subjected to intersecting flows is a problem of considerable interest as such flow conditions occur in multi-phase flows in porous media and biological systems. Considerable progress has been made in understanding the deformation a single droplet in shear and extensional flows. In the past few decades there have

been extensive studies on the splitting of droplets in a microfluidic cross-junction [9]. Dupin *et al.* used Lattice-Boltzmann computations to simulate a microfluidic flow focusing device [16]. A review of droplet dynamics in complex flows can be found in the review article by Cristini *et al.* [8]. However, there is very limited information available on the deformation of a single droplet without breakup in a microfluidic junction. This is in contrast to the current knowledge of droplet formation in cross-junctions [50, 46]. Gu *et al.* reviewed the progress in the formation and merging of droplets in two-phase flow microfluidics [18]. The goal of this current study is to develop a better understanding of the dynamics of droplets in a cross-junction without interfacial breaking.

To address this issue, we study the dynamics of a single droplet moving along the centerline of a microfluidic cross-junction. A three-dimensional spectral boundary element algorithm is used to compute the droplet deformation and motion under Stokes flow conditions in a microfluidic cross-junction. We provide a detailed discussion of the junction geometry used in our computations in section 2.2.1. The mathematical formulation of the problem and the boundary conditions are discussed in section 2.2.2. The implicit interfacial spectral boundary-element method used in our computations is discussed in detail in section 2.3. We discuss the results obtained from our numerical calculations in section 2.4. In particular, we study the effects of flow rate, droplet size and viscosity ratio in three different subsections. A summary of our results is presented in section 2.5.

2.2 Mathematical Formulation and Computational Method

2.2.1 Problem Description

A schematic diagram of the cross-junction employed in this work is shown in figure 2.1. The cross-junction is constructed from intersecting square microfluidic channels. To facilitate our results description, we imagine that the main channel is horizontal, as illustrated in figure 2.1. Thus the flow direction (*i.e.*, the x -axis) corresponds to the channel's or droplet's length, the z -direction will be referred as

height while the y -direction will be referred as width (of the channel or the droplet). Seeing the droplet from the positive y -axis, positive z -axis or negative x -axis, represents a front view, a top view or an upstream view, respectively. In addition, we adopt the standard definition of geometric shapes (polygons). Thus we call the droplet's rear edge as convex when the radius of curvature at the middle of the rear edge points inside the capsule (*i.e.*, the local curvature is positive); in the opposite case the edge shape is concave. In general, the half length l_x of the horizontal main channel of the junction along the x -axis is 9 units. The half lengths of the square cross-section of the main channel, along the y and z -axes are l_y and l_z respectively, with $l_y = l_z = 1$. The length of the vertical branch channels along the positive and negative z -axis are four units each. The origin of the system is placed at the center of the junction.

The droplet (fluid 1) with a density ρ_1 and viscosity $\lambda\mu$ is naturally buoyant in the surrounding fluid (fluid 2) with density ρ_2 and viscosity μ , as $\rho_1 = \rho_2$. The surface tension γ is assumed to be constant throughout the surface of the droplet. The undeformed spherical droplet, at the start of our computations, has a radius a with volume $V = \frac{4}{3}\pi a^3$. The surrounding fluid flows in to the junction towards the junction center through the square cross sections at $-x$, $-z$ and $+z$ -axes. The incoming flow of the surrounding fluid through the square cross sections at $-x$, upstream of the droplet is the undisturbed flow of fluid through a square channel with an average velocity of \mathcal{U} . The flow of the fluid coming in through the square cross sections of the vertical branch channels along the $+z$ and $-z$ axes is a fraction q of the fluid flow through the main channel of the junction, *i.e.*, the average velocity of the fluid through each of the vertical channels is $q\mathcal{U}$. At the start of our computations, the spherical droplet is placed inside the horizontal channel upstream of the flow intersection of the junction. Due to the symmetry of the flow and the system, the droplet velocity in the direction of the y - and z -axes is zero. As the droplet deforms, it moves along the x -axis which is the center-line of the junction. Due to the presence of intersecting flows in the junctions the deformation varies by a great margin to that of deformation of a single droplet in a straight channel, under

similar external shear and other physical conditions.

The major parameters of interest in this study are the strength of flow rate in the horizontal main channel, viscosity ratio and the size of droplets. Figure 2.2(a) shows the three-dimensional figure of an undeformed droplet while figure 2.2(b) shows a three-dimensional view of a cross-junction with the $-y$ elements removed.

2.2.2 Fluid Dynamics

Due to the very small length scales involved with droplet flow in microfluidics junctions, the Reynolds number is very small and the inertial terms in the Navier-Stokes equations can be neglected. The flow is governed by Stokes equations

$$\nabla \cdot \boldsymbol{\sigma} \equiv -\nabla p + \mu \nabla^2 \mathbf{u} = 0 \quad (2.1)$$

and the continuity equation

$$\nabla \cdot \mathbf{u} = 0 \quad (2.2)$$

where $\boldsymbol{\sigma}$ is the stress tensor, p is the dynamic pressure and \mathbf{u} is the velocity vector.

In this study, the system surface S_B consists of droplet surface S_d , the solid surface of the junction S_s , the fluid surfaces S_f of the junction's inlets and the outlet. At the droplet surface the velocity is continuous and there is an interfacial stress jump owing to the surface tension. As the density of both fluids are same, the contribution of gravity to the interfacial stress jump is zero and thus the boundary conditions on the droplet surface are,

$$\mathbf{u}_1 = \mathbf{u}_2 \quad \text{and} \quad \Delta \mathbf{f} \equiv \mathbf{f}_2 - \mathbf{f}_1 = \gamma \nabla \cdot \mathbf{n} \quad (2.3)$$

Here the subscripts designate quantities related to the fluids 1 and 2 respectively, while \mathbf{n} is the unit normal pointing from the droplet interface into fluid 2. The boundary conditions on the rest surfaces are,

$$\mathbf{u} = 0 \quad \text{on the solid boundary } S_s, \quad (2.4)$$

$$\mathbf{u} = \mathbf{u}^\infty \quad (2.5)$$

where \mathbf{u}^∞ is the undisturbed channel velocity far from the droplet.

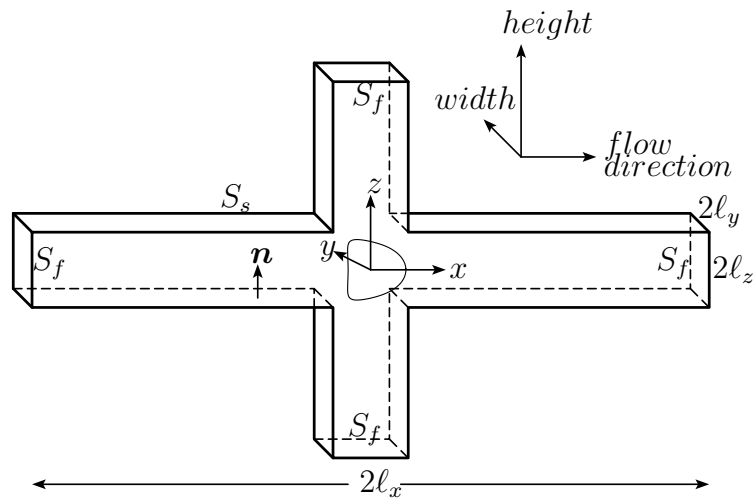


Figure 2.1: Schematic illustration of the geometry of cross-junction.

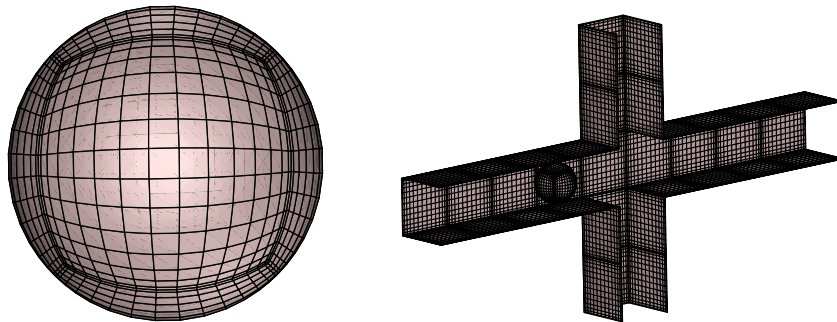


Figure 2.2: Three-dimensional figures of an undeformed droplet and the cross-junction used in our computations.

The undisturbed velocity profile for flow through a rectangular channel along x -axis, far from the droplet, can be found in the book by Yih [51], which is,

$$\frac{u^\infty(x)}{\Upsilon} = (l_z^2 - z^2) + \sum_{m=1}^{\infty} B_m \cosh\left(\frac{b_m y}{l_z}\right) \cos\left(\frac{b_m z}{l_z}\right), \quad (2.6)$$

where

$$\Upsilon = -\frac{1}{2\mu}, \quad b_m = \frac{(2m-1)\pi}{2}, \quad \text{and} \quad B_m = \frac{(-1)^m 4l_z^2}{b_m^3 \cosh\left(\frac{b_m l_y}{l_z}\right)} \quad (2.7)$$

while p is the dynamic pressure. The volumetric flow rate Q can be obtained by integrating over the cross-section, which is,

$$\frac{Q}{\Upsilon} = \frac{8l_y l_z^3}{3} + \sum_{m=1}^{\infty} B_m \left(\frac{2l_z}{b_m}\right)^2 \sinh\left(\frac{b_m l_y}{l_z}\right) \sin(b_m) \quad (2.8)$$

In our study, the incoming flows through each of the vertical branch channels is half as strong as the flow through the main horizontal channel. The velocity profile from the main channel is copied to the branch channels and scaled after accounting for the direction of flow. Far from the droplet, the average velocity of the undisturbed flow is $\mathcal{U} = Q/(l_y l_z)$, while the maximum undisturbed velocity at the centerline of the square channel is $\mathcal{U}_{max}/\mathcal{U} \approx 2.096$.

In this study, if no scale is present, the horizontal channel's half-height l_z is used as the length scale, the velocity is scaled with the average undisturbed velocity \mathcal{U} , and thus time is scaled with $\tau_f = l_z/\mathcal{U}$. In addition the pressure is scaled with $\Pi = \mu\mathcal{U}/l_z$.

Based on standard boundary integral formulation, the velocity at a point \mathbf{x}_0 on the system surface S_B may be expressed as a surface integral of the force vector $\mathbf{f} = \mathbf{n} \cdot \boldsymbol{\sigma}$ and the velocity \mathbf{u} over all points \mathbf{x} on the boundary S_B ,

$$\begin{aligned} \Omega \mathbf{u}(\mathbf{x}_0) = & - \int_{S_c} [\mathbf{S} \cdot (\Delta \mathbf{f} - \mu(1-\lambda)\mathbf{T} \cdot \mathbf{u} \cdot \mathbf{n})](\mathbf{x}) dS \\ & - \int_{S_s \cup S_f} (\mathbf{S} \cdot \mathbf{f} - \mu \mathbf{T} \cdot \mathbf{u} \cdot \mathbf{n})(\mathbf{x}) dS \end{aligned} \quad (2.9)$$

where the coefficient Ω takes values $4\pi\mu(1 + \lambda)$ and $4\pi\mu$ for points \mathbf{x}_0 on the surfaces S_d and $S_s \cup S_f$ respectively. The tensors \mathbf{S} and \mathbf{T} are the fundamental solutions for the velocity and stress for the three-dimensional Stokes equations, i.e., known functions of the system surface S_B [13]. More details on the definition of all physical variables employed in this work may be found in the article by Kuriakose and Dimitrakopoulos on the capsule motion inside a square microfluidic channel [23].

2.3 Implicit Interfacial Spectral Boundary-Element Method

The boundary integral equation, eq.(2.9), was solved using our three-dimensional fully-implicit interfacial spectral boundary-element method. The boundary is divided into a number N_E of surface elements, each of which is parametrized by variables η and ξ on a square domain of $[-1, 1]^2$. The geometry and physical variables are discretized using Lagrangian interpolation in terms of these parametric variables. The number N_B of basis points (η_i, ξ_i) chosen for interpolation are zeros of orthogonal polynomial. Any point \mathbf{x} on the geometry can be represented by

$$\mathbf{x}(\xi, \eta) = \sum_{i=1}^{N_B} \sum_{j=1}^{N_B} \mathbf{x}(\xi_i, \eta_i) h_i(\xi) h_j(\eta) \quad (2.10)$$

Similarly the physical variables \mathbf{u} and \mathbf{f} can be interpolated at any point \mathbf{x} from their values at the basis points.

Two types of points are used in solving the boundary integral equation by our spectral element method, the collocation points \mathbf{x}_0 where the equation is required to be satisfied and the basis points \mathbf{x} where the physical variables \mathbf{u} and \mathbf{f} are specified. The collocation points \mathbf{x}_0 are of Legendre-Gauss quadrature where the points lie on the interior of the spectral elements. Thus, the boundary integral equation is valid even at corners of singular elements. The basis points \mathbf{x} are of Legendre-Gauss-Lobatto quadrature and thus the physical variables are defined in the interior and edges of the spectral elements. Further details on the discretization of system surfaces can be found in these earlier papers [47, 15].

The transformation of the Stokes equations into boundary integral equations and solution by an explicit time integration method has been a common method

to determine the droplet shape as a function of time since the pioneering work of Acrivos and coworkers [52, 36]. This results in a great reduction in computational time as a three-dimensional problem can be described and solved using only two curvilinear coordinates. However, the explicit time integration requires a time step smaller than any time scale (numerical and physical) appearing in the problem. To ensure stability the time step employed has to satisfy the following condition,

$$\Delta t < O(Ca \Delta x_{min}) \quad (2.11)$$

where Δx_{min} is the minimum grid spacing in the computational problem [35, 54]. Dimitrakopoulos developed an efficient, fully-implicit time-integration algorithm for interfacial dynamics in Stokes flow to avoid the computational cost associated with small time steps [15]. This method is based on a mathematically rigorous combination of implicit schemes with the Jacobian-free three-dimensional Newton method developed by Dimitrakopoulos and Higdon [13]. Both multi-step (one-stage) implicit formulae (e.g. Euler and backward differentiation schemes) and multi-stage diagonally implicit Runge-Kutta schemes are employed. By the combination of the an implicit scheme with the Newton method, the interfacial algorithm preserves the stability properties of the corresponding implicit formula, and hence permits the use of very large time steps. In addition, sufficient accuracy can be easily achieved, even with larger time steps, by employing high-order implicit schemes. In this work we use a third-order diagonally implicit Runge-Kutta scheme (DIRK3) with a time step $\Delta t = 10^{-2}$. Owing to the fully-implicit nature of our algorithm and the high-order DIRK3 scheme, even a larger time step $\Delta t = O(10^{-1})$ produces accurate results without causing interfacial breaking.

By combining the implicit interfacial method with the spectral boundary-element algorithm, the resulting algorithm exploits all the benefits of the spectral methods, i.e., high-order interpolation with exponential convergence and numerical stability with increasing number of spectral points, along with the versatility of the boundary-element method, i.e., the ability to handle the most complicated geometries. In addition, it is not affected by the disadvantage of the spectral methods

used in volume discretization; namely the requirement to deal with dense systems, because in boundary-integral formulations the resulting systems are always dense, independent of the form of discretization. We note that the exponential convergence in the numerical accuracy is evident at both the properties of a given shape, such as the interfacial curvature, and the dynamic evolution of the interfacial shape. For more details the reader is directed to the article by Dimitrakopoulos [15].

In our study, the horizontal main channel of the cross-junction is divided into nine rows with four rows upstream and downstream of the junction. Each of the vertical branch channels are two-rows long. Each row of the channels are represented by four surface elements, with one element representing a side of the row. Thus the solid walls of the cross-junction are divided into fifty elements. In addition the four fluid surfaces for entrance and exit of fluids into the channel are represented by one element each. The droplet surface is divided in a minimum of six elements by cube projection, with each element corresponding to a side of the cube. Our method is also capable of generating more surface elements on the droplet surface and more than one elements per row for each channel side. In most of our computations, we have used ten surface elements for capturing the droplet shape. However, for handling complex shapes of the deformed droplets for high Ca we have used up to 22 surface elements with progressive splitting of an element at the tip of the droplet into five elements. Such discretizations are not needed in most of the cases as the method is accurate, as shown from our convergence runs.

In most of our computations, we utilized $N_B = 8$ basis points on each element. As we have N_E number of surface elements and N_B^2 points per spectral elements, we finally have a system of $3N_EN_B^2$ algebraic equations. For verification of accuracy of our results, we performed some runs with $N_B = 10$ basis points for moderate and high Ca and high droplet sizes a . The convergence runs showed that $N_B = 8$ is sufficient enough to capture the shape of the deformed droplets except for the cases with large Ca ($Ca = 0.4, 0.6$).

In all our computations carried out in this chapter, we exploited two symmetry levels, $y = 0$ and $z = 0$. Exploiting these symmetries reduce the memory

requirements for storage of the system by a factor of 4^2 , the computational time for calculating the system matrices by a factor of 2^2 and the solution time via direct system solvers by factor of 8^2 .

2.4 Results

The results obtained from the numerical computations are discussed in this section. The study covers a wide range of flow rates, viscosity ratio and droplet size. The computations are started with a spherical droplet which deforms as it moves downstream. In our computations, we fix any two of Ca , λ , a at $Ca = 0.1$, $\lambda = 0.2$, $a = 0.7$ and vary the third one over a wide range to study its effects on droplet deformation. At the beginning of all computations, the droplet is placed at the center of the main channel at $x_c = -3.0$ and starts moving downstream due to flow initiation. We compute the droplet dynamics until the droplet centroid reaches $x_c = 8.0$. However, we plot the results of our computations only when the droplet centroid is in the range of $x_c = [-3.0, 6.0]$ as our main focus is on the dynamics of the droplet near the center of the junction where flow intersection occurs. Also we plot the results as a function of the droplet centroid x_c .

Three-dimensional shapes of a droplet at different locations x_c are shown in figure 2.3. The three-dimensional views presented here were derived from the actual spectral grid by spectrally interpolating to $N_B = 14-16$. The first shape shows the undeformed droplet at the start of our computation with its centroid at $x_c = -3.0$. After the start of computation, the droplet starts flowing downstream and deforms due to the hydrodynamic forces acting on it. The droplet assumes a bullet shape with a pointed downstream tip and a flattened rear, as seen in the second shape of figure 2.3, while still upstream of the zone of flow intersection. The droplet takes the shape of a bullet as it tries to balance the hydrodynamic forces and the surface tension forces. This can be explained by putting an observer at the center of the droplet, assuming a static frame of reference for the observer. In this case, the fluid is flowing upstream in the junction. With a spherical droplet the net surface tension

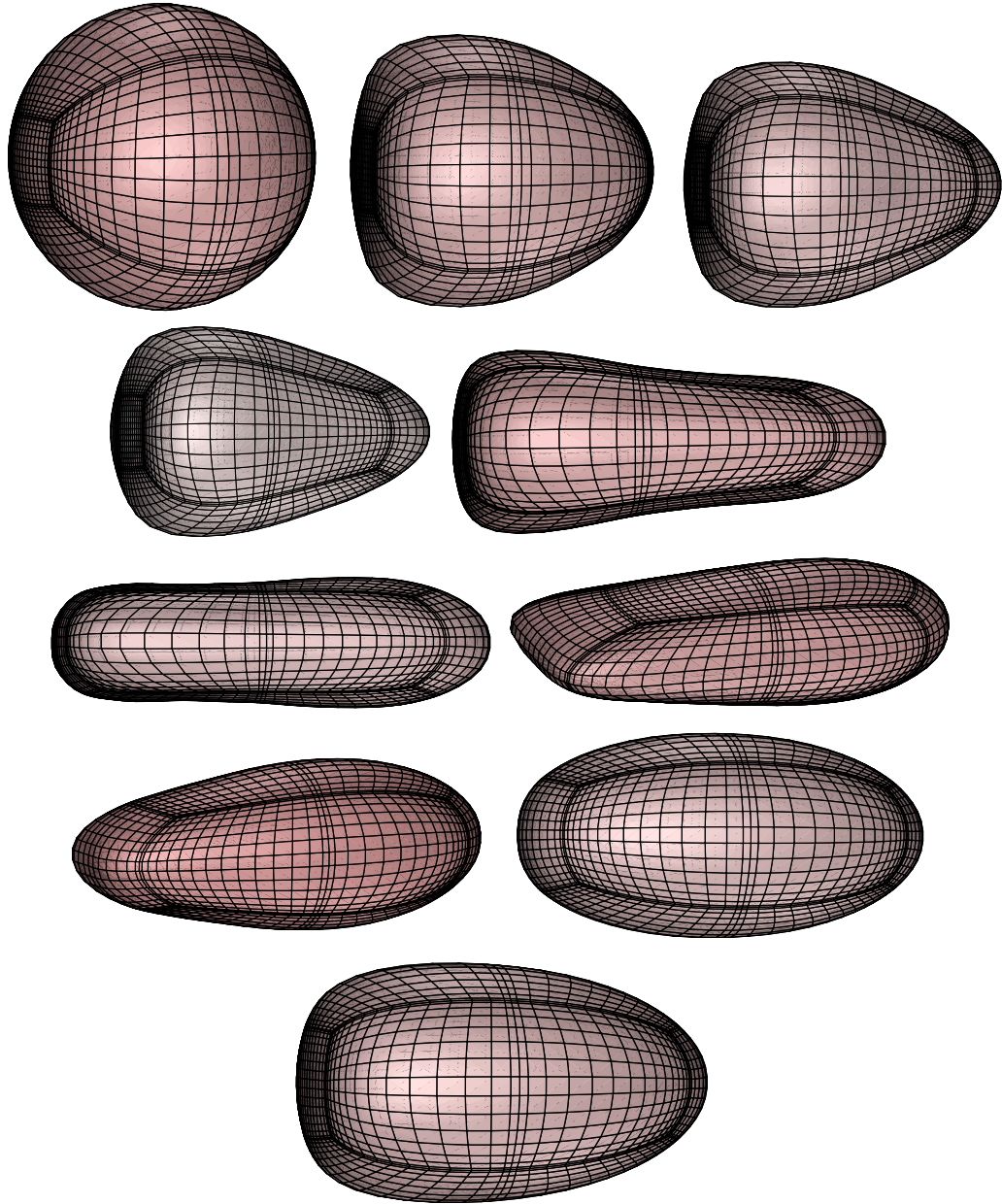


Figure 2.3: Three-dimensional shapes of a droplet (plotted row-wise) with $Ca = 0.4$, $\lambda = 0.2$, $a = 0.7$, $q = 0.5$ in a cross-junction, as viewed slightly askew from the $-y$ -axis at $x_c = -3.0, -1.5, -0.45, -0.03, 0.51, 1.23, 2.1, 3.83, 5.58, 7.27$.

force is zero. The surface tension force acting at a point on the droplet surface is inversely proportional to its radius of curvature and can be written as

$$F_\gamma \sim \frac{\gamma}{R} \quad (2.12)$$

where R is the radius of curvature of the point on the droplet. As the tip of the droplet becomes pointed and the rear becomes flatter, there is a net surface tension force on the droplet

$$F_\gamma \sim \gamma \left(\frac{1}{R_1} - \frac{1}{R_2} \right) \quad (2.13)$$

where R_1 and R_2 are the radius of curvatures of the center of the tip and the rear of the droplet. This quantity is positive as R_1 is smaller than R_2 .

As the tip of the droplet enters the zone of flow intersection, its tip becomes more pointed and the rear flatter as the droplet experiences a stronger hydrodynamic force due to increased flow rate coming in through the vertical branch channels. This can be observed in the third and fourth shapes in figure 2.3. As the droplet becomes more pointed, its centroid moves further towards the rear due to the presence of the long pointed tip and the short flattened rear. When the rear of the droplet is in the zone of flow intersection, with the downstream tip just outside of it, the droplet becomes very slender with a very pointed tip and a very flattened rear, as shown in the fifth shape of figure 2.3. As the droplet moves further downstream, with its tip now well outside the flow intersection while the rear is still in the flow intersection, the rear of the droplet becomes very slender while downstream tip of the droplet tries to regain its original shape. With this, now the droplet centroid moves towards the downstream tip. This shape can be seen in the sixth shape in figure 2.3. When the rear of the droplet reaches very close to the end of the flow intersection, it becomes very flat and thin with a concave shape, to accommodate the flow coming in through the vertical branch channels. The concave rear appears as the surface tension forces try to balance the even stronger hydrodynamic forces, since now the radius of curvature of the rear becomes negative and thus the surface tension forces on the droplet become

$$F_\gamma \sim \gamma \left(\frac{1}{R_1} + \frac{1}{R_2} \right) \quad (2.14)$$

After the droplet exits the flow intersection downstream, its rear starts regaining the flattened shape, as can be seen in the sixth shape of figure 2.3. The elongation of the droplet is at its maximum slightly downstream of the center of the junction. As the droplet moves further downstream, the droplet gradually regains its bullet shape, though longer than its bullet shape upstream of the junction, due to higher flow rate, and finally exits the junction.

2.4.1 Effect of flow rate

In this section, we collect our computational results studying the effects of varying flow rates in the horizontal main channel. The flow rate in the vertical branch channels is maintained constant at $q = 0.5$ in this series of computations. A spherical droplet with viscosity ratio $\lambda = 0.2$ and size $a = 0.7$ is placed upstream of the junction at $x_c = -3.0$ and the capillary number Ca varies in the range $[0.01-0.6]$. From our computations we found that the droplet deformation depends strongly on Ca with an increase in length and a decrease in its width.

Figure 2.4 shows the droplet lengths L_x along the flow direction as a function of the droplet centroid position x_c . It is observed from figure 2.4(a) that the total length of the droplet L_x increases monotonically with an increase in flow rate. At first, the length L_x increases slowly in the main upstream channel followed by a sharp increase as the droplet enters the flow intersection. L_x reaches a maximum after the droplet centroid x_c goes past the flow intersection and then starts decreasing in the downstream horizontal channel. For the cases with low flow rates, L_x decreases to a steady state after crossing the flow intersection. This is similar to droplet deformation reaching a steady state in low Reynold's number flows in a straight square channel [24, 48]. Lac *et al.*[24], in their study of droplets in a circular capillary, found that beyond a critical capillary number droplets cannot attain steady state shapes, owing to capillary instability. We also observed from our computations that for high Ca , L_x does not reach steady state. In addition, for the range of Ca studied in this chapter, none of the droplets break inside the junction channel.

We also divide the total droplet length L_x into two components, the upstream

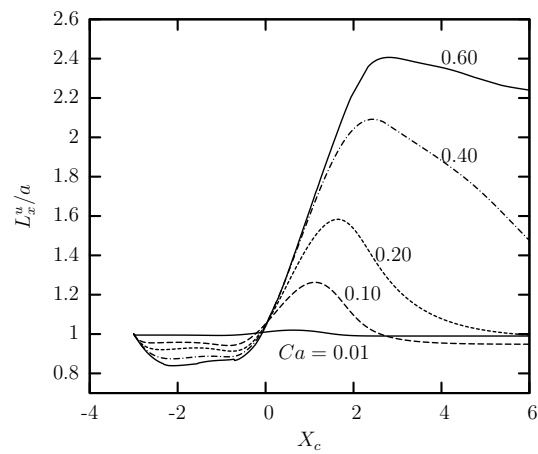
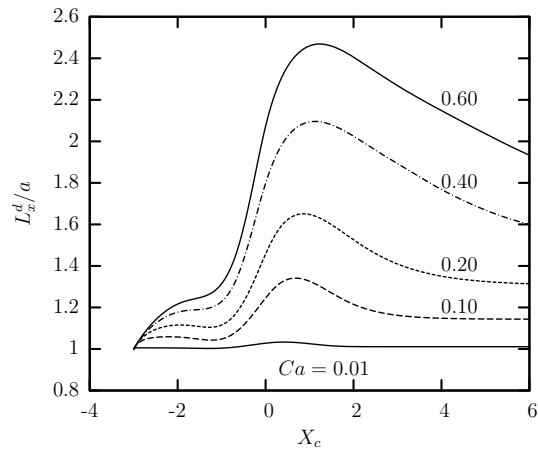
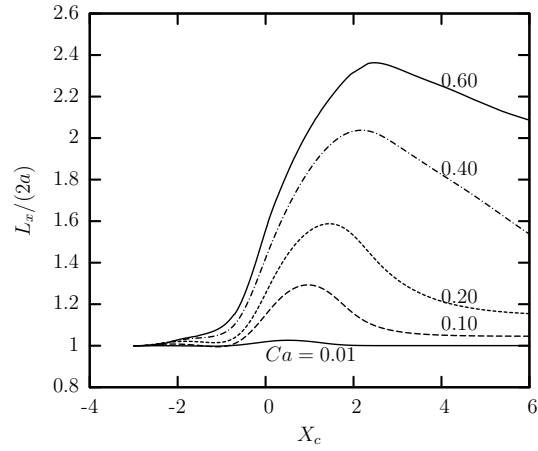


Figure 2.4: Droplet lengths along the flow direction as a function of the droplet centroid x_c for $\lambda = 0.2$, $a = 0.7$, $q = 0.5$ and capillary number $Ca = 0.01, 0.1, 0.2, 0.4, 0.6$. (a) Droplet length L_x . (b) Downstream droplet length L_x^d . (c) Upstream droplet length L_x^u .

and downstream droplet lengths, L_x^u and L_x^d , (calculated from the droplet centroid x_c to the rear and front tips of the droplet respectively), and plot them separately in figure 2.4(b, c) as a function of the droplet centroid x_c . It is observed that before the droplet centroid crosses the center of the cross-junction, they exhibit different behavior, while their behavior after that is similar. The upstream droplet length L_x^u at first decreases then starts increasing till it reaches a maximum. This is because of the appearance of a flattened rear and a pointed tip, as shown in figure 2.3, which cause the droplet's centroid to move backwards. The downstream length of the droplet L_x^d increases, at first slowly and then rapidly till it reaches a maximum. This can be attributed to the evolution of the pointed tip and the lengthening due to increased flow through the vertical branch channels. After reaching a maximum, both L_x^u and L_x^d decrease, and reach a steady state for low Ca .

In figure 2.5 (a) and (b) we plot L_y and L_z *i.e.*, the droplet lengths along y - and z -axes respectively as a function of droplet centroid x_c . L_y and L_z both decrease with an increase in flow rate as a result of the droplet becoming thinner and longer to enable the fluid to flow through the channel. L_y and L_z both reach minimum downstream of the junction and then start increasing. This is due to preservation of the volume of the droplet as L_x reaches its maximum downstream of the junction. L_z is lower than L_y which can be attributed to the additional squeezing of the droplets along the z -direction by the flows coming in through the vertical branch channels.

We plot the surface area of the deformed droplet S_d , against the droplet centroid x_c , in figure 2.6. The surface areas of the deformed droplets S_d are scaled with the undeformed surface area of the originally spherical droplet S_d^0 . It is observed that the scaled surface area of the droplets increase monotonically with increasing flow rate till it reaches a maximum downstream of the junction and then starts decreasing. With an increase in the flow rate, the hydrodynamic forces acting on the droplet increase, making the droplet becoming thinner and longer, which in turn increases the total surface area of the droplet.

The curvatures of the xz - and xy -profiles of the downstream tip of the droplets, C_{xz}^d and C_{xy}^d , are plotted in figure 2.7 (a) and (b). The curvatures C_{xz}^d , C_{xy}^d are scaled

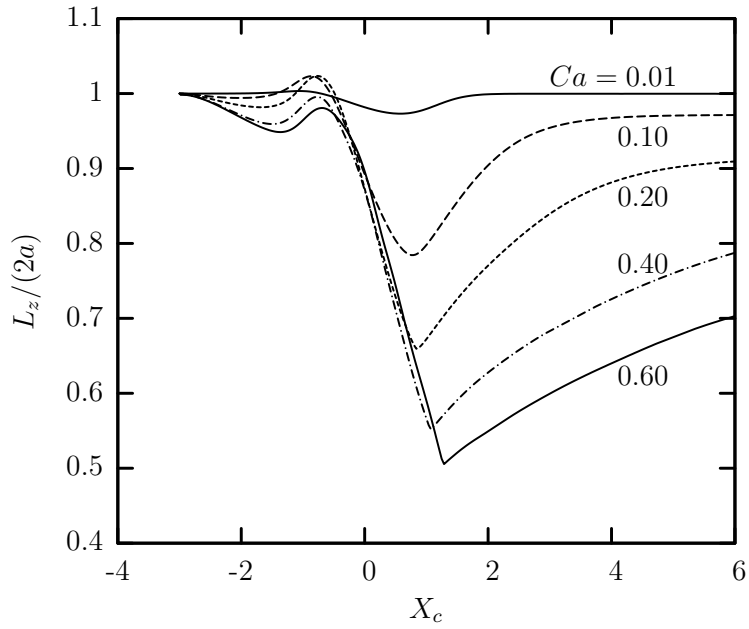
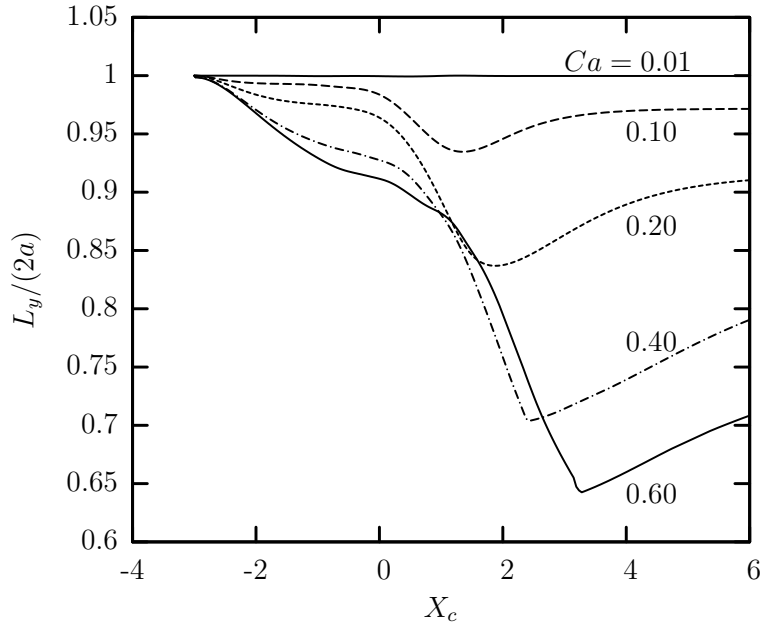


Figure 2.5: Droplet lengths along the y - and z -axes as a function of the droplet centroid x_c for $\lambda = 0.2$, $a = 0.7$, $q = 0.5$ and capillary number $Ca = 0.01, 0.1, 0.2, 0.4, 0.6$. (a) Droplet length along the y -axis $L_y/(2a)$. (b) Droplet length along the z -axis $L_z/(2a)$.

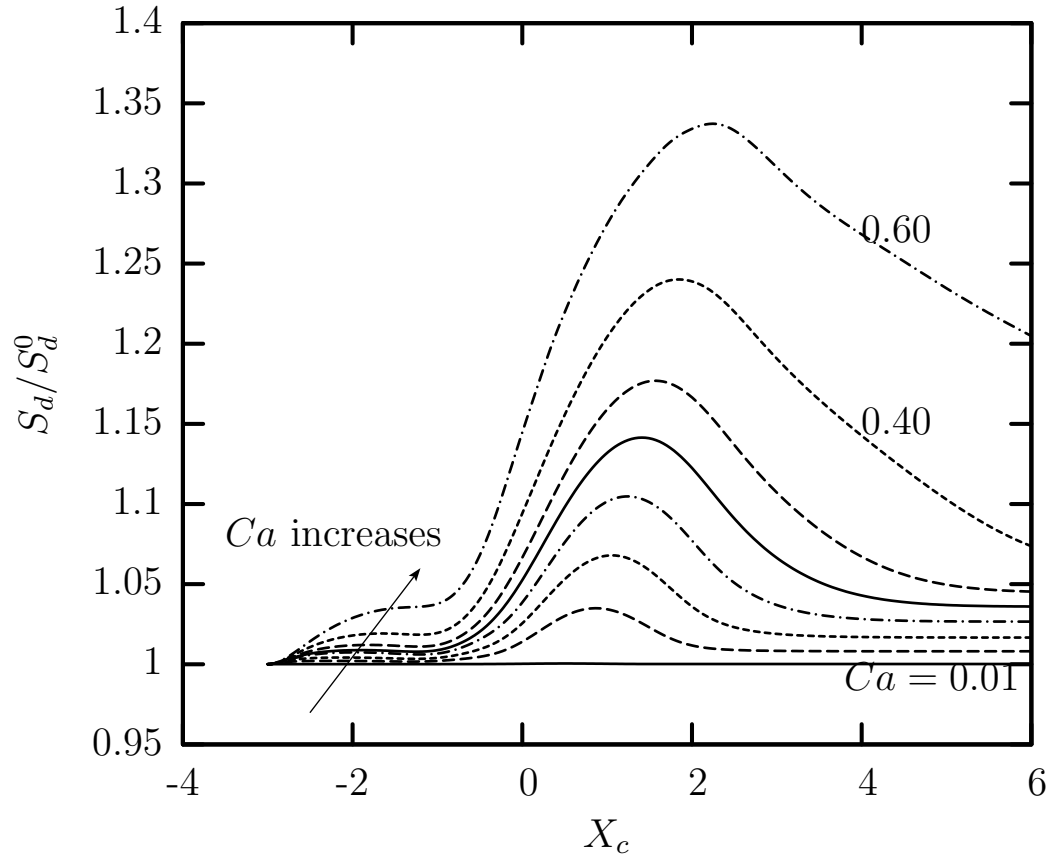


Figure 2.6: Surface area of the droplet (scaled with its undisturbed value) S_d/S_d^0 as a function of the droplet centroid x_c for $\lambda = 0.2$, $a = 0.7$, $q = 0.5$ and capillary number $Ca = 0.01, 0.1, 0.2, 0.4, 0.6$.

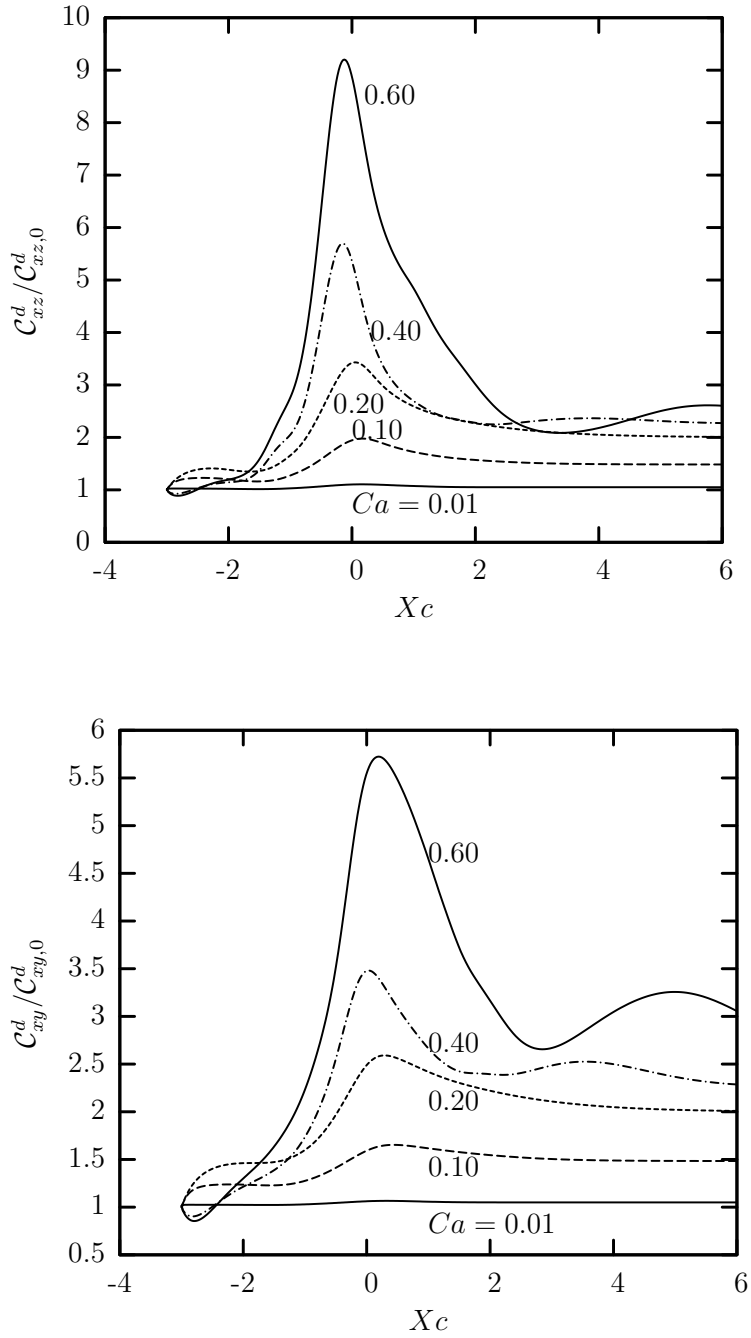


Figure 2.7: Curvatures of the downstream droplet tip as a function of the droplet centroid x_c for $\lambda = 0.2$, $a = 0.7$, $q = 0.5$ and capillary number $Ca = 0.01, 0.1, 0.2, 0.4, 0.6$. (a) Curvature of the droplet xz -profile C_{xz}^d . (b) Curvature of the droplet xy -profile C_{xy}^d . The curvatures are scaled with the curvature of the undisturbed spherical shape.

with the curvatures of the undeformed spherical droplet $\mathcal{C}_{xz,0}^d$, $\mathcal{C}_{xy,0}^d$ respectively. Both the curvatures increase with increasing flow rate owing to the formation of the pointed downstream tip of the droplet. It is observed that the xz -curvature is greater than the xy -curvature at all flow rates. This can be attributed to the additional squeezing of the front tip of the droplet due to flow coming in through the vertical branch channels. For both xz - and xy -profiles, the curvature reaches a maximum when the droplet centroid is very near to the junction center and then starts decreasing. This is because the front tip of the droplet becomes very thin when the droplet is in the zone of flow intersection near to the center of the junction. It is also observed that for high enough Ca , both xz - and xy -curvatures first decrease to a minimum after the droplet is released in the junction and then start increasing. For these cases with high Ca , the curvatures reach another minima after reaching the maxima and then increase again. The final values for both \mathcal{C}_{xz}^u and \mathcal{C}_{xy}^u increase with an increase in Ca .

Figure 2.8 shows the curvatures of the xz - and xy -profiles of the upstream rear of the droplet, \mathcal{C}_{xz}^u and \mathcal{C}_{xy}^u , against the droplet centroid x_c . The behavior of the curvatures \mathcal{C}_{xz}^u and \mathcal{C}_{xy}^u for the rear of the droplet are more complicated than the curvatures for the downstream tip of the droplet, \mathcal{C}_{xz}^d and \mathcal{C}_{xy}^d . As the droplet deforms, while moving from through the channel, the rear of the droplet undergoes a continual change in its shape. Unlike the \mathcal{C}_{xz}^d and \mathcal{C}_{xy}^d curvatures, for the downstream tip of the droplet, the curvatures for the rear of the droplet \mathcal{C}_{xz}^u and \mathcal{C}_{xy}^u show different behavior. Also the behavior of the curvature is heavily dependent on the Ca . For small Ca ($Ca = 0.01, 0.1$), \mathcal{C}_{xz}^u and \mathcal{C}_{xy}^u show a small increase in its curvature after the start of computations, while for Ca higher than that the curvatures decrease from its initial value. The initial increase in curvatures, for small Ca , arises as the droplet becomes elongated, with both the tip and the rear of the droplet becoming more pointed, and then gradually becomes flatter. For the higher capillary numbers considered in this study, the rear of the droplet tends to become flattened right after the computations. Both \mathcal{C}_{xz}^u and \mathcal{C}_{xy}^u remain less than 1 till the tip of the droplet enters the flow intersection near the center of the junction, after which their

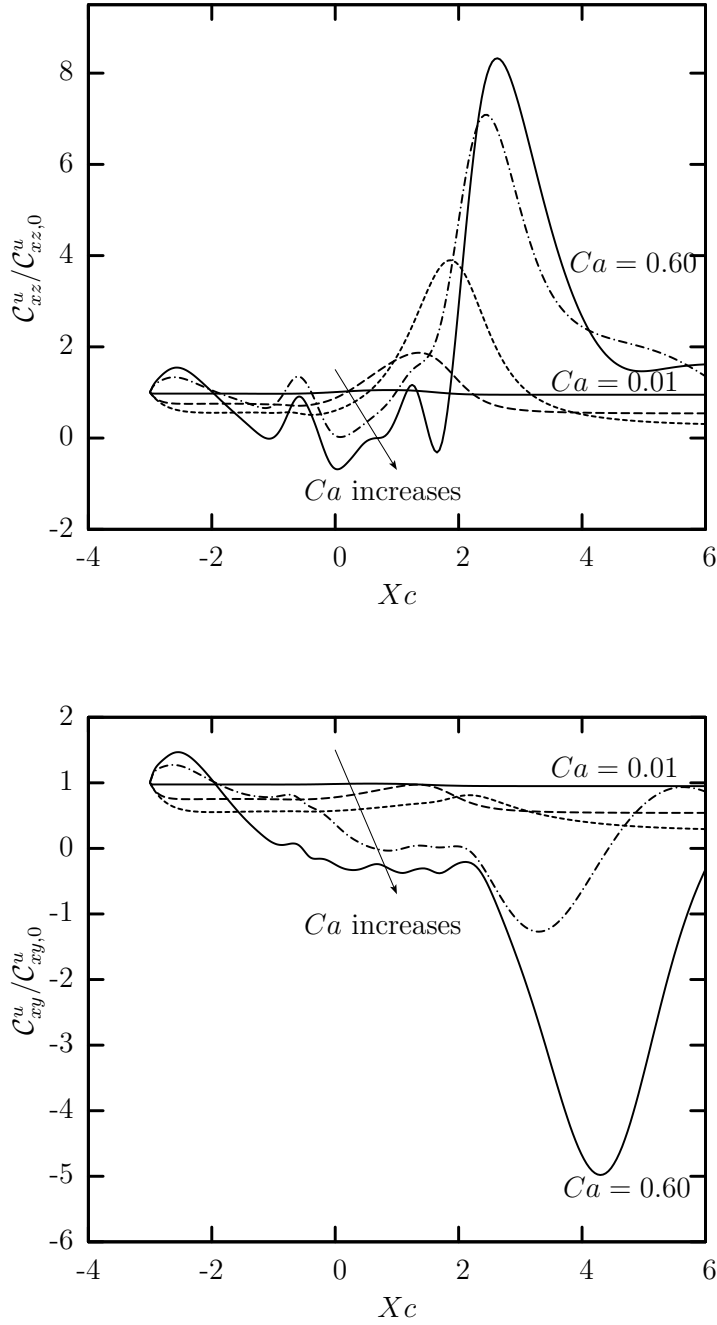


Figure 2.8: Curvatures of the upstream droplet tip as a function of the droplet centroid x_c for $\lambda = 0.2$, $a = 0.7$, $q = 0.5$ and capillary number, $Ca = 0.01, 0.1, 0.2, 0.4, 0.6$. (a) Curvature of the droplet xz -profile C_{xz}^u . (b) Curvature of the droplet xy -profile C_{xy}^u . The curvatures are scaled with the curvature of the undisturbed spherical shape.

behavior become completely different. C_{xz}^u starts increasing significantly as the rear of the droplet gets squeezed due to the flow coming in through the vertical branch channels, which increases with an increase in the flow rate. C_{xy}^u starts decreasing with an increased flow rate, as the hydrodynamic forces acting on the droplet increase and to balance this force with the surface tension forces, the rear of the droplet starts taking a concave shape, as explained before. With an increase in flow rate, the rear of the droplet becomes more concave and C_{xy}^u becomes even more negative. As the droplet leaves the flow intersection and gradually regains its bullet shape, C_{xz}^u starts decreasing and C_{xz}^u starts to increase.

We plot the droplet velocity U_x and the additional pressure difference due to the presence of the droplet ΔP^+ , against the droplet centroid x_c , in figure 2.9(a) and (b) respectively. We observe from figure. 2.9(b) that the final velocity attained by the droplet at the end of the channel increases with Ca . This is due to stronger hydrodynamic forces acting on the droplet with increased Ca . Similar behavior has been observed by Wang and Dimitrakopoulos in their study of microfluidic droplets in a straight rectangular channel [48]. As the droplet becomes thinner with an increased flow rate, there is more space for the surrounding fluid to flow through and hence the additional pressure difference decreases.

Figure 2.10 shows the plots of the minimum distance of the droplet from the $z = -l_z$ wall of the junction h , plotted against the droplet centroid x_c as the droplet moves through the channel. At the start of our computations, after releasing the droplet in the junction a slight increase of the gap thickness is observed which is due to slight lengthening of the droplet from its original spherical shape. It is followed by a slight decrease, just before the droplet centroid enters the junction, as the droplet's rear takes the shape of a disc as the front tip becomes thinner. The minimum distance h then starts increasing to a maximum as the droplet becomes progressively thinner under increased shear force due to additional flow through the branch channels and then starts decreasing as the droplet gradually regains its bullet shape.

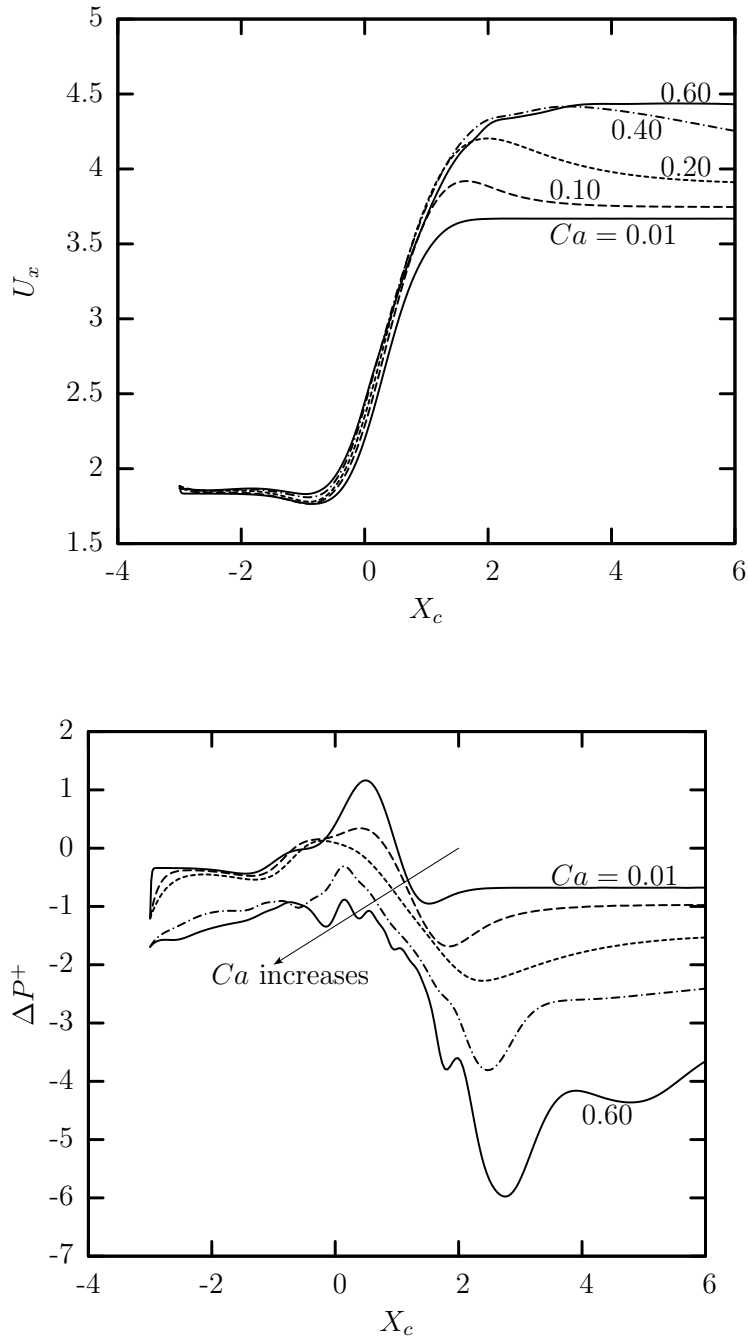


Figure 2.9: Droplet velocity and additional pressure difference as a function of the droplet centroid x_c for $\lambda = 0.2$, $a = 0.7$, $q = 0.5$ and capillary number $Ca = 0.01, 0.1, 0.2, 0.4, 0.6$. (a) Droplet velocity U_x . (b) Additional pressure difference ΔP^+ .

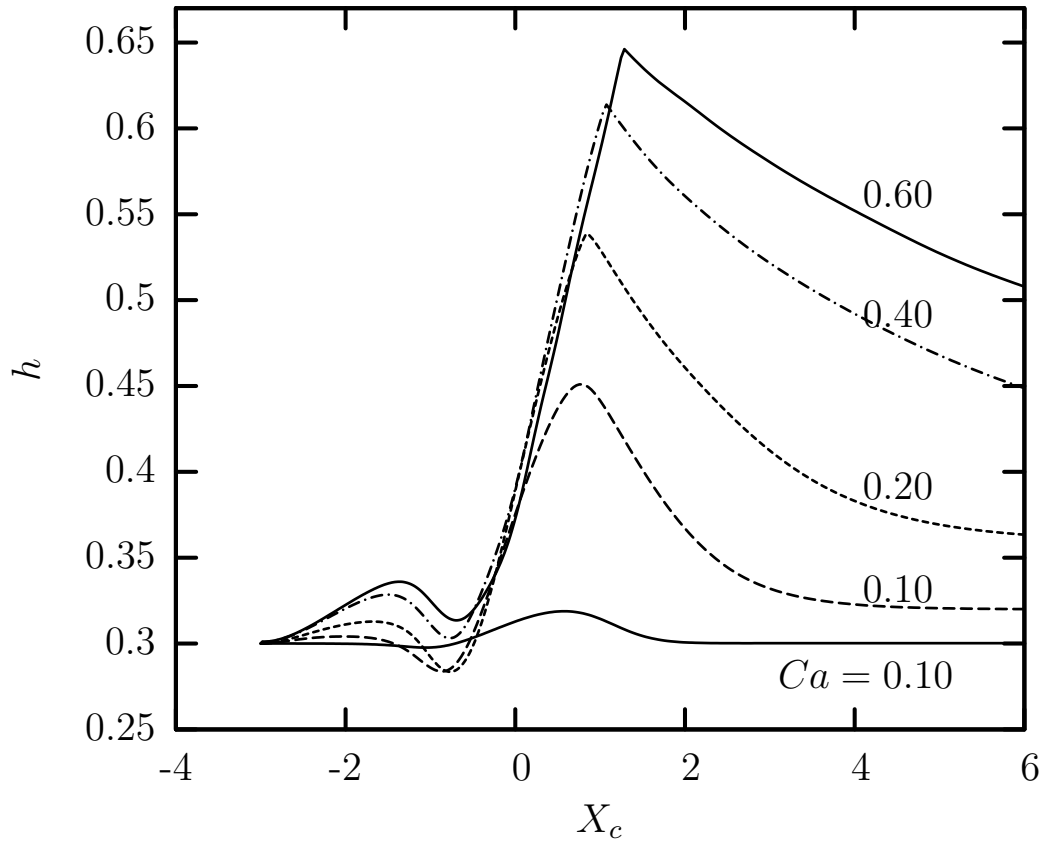


Figure 2.10: Minimum distance h of the droplet interface from the $z = -l_z$ wall of the junction as a function of the droplet centroid x_c for $\lambda = 0.2$, $a = 0.7$, $q = 0.5$ and capillary number $Ca = 0.01, 0.1, 0.2, 0.4, 0.6$.

2.4.2 Effect of droplet size

In this section, we collect the results of our computations studying the effects of droplet size on its dynamics in the microfluidic cross-junction. The spherical droplets with viscosity ratio $\lambda = 0.2$ and capillary number $Ca = 0.1$ are placed upstream of the junction at $x_c = -3.0$, with the flow rates in the vertical branch channels maintained constant at $q = 0.5$. The range of droplet sizes studied in this chapter varies from moderately sized droplets with $a = 0.5$ to large droplets with $a = 0.95$. From our computations we found that the droplet dynamics depends strongly as a function of droplet size a .

Figure 2.11(a) shows the droplet lengths L_x along the flow direction, which is the x -axis, plotted against the droplet centroid x_c . We scale the the droplet length L_x with its undisturbed value as it allows us to compare the deformation of droplets of various sizes. As soon as we release a droplet, at its initial position with $x_c = -3.0$, the droplet moves along the centerline of the junction and its shape deforms, with an increase in its length and decrease in width. The droplet takes the bullet shape on deformation with a pointed downstream tip and a flatter rear. We observe from the plots that the deformation of a droplet, till it enters the flow intersection, depends on its size. For the moderately sized droplets ($a = 0.5, 0.6, 0.7$) the initial deformation after being released is very small, while for the larger sized droplets ($a = 0.8, 0.9, 0.95$) there is an instantaneous increase in their deformation. This is because of the smaller surface area of the moderately sized droplets, which makes the hydrodynamic forces acting on them small, as compared to the droplets larger in size. We observe from the plots that for a moderately sized droplet ($a = 0.5, 0.6, 0.7$) there is a very small decrease in its length when it is just about to enter the flow intersection, which is due to the downstream tip of the droplet becoming a little flatter due to the flow coming in through the vertical branch channels. In case of the larger droplets the increase in their lengths is monotonic, as due to their large size the hydrodynamic forces acting on them is big. The deformation of the droplets increase considerably after they enter the flow intersection, as due to the

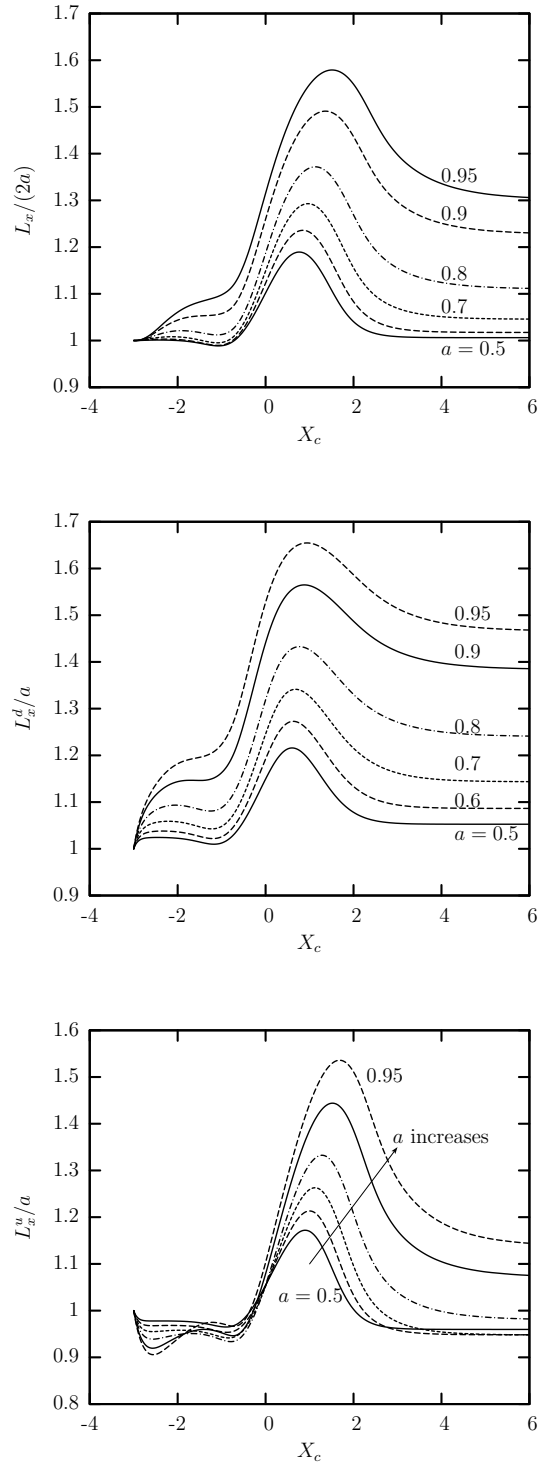


Figure 2.11: Droplet lengths along the flow direction as a function of the droplet centroid for $\lambda = 0.2$, $Ca = 0.1$, $q = 0.5$ and droplet size $a = 0.5, 0.6, 0.7, 0.8, 0.9, 0.95$. (a) Droplet length $L_x/(2a)$. (b) Downstream droplet length L_x^d/a and (c) Upstream droplet length L_x^u/a .

flows coming in through the vertical branch channels the hydrodynamic forces acting on the droplets increase. L_x reaches a maximum slightly downstream of the junction and then starts decreasing. For all droplet sizes studied, the lengths of the droplet L_x at the end of the junction is more than its undisturbed value at the start of computations. It is to be noted that the droplet deformation, and thus its length L_x , increases significantly with an increase in the droplet size. This is due to the fact that due to the large size of the droplet, the effective capillary number acting on the droplet becomes,

$$Ca^{\text{eff}} \sim \frac{\mu U}{\gamma} \left(\frac{L_z}{h}\right)^n \quad (2.15)$$

due to the stronger hydrodynamic forces in the small gap h , where L_z is the length of the droplet along the z -axis. For the moderately sized droplets, the factor $(\frac{L_z}{h})^n$ is not significantly greater than 1, while for the larger sized droplets the factor is large as h , the distance of the droplet interface from the $z = -l_z$ wall of the junction decreases with an increase in droplet size, as can be seen in figure 2.12. This is because of the higher deformation of the larger sized droplets by becoming thinner and longer to preserve its volume, while allowing the surrounding fluid to flow through the channel.

We divide the total droplet length L_x into the droplet's upstream length L_x^u and the downstream length L_x^d (calculated from the droplet centroid to the rear and front tips of the droplet) to explain the deformation of the front and rear parts of the droplet. We show the downstream and upstream lengths of the droplets in figure 2.11(b) and figure 2.11(c) respectively. The behavior of the downstream droplet length L_x^d is very similar to that of L_x , while L_x^u first go to a minimum before it starts increasing. This is due to the evolution of a pointed downstream tip and a flatter rear during deformation of the droplet, which causes the droplet centroid to move towards the rear of the droplet. With an increase in the droplet size, the downstream length of the droplet L_x^d increases monotonically due to the lengthening of the downstream portion of the droplet. After the slow initial increase, L_x^d increases rapidly after it enters the flow intersection, due to the flow coming in through the vertical branch channels, and reaches a maximum slightly downstream

of the flow intersection. L_x^d decreases rapidly after reaching the maximum. For the moderately sized droplets, L_x^d reach a steady state, which is only slightly higher than its undisturbed value a , while for the larger droplets, the final values of L_x^d is significantly higher.

From figure 2.11(c) we observe that before the droplet enters the flow intersection zone, L_x^u decreases to a minimum, which is due to the flattening of the rear of the droplet. However, after the droplet enters the flow intersection, L_x^u increases rapidly as the rear of the droplet gets elongated and reaches a maximum slightly downstream of the flow intersection, similar to L_x^d . As the droplet gradually regains its bullet shape L_x^u starts decreasing rapidly. Eventually L_x^u reaches a steady state for the moderate droplet sizes which is lower than its undisturbed value. For the very large droplet sizes ($a = 0.9, 0.95$), L_x^d remains higher than 1 as the deformation and elongation in those cases is very high. It is also observed from figure 2.11(b) and (c) that L_x^d is larger than L_x^u for all droplet sizes and at all points inside the junction. This arises from the fact that the rear of the droplet is always flatter, and hence shorter, than the front tip of the droplet.

In figure 2.12 (a) and (b) we plot L_y and L_z against the droplet centroid x_c . The final values of both L_y and L_z at $x_c = 6.0$ decrease with an increase in droplet size. However, the initial behavior of L_y and L_z , before the droplet enters the flow intersection, are different. For all droplet sizes studied, after the droplet is released in the horizontal main channel of the junction, L_y decreases continually till it reaches a minimum slightly downstream of the junction and then starts increasing. On the other hand L_z shows different behavior for different droplet sizes studied. For the very large droplet sizes studied ($a = 0.9, 0.95$), there is a rapid decrease in L_z and then a rapid increase before the droplet enters the flow intersection, while for the smaller droplets, there is no significant decrease in L_z before it starts increasing before reaching the flow intersection. This behavior again can be explained by considering the high Ca^{eff} in the case of the larger droplets, which makes the droplets thinner and longer, as soon they are released in the junction, to enable the surrounding fluid to flow through the channel. The front tip of the droplet, before it enters the

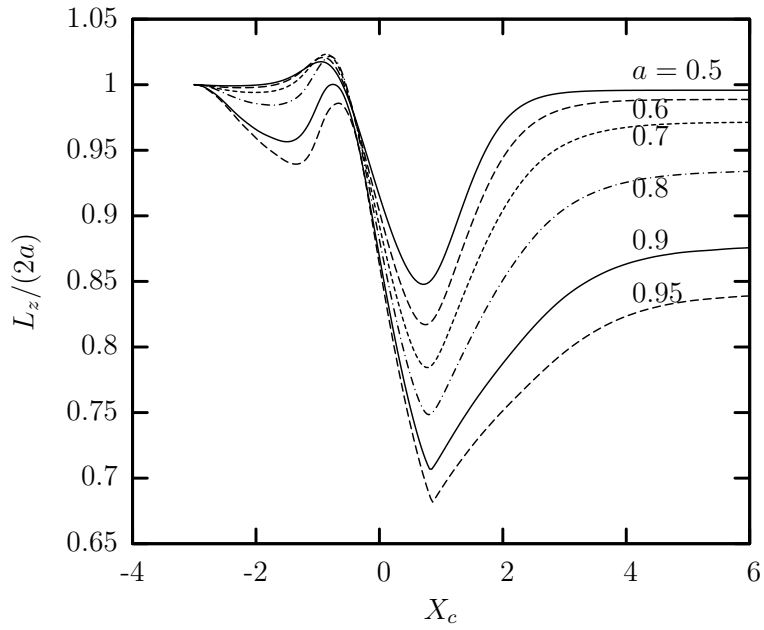
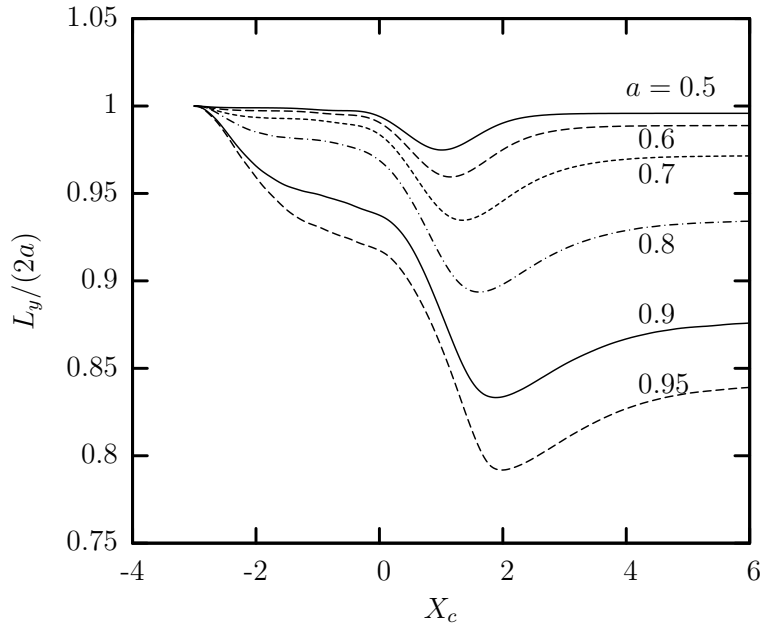


Figure 2.12: Droplet lengths along the y - and z -axes as a function of the droplet centroid x_c for $\lambda = 0.2$, $Ca = 0.1$, $q = 0.5$ and droplet size $a = 0.5, 0.6, 0.7, 0.8, 0.9, 0.95$. (a) Droplet length along the y -axis $L_y/2a$. (b) Droplet length along the z -axis $L_z/2a$.

flow intersection, gets flattened due to the flow coming through the vertical branch channels and hence L_z shows a sharp increase. For all droplet sizes studied, L_z is always lower than the L_y , which can be attributed to the additional squeezing of the droplets along the z -axis by the flows coming in through the vertical branch channels.

In figure 2.13 we show the plots of droplet surface area against the droplet centroid x_c . The surface area S_d is scaled with the surface area of the undisturbed spherical droplet S_d^0 . The droplet surface area is an important parameter as it gives us a general indication about the deformation of the droplet inside the junction. It is observed that S_d starts increasing after the droplet is released in the junction, until it reaches a maximum downstream of the flow intersection and then starts decreasing. The rapid increase in S_d/S_d^0 is due to the increased flow coming in through the vertical branch channels. For the large droplets ($a = 0.9, 0.95$), there is a small decrease in the droplet surface area before the front tip of the droplet enters the flow intersection which corresponds to the flattening of the front tip and a decrease in the droplet deformation. For all droplet sizes, the droplet deformation, hence S_d/S_d^0 , increases with an increase in the droplet size a at all x_c . We also observe that for the moderately sized droplets ($a = 0.5, 0.6, 0.7, 0.8$) the increase in S_d/S_d^0 at $x_c = 6.0$ is not significant as compared to the droplets with $a = 0.8, 0.9, 0.95$.

The curvatures of the xz - and xy -profiles of the downstream tip of the droplets, \mathcal{C}_{xz}^d and \mathcal{C}_{xy}^d , are plotted in figure 2.14 (a) and (b) respectively. The curvatures \mathcal{C}_{xz}^d , \mathcal{C}_{xy}^d are scaled with the curvatures of the undeformed spherical droplet $\mathcal{C}_{xz,0}^d$, $\mathcal{C}_{xy,0}^d$ respectively. The final values attained by both \mathcal{C}_{xz}^d and \mathcal{C}_{xy}^d at $x_c = 6.0$ increases with an increase in the droplet size a . This is due to the formation of a pointed downstream droplet tip on deformation. Both \mathcal{C}_{xz}^d and \mathcal{C}_{xy}^d start increasing after the droplet is released in the junction upstream of the flow intersection. We observe that for all droplet sizes a , \mathcal{C}_{xy}^d keeps on increasing till it reaches maximum slightly downstream of the junction and then decreases to a steady state. For the droplets with $a = 0.5, 0.6, 0.7, 0.8$, the curvatures show a slight decrease, after the initial increase, before the droplet enters the flow intersection. This is due to the

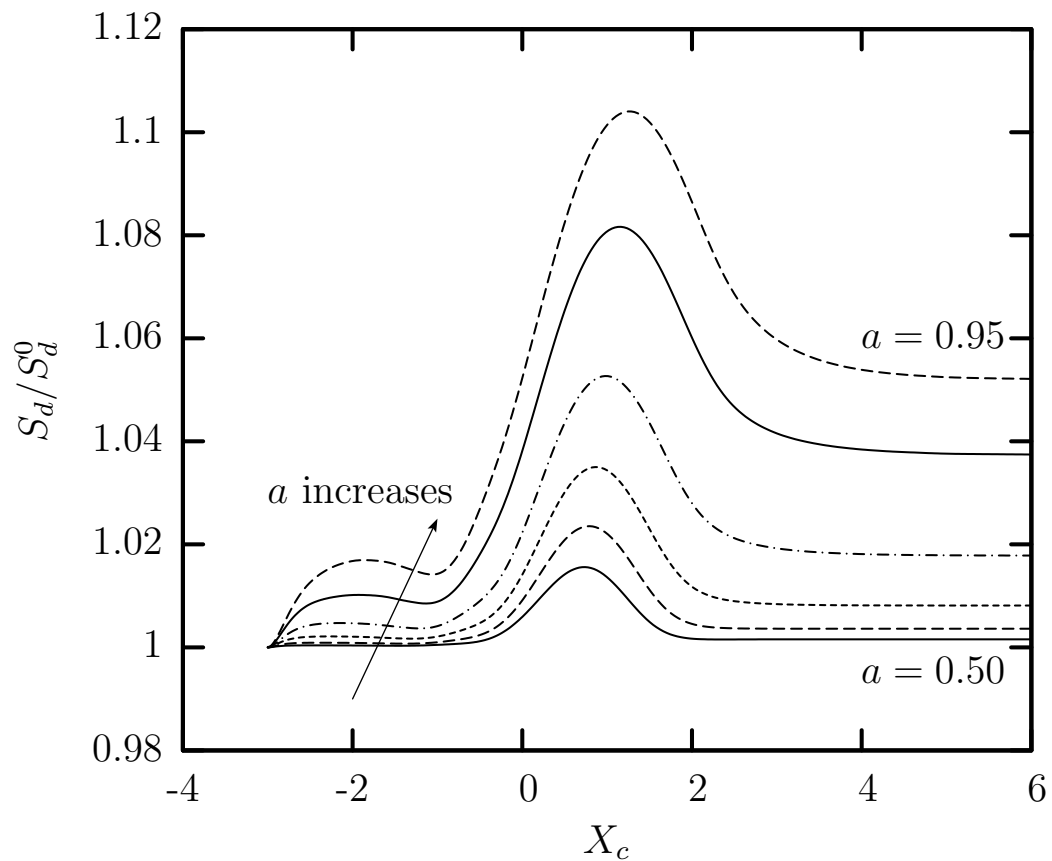


Figure 2.13: Surface area of the droplet (scaled with its undisturbed value) S_d/S_d^0 as a function of the droplet centroid x_c for $\lambda = 0.2$, $Ca = 0.1$, $q = 0.5$ and droplet size, $a = 0.5, 0.6, 0.7, 0.8, 0.9, 0.95$.

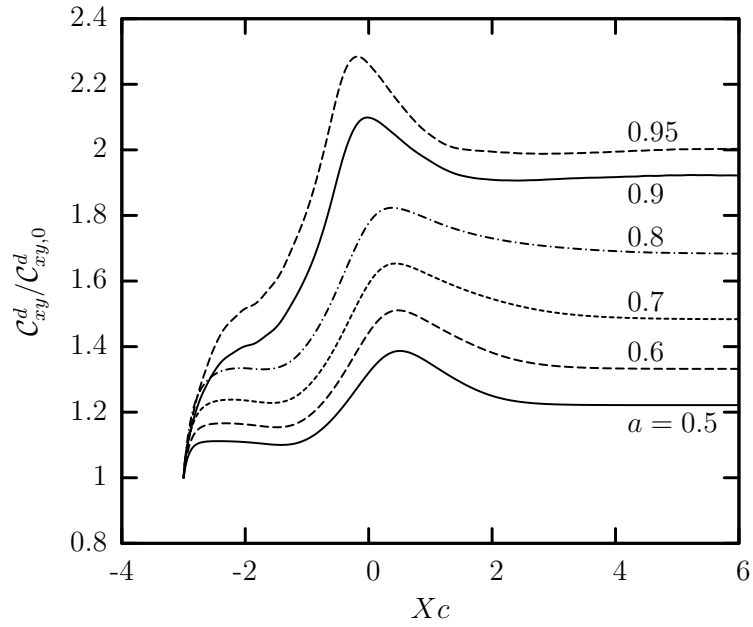
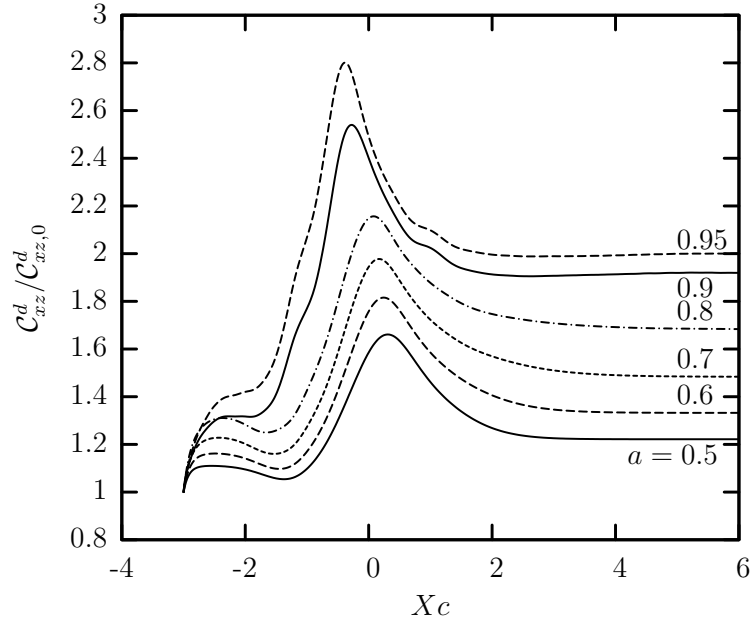


Figure 2.14: Curvatures of downstream droplet tip as a function of the droplet centroid x_c for $\lambda = 0.2$, $Ca = 0.1$, $q = 0.5$ and droplet size $a = 0.5, 0.6, 0.7, 0.8, 0.9, 0.95$. (a) Curvature of the droplet xz -profile C_{xz}^d . (b) Curvature of the droplet xy -profile C_{xy}^d .

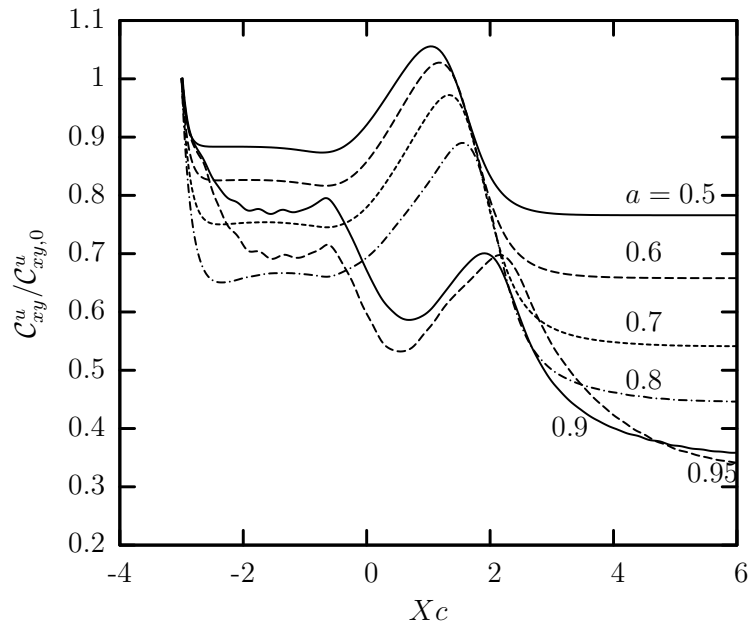
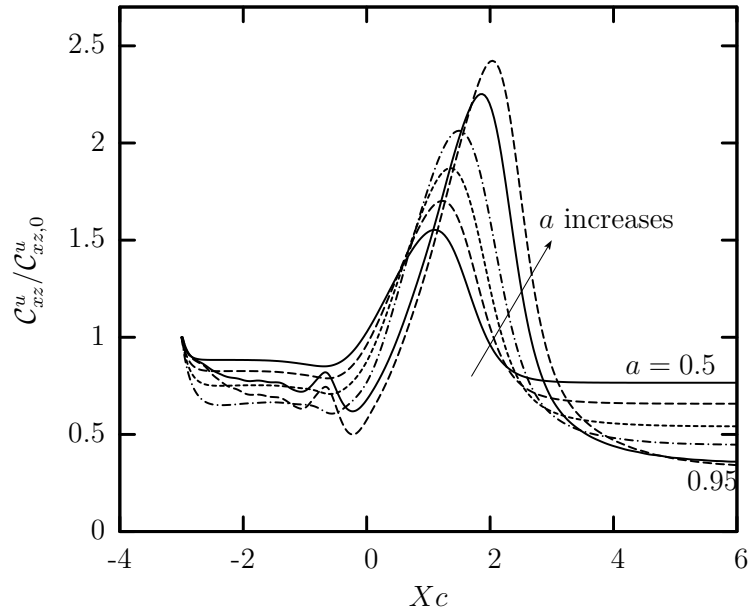


Figure 2.15: Curvatures of the upstream droplet tip as a function of droplet centroid x_c for $\lambda = 0.2$, $Ca = 0.1$, $q = 0.5$ and droplet size $a = 0.5, 0.6, 0.7, 0.8, 0.9, 0.95$. (a) Curvature of the droplet xz -profile C_{xz}^u . (b) Curvature of the droplet xy -profile C_{xy}^u .

squeezing of the downstream tip of the droplet by the flow coming in through the vertical branch channels. As there \mathcal{C}_{xy}^d does not decrease before the droplet enters the flow intersection zone, we note that the flow coming in through the vertical branch channels do not effect the curvature of the xy -profile of the front tip of the droplet, for all droplet sizes considered.

The upstream tip curvatures \mathcal{C}_{xz}^u and \mathcal{C}_{xy}^u show behavior different from the downstream tip curvatures \mathcal{C}_{xz}^d and \mathcal{C}_{xy}^d . We observe, from the plots of figure 2.15(a) and (b), that the final values of the upstream tip curvatures \mathcal{C}_{xz}^u and \mathcal{C}_{xy}^u , at $x_c = 6.0$ decrease with an increase in droplet size. This is due to the larger deformation of the larger droplets, which again is due to higher Ca^{eff} . Both \mathcal{C}_{xz}^u and \mathcal{C}_{xy}^u initially show a decrease after the droplet is released in the junction, followed by an increase to a maximum and then a subsequent decrease. We also observe that the maximum value attained by \mathcal{C}_{xz}^u during deformation increases with an increase in droplet size while the maximum value of \mathcal{C}_{xy}^d during deformation decreases with an increase in droplet size. This increase in the maximum value of \mathcal{C}_{xz}^u , with an increase in a , is due to the squeezing of rear of the droplet by the flow coming in through the vertical branch channels when it is in the flow intersection, which results a higher deformation of the xz -profile of the droplet. The maximum value of \mathcal{C}_{xy}^d decreases with an increase in the droplet size as the rear of the droplet becomes flatter with an increase in the droplet size a . The final values of the curvatures \mathcal{C}_{xz}^u and \mathcal{C}_{xy}^u are less than 1 which is due to the flattening of the rear of the droplet as compared to the undeformed spherical shape.

In figure 2.16(a) we plot the droplet velocity as a function of the droplet centroid x_c . Upon release, the droplet velocity decreases to a minimum before the droplet enters the flow intersection zone and the increases sharply to a maximum downstream of the flow intersection. This is followed by another small decrease to a value which is higher than the initial velocity of the droplet, due to the additional flow through the vertical channels. U_x reaches a steady state at $x_c = 6.0$ the moderately sized droplets with $a = 0.5, 0.6, 0.7$. We also observe that the droplets with smaller size move faster inside the junction at all x_c . Similar behavior has been

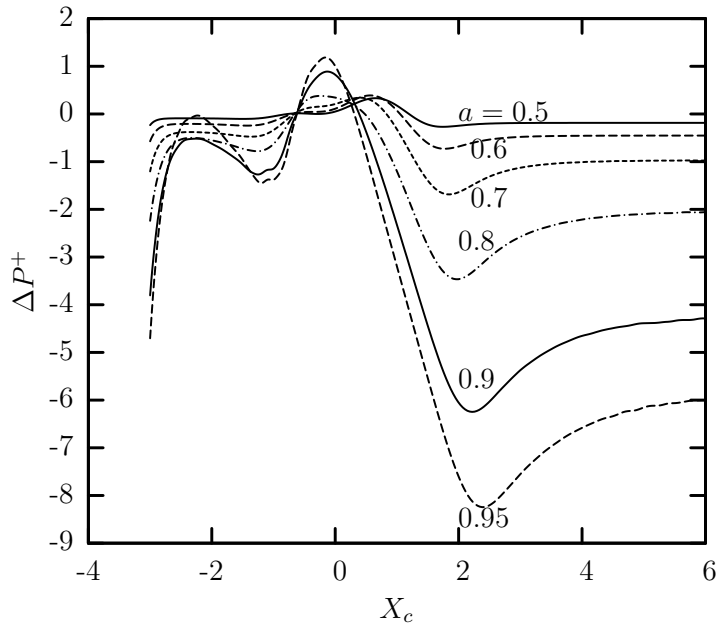
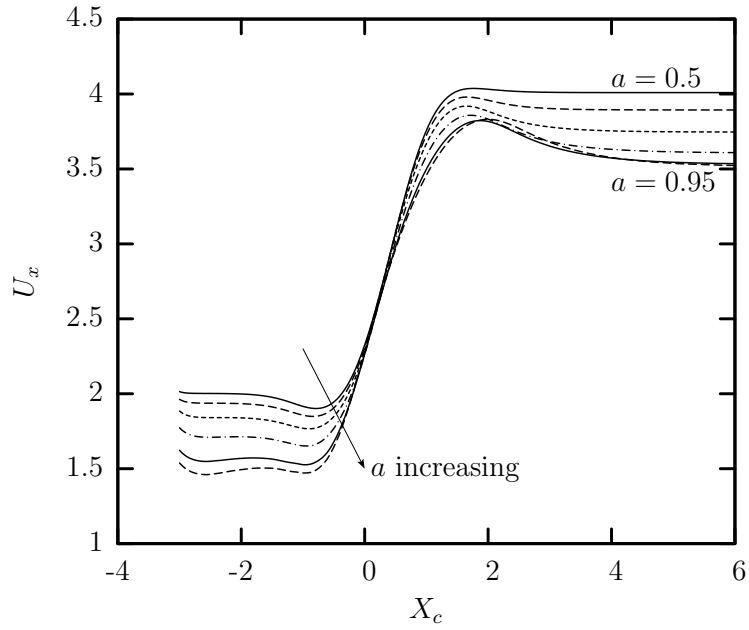


Figure 2.16: Droplet velocity and additional pressure difference as a function of droplet centroid x_c for $\lambda = 0.2$, $Ca = 0.1$, $q = 0.5$ and droplet size $a = 0.5, 0.6, 0.7, 0.8, 0.9, 0.95$. (a) Droplet velocity U_x . (b) Additional pressure difference ΔP^+ .

observed in the case of a single droplet moving in a straight rectangular microfluidic channel [48].

Figure 2.16(b) shows plots of additional pressure difference due to the presence of the droplet as a function of the droplet centroid x_c . From the plots we observe that the initial and the final values of additional pressure difference are negative for all droplet sizes. We also observe that the final value of ΔP^+ becomes more negative with an increase in the droplet size a . This is a result of the higher deformation of the droplet, and hence its lengthening, due to its small viscosity ratio, which in turn blocks the flow less effectively causing ΔP^+ to decrease. For all droplet sizes studied in this chapter, ΔP^+ is positive for a small range of x_c . This positive ΔP^+ occurs when the deformed droplet, a flat rear and a pointed front tip, is completely within the flow intersection zone and thus blocks the flow of the surrounding fluid much more efficiently causing ΔP^+ to become positive.

Figure 2.17 shows the minimum distance of the droplet from the $z=-l_z$ wall of the junction h , plotted against the droplet centroid x_c as the droplet moves through the channel. The minimum distance h reaches a maximum slightly downstream of the junction and then starts decreasing. This is due to the droplet becoming longer and thinner due to the incoming flows to the junction through the vertical branch channels. The final values of the h decreases with an increase in the droplet size a .

2.4.3 Effect of viscosity ratio

In this section, we collect the results and study the effects of viscosity ratio on the dynamics of a droplet with capillary number $\text{Ca} = 0.1$, droplet size $a = 0.7$ and flow rate in branch channel $q = 0.5$. The range of viscosity ratio studied here range from very low ($\lambda = 0.01$) to very high ($\lambda = 20.0$). It was observed from our computations that the droplet dynamics varies strongly as a function of the viscosity ratio of the fluids.

Figure 2.18(a) shows the droplet lengths L_x along the flow direction as a function of the droplet centroid x_c for different viscosity ratios. We also divide the total droplet length L_x into the droplet's upstream and downstream length, L_x^u and

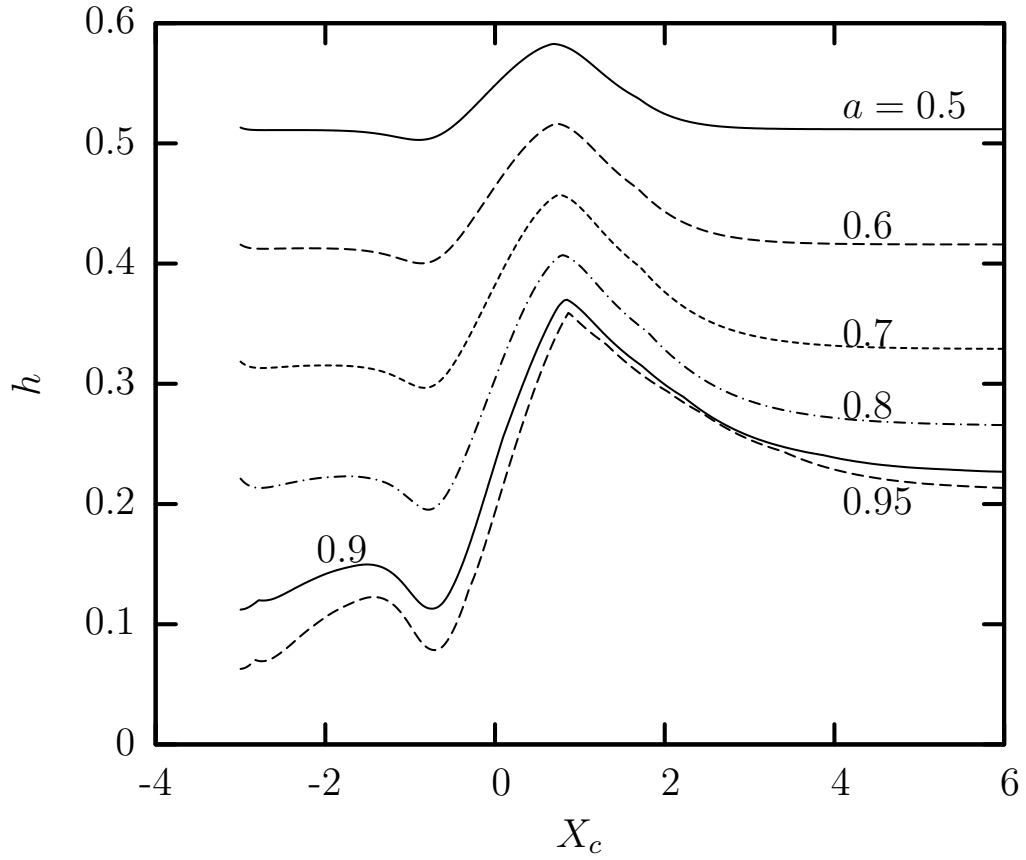


Figure 2.17: Minimum distance h of the droplet interface from the $z = -l_z$ wall of the junction as a function of of the droplet centroid for $\lambda = 0.2$, $Ca = 0.1$, $q = 0.5$ and droplet size $a = 0.5, 0.6, 0.7, 0.8, 0.9, 0.95$.

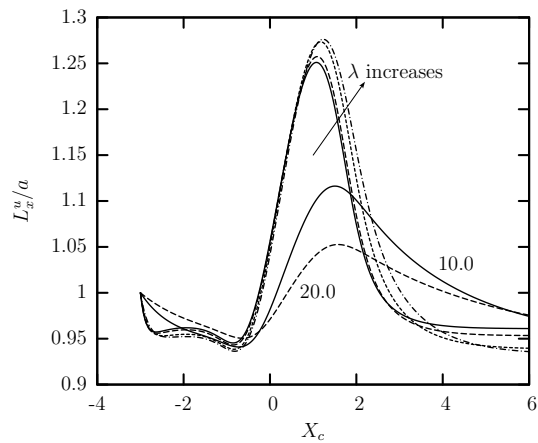
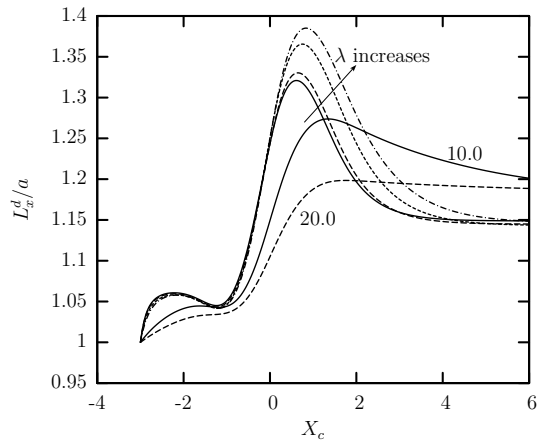
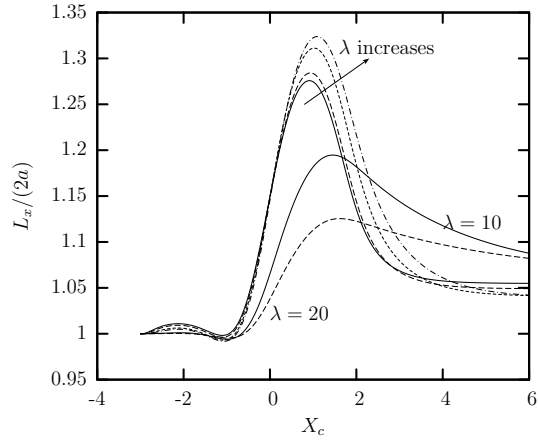


Figure 2.18: Droplet lengths along the flow direction as a function of the droplet centroid x_c for $Ca = 0.1$, $a = 0.7$, $q = 0.5$ and viscosity ratio $\lambda = 0.01, 0.1, 0.5, 1.0, 10.0, 20.0$. (a) Droplet length $L_x/(2a)$. (b) Downstream droplet length L_x^d/a . (c) Upstream droplet length L_x^u/a .

L_x^d , (calculated from the droplet centroid x_c to the rear and the front tips of the droplet respectively) and plot them separately in figure 2.18(b, c) as a function of the droplet centroid x_c . We observe from the plots of figure 2.18(a) that the droplet length L_x depends upon the viscosity ratio λ . For all viscosity ratios λ studied, the droplet length shows a small increase, followed by a small decrease to a minimum before the droplet enters the flow intersection. After the minimum is reached, there is a rapid increase in L_x to a maximum, as the droplet enters the flow intersection, and then a sharp decrease as the droplet leaves the flow intersection. The initial increase in droplet length, upstream of the flow intersection, is because of the initial deformation of the droplet after being released in the horizontal main channel of the junction while the decrease to minimum is due to shortening of the droplet with the front tip being flatter. The increase to the maximum, downstream of the flow intersection, is because of the additional flow coming in through the vertical branch channels. We observe that for $\lambda = [0.01, 1]$, the maximum value of L_x at the downstream of the junction increases with an increase in λ , while for $\lambda = 10, 20$ the opposite happens. In the case of a single droplet in a rectangular straight channel, it has been observed that the steady state deformation of the droplet, and hence L_x , increases with an increase in λ due to an increase in higher inner hydrodynamic forces [48]. However, deformation takes place slower for a droplet with a higher λ , *i.e.*, a more viscous droplet needs more time deforming from its initial shape. The time needed for a droplet to deform can be expressed as,

$$\tau \sim (1 + \lambda)Ca \tau_f \quad (2.16)$$

In a cross-junction, when λ is small there is enough time for the droplet to deform and hence the maximum L_x increases with an increase in λ . When $\lambda = 10, 20$, the time needed by the droplet to deform to its maximum, in a cross-junction, is significantly raised as the factor $(1+\lambda)$ becomes dominant and hence we observe the decrease in the maximum L_x with an increase in λ . In our study, the droplets do not reach steady state at the end of the device, but if given enough time, the final value of L_x will increase with an increase in λ .

The downstream and upstream lengths of the droplet, L_x^d and L_x^u , show behavior similar to L_x as can be seen from figure 2.18(b) and (c). We observe that, after the droplet is released in the horizontal main channel of the junction, L_x^d shows a sharp increase followed by a small decrease, while L_x^u shows a decrease to a minimum before the droplet enters the flow intersection. This behavior of L_x^d and L_x^u is due to the initial lengthening of the droplet with a pointed tip and a flat rear, followed by flattening of the pointed front tip when the front tip is about to enter the flow intersection zone. The maximum values attained by L_x^d and L_x^u are similar to the maximum value attained by L_x and depends upon the viscosity ratio λ , hence the time needed for deformation. We also observe that the downstream droplet length L_x^d is greater than the upstream droplet length L_x^u for all viscosity ratios. The final value of L_x^d at $x_c = 6$ is greater than 1, while for L_x^u at $x_c = 6$ it is smaller than 1, which is due to the movement of the droplet centroid towards the rear of the droplet owing to the pointed tip and the relatively flat rear of the droplet.

The plots for the droplet lengths along the y - and z -axes, L_y and L_z , are shown in figure 2.19(a) and (b) respectively as a function of the droplet centroid x_c . We observe that L_y decreases monotonically for $\lambda = [0.01, 1.0]$ till it reaches a minimum downstream of the flow intersection and then starts increasing. For $\lambda = [10, 20]$, L_y decreases monotonically after the droplet is released in the horizontal main channel. The minimum value of L_y decreases with an increase in λ for $\lambda = [0.01, 1.0]$. The value of L_y for $\lambda = 10$ is lower than that for $\lambda = 20$. This again can be explained by considering the time τ needed by the droplet to deform, as explained while discussing the the plots of figure 2.18. The behavior of L_z is very similar to that of L_y for $\lambda = [0.01, 1.0]$. For $\lambda = [10, 20]$ L_z does have a minimum downstream of the flow intersection which is due to the flow coming in through the vertical branch channels, while L_y did not have any such minimum.

Figure 2.20 shows the plots of the surface area of the deformed droplet S_d plotted against the droplet centroid x_c for different viscosity ratios. The surface area of the deformed droplet S_d is scaled with its undisturbed value S_d^0 . From the plots we observe that S_d reaches a maximum downstream of the flow intersection

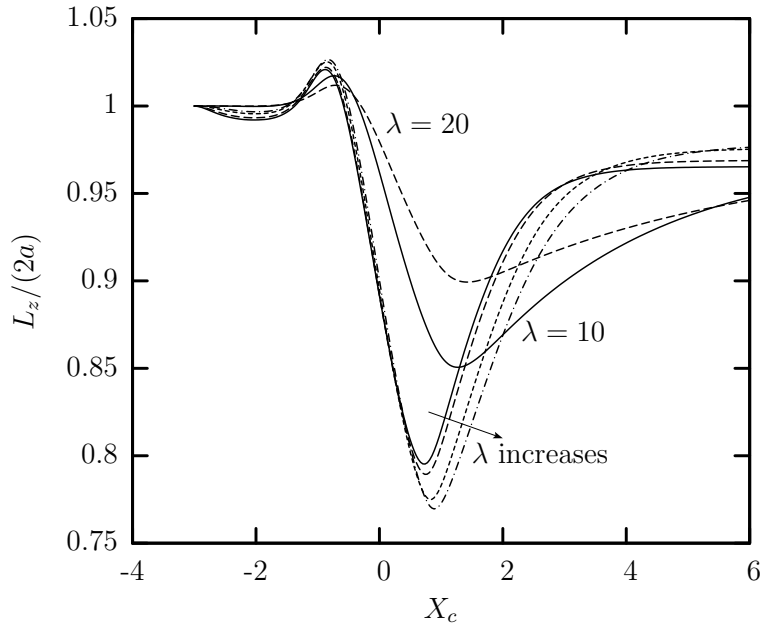
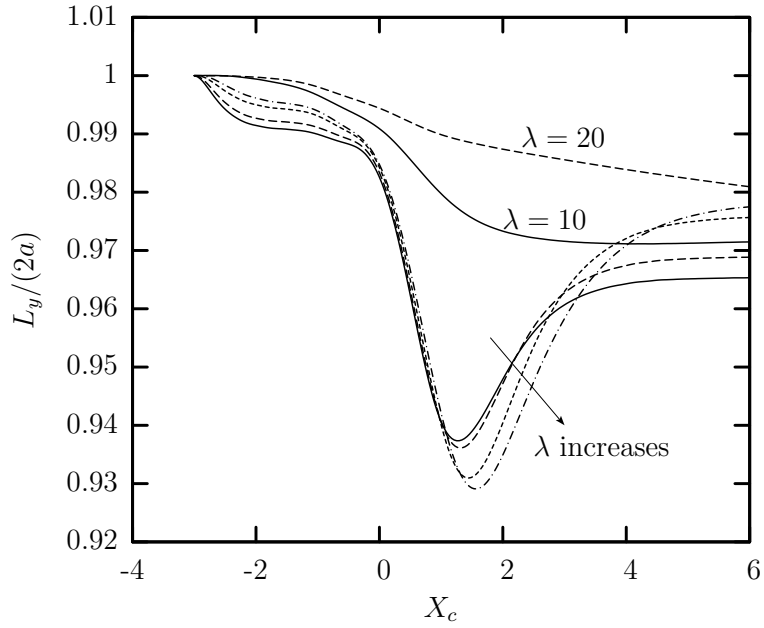


Figure 2.19: Droplet lengths along the y - and z -axes as a function of the droplet centroid x_c for $Ca = 0.1$, $a = 0.7$, $q = 0.5$ and viscosity ratio $\lambda = 0.01, 0.1, 0.5, 1.0, 10.0, 20.0$. (a) Droplet length along the y -axis $L_y/(2a)$. (b) Droplet length along the z -axis $L_z/(2a)$.

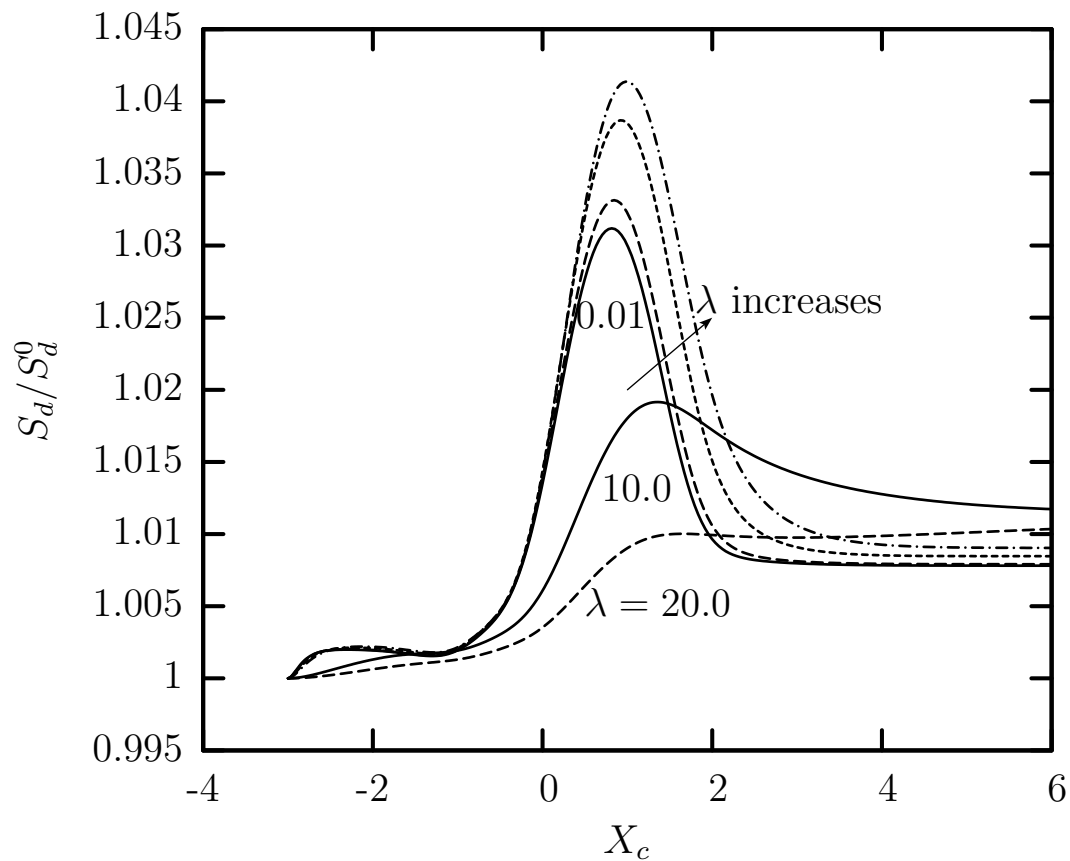


Figure 2.20: Surface area of the droplet (scaled with its undisturbed value) S_d/S_d^0 a function of the droplet centroid x_c for $Ca = 0.1$, $a = 0.7$, $q = 0.5$ and viscosity ratio $\lambda = 0.01, 0.1, 0.5, 1.0, 10.0, 20.0$.

and then starts decreasing. The maximum S_d reached by the droplet increases with an increase in the viscosity ratio λ for $\lambda = [0.01, 1.0]$, while for $\lambda = [10, 20]$ the opposite happens. For $\lambda = [0.01, 1.0]$, S_d reaches a steady state at $x_c = 6$. This again can be explained by considering the time τ needed by the droplet to deform from its undisturbed shape, which increases with an increase in viscosity ratio. The final value of S_d increases with an increase in the viscosity ratio.

The curvatures of the xz - and xy -profiles of the downstream tip of the droplets, \mathcal{C}_{xz}^d and \mathcal{C}_{xy}^d , are plotted in figure 2.21 (a) and (b) respectively. The curvatures \mathcal{C}_{xz}^d , \mathcal{C}_{xy}^d are scaled with the curvatures of the undeformed droplet $\mathcal{C}_{xz,0}^d$, $\mathcal{C}_{xy,0}^d$ respectively. From the plots of figure 2.21(a), we observe that \mathcal{C}_{xz}^d shows a sharp increase to a maximum when the droplet enters the flow intersection zone and then starts decreasing. Again the maximum value of \mathcal{C}_{xz}^d is dependent upon the viscosity ratio λ of the fluids and increases with an increase in λ for $\lambda = [0.01, 1]$, while for $\lambda = [10, 20]$ the opposite happens. This again can be explained by the time τ needed by a droplet to deform to its steady state shape. For small to moderate viscosity ratio of $\lambda = [10, 20]$, there is enough time for the droplet to deform and hence the maximum increases with an increase in λ , while for the very large viscosity ratio of $\lambda = [10, 20]$ the factor $(1+\lambda)$ becomes more dominant and hence a droplet with $\lambda = [10, 20]$ needs a longer time to deform.

The behavior shown for the curvature \mathcal{C}_{xy}^d of the xy -profile of the downstream droplet tip is more complicated. While the behavior of \mathcal{C}_{xy}^d is very similar to \mathcal{C}_{xz}^d for $\lambda = [0.1, 10]$, it shows completely different behavior for $\lambda = 0.01, 20$. The curvature \mathcal{C}_{xy}^d stay less than 1 after the start of the computations till $x_c = 6$.

Figure 2.22(a, b) shows the plots for curvatures \mathcal{C}_{xz}^u and \mathcal{C}_{xy}^u of the rear of the droplet. The curvatures \mathcal{C}_{xz}^u , \mathcal{C}_{xy}^u are scaled with the curvatures of their undisturbed values $\mathcal{C}_{xz,0}^u$, $\mathcal{C}_{xy,0}^u$ respectively. From figure 2.22(a) we observe that for $\lambda = [0.1, 1]$, \mathcal{C}_{xz}^u decreases after the start of computations, followed by a sharp increase to a maximum after the droplet leaves the flow intersection. There is no general trend in behavior for the curvatures of the upstream rear of the droplet. For the very small viscosity ratio of $\lambda = 0.01$, \mathcal{C}_{xz}^u reaches a steady state, which is smaller than

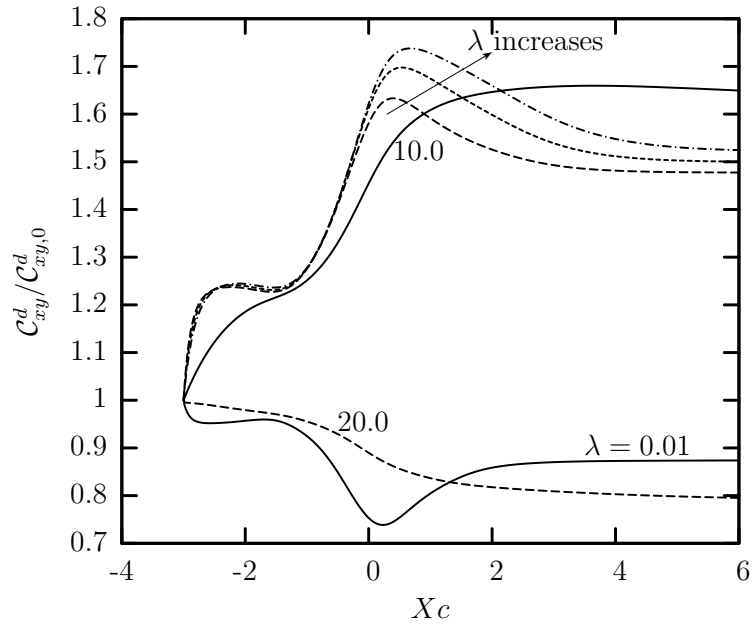
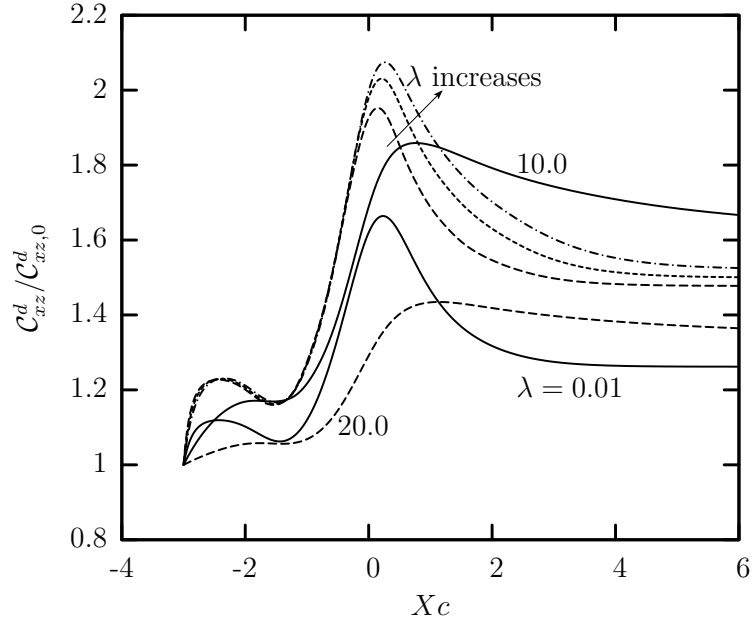


Figure 2.21: Curvatures of the downstream droplet tip as a function of the droplet centroid x_c for $Ca = 0.1$, $a = 0.7$, $q = 0.5$ and viscosity ratio $\lambda = 0.01, 0.1, 0.5, 1.0, 10.0, 20.0$. (a) Curvature of the droplet xz -profile C_{xz}^d . (b) Curvature of the droplet xy -profile C_{xy}^d .

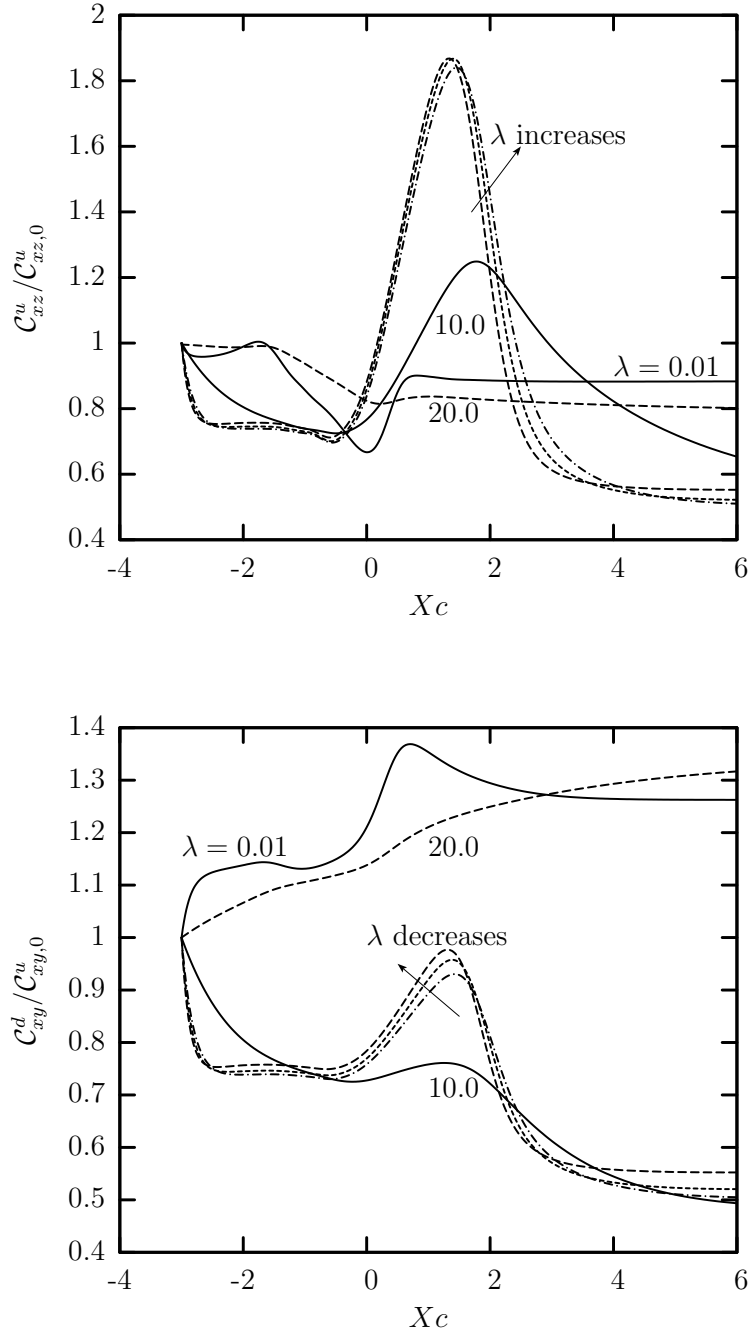


Figure 2.22: Curvatures of the upstream droplet tip as a function of the droplet centroid x_c for $Ca = 0.1$, $a = 0.7$, $q = 0.5$ and viscosity ratio $\lambda = 0.01, 0.1, 0.5, 1.0, 10.0, 20.0$. (a) Curvature of the droplet xz -profile C_{xz}^u . (b) Curvature of the droplet xy -profile C_{xy}^u .

the values for $\lambda = 0.01$, after the droplet crosses the flow intersection. For the large viscosity ratios of $\lambda = 10, 20$, the final value of $C_{xz,0}^u$ increases with an increase in λ . No general trend in behavior, with respect to viscosity ratio, is observed from the plots of C_{xy}^u shown in figure 2.22(b).

Figure 2.23(a) shows plots of droplet velocity U_x as a function of the droplet centroid x_c for the viscosity ratios studied. We observe that the droplet velocity U_x decreases with an increase in the viscosity ratio λ , for all values of x_c . After the droplet is released, U_x decreases till the droplet enters the flow intersection followed by a rapid increase to a maximum and then a subsequent decrease after the droplet exits the flow intersection. The rapid increase after the droplet enters the flow intersection is due to the flow coming in through the vertical branch channels. The influence of viscosity ratio λ on droplet velocity U_x is qualitatively similar to that reported by Wang and Dimitrakopoulos in their study of droplets in rectangular straight channels [48].

Figure 2.23(b) shows plots of additional pressure difference ΔP^+ for different viscosity ratios as a function of the droplet centroid x_c . It is observed that the additional pressure difference ΔP^+ increases with an increase in the viscosity ratio. This is because a stronger hydrodynamic force is needed for the deformation of a droplet with higher viscosity ratio.

Figure 2.24 shows the plots of the minimum distance h as a function of the droplet centroid x_c . We observe that the minimum distance increases sharply to a maximum when the droplet enters the flow intersection, which is followed by a decrease. The maximum value reached by h depends on the viscosity ratio λ . For the small to moderate viscosity ratios $\lambda = [0.01, 1]$, the maximum reached increases with an increase in the viscosity ratio λ . This again is because of the longer deformation time needed by a droplet with higher viscosity ratio.

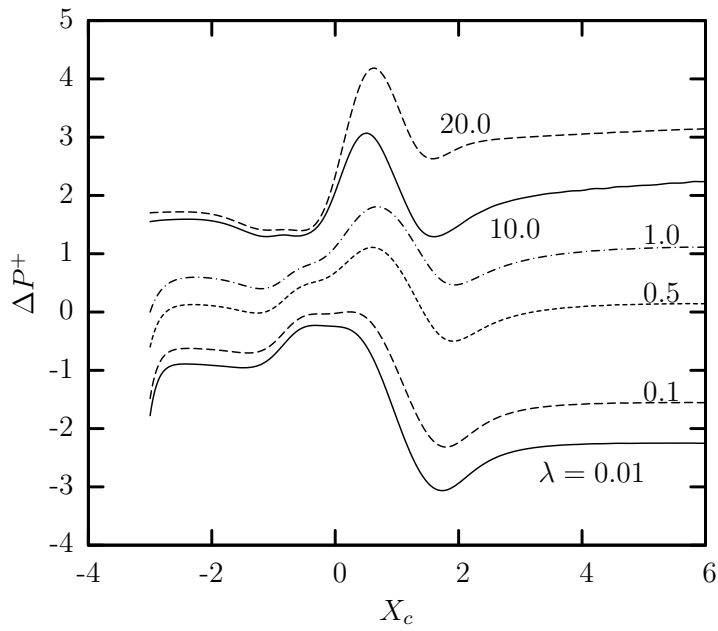
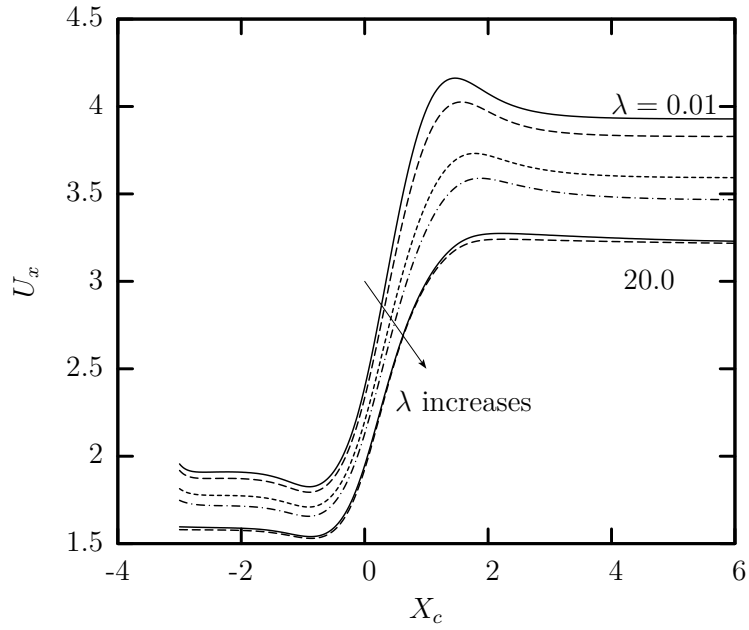


Figure 2.23: Droplet velocity and additional pressure difference as a function of the droplet centroid x_c for $Ca = 0.1$, $a = 0.7$, $q = 0.5$ and viscosity ratio $\lambda = 0.01, 0.1, 0.5, 1.0, 10.0, 20.0$. (a) Droplet velocity U_x . (b) Additional pressure difference ΔP^+ .

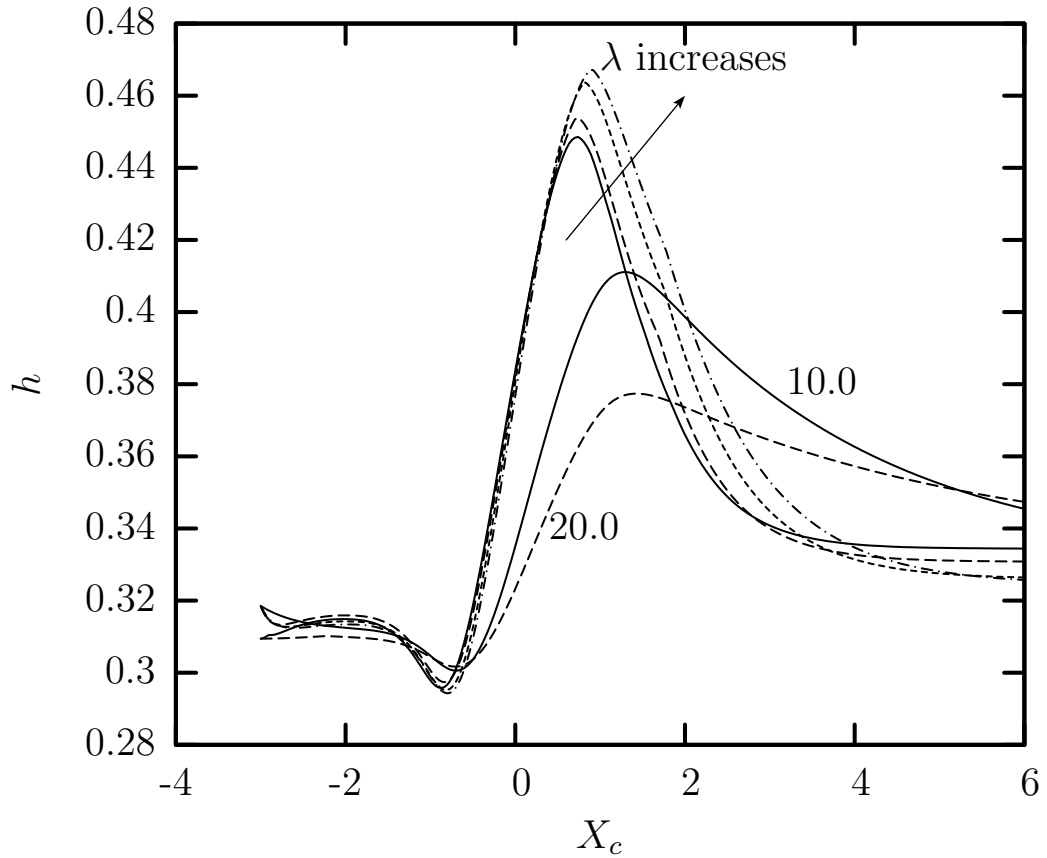


Figure 2.24: Minimum distance h of the droplet interface from the $z = -l_z$ wall of the junction as a function of the droplet centroid for $Ca = 0.1$, $a = 0.7$, $q = 0.5$ and viscosity ratio $\lambda = 0.01, 0.1, 0.5, 1.0, 10.0, 20.0$

2.5 Conclusion

In this chapter, we have investigated computationally the dynamics of microfluidic droplets in a cross-junction comprising of square channels. In particular, we have considered droplets with constant surface tension which are naturally buoyant in the surrounding fluid, and have size smaller than the cross-section of the square channels comprising the cross-junction. The study is motivated by a wide range of applications including direct contact heat-mass exchangers, encapsulation of reactants with droplets as microreactors, drug delivery methods, coating processes, and of course applications in energy, e.g. enhanced oil recovery processes and direct methanol fuel cells.

To our knowledge, this is the first work to systematically study the dynamics of droplets, without interfacial breaking, in a microfluidic cross-junction device. Our investigations complement earlier studies on formation of droplets in a microfluidic cross-junction and droplet motion in a straight rectangular microfluidic channel [9, 27, 41, 48]. We summarize briefly some of the more important conclusions.

(i) Our computations investigating the effects of flow rates in the channels of cross-junction, has revealed that the degree of interfacial deformation of the droplet, and hence its dynamics, depends on the strengths of flows in the channels of the cross-junction device. In general, upon release, the droplet takes the shape of a bullet before of the flow intersection with a pointed downstream tip and a flattened rear, so that to increase the restoring surface tension forces and thus balance the deforming hydrodynamic forces. When the droplet enters the flow intersection of the cross-junction device, its downstream tip becomes more pointed, and the rear flatter than before, to accomodate the incoming flows through the branch channels. When the droplet is completely in the zone of flow intersection, it becomes slender to due to the stronger hydrodynamic forces of the additional flow through the vertical branch channels. As the droplet moves further downstream, the droplet centroid moves towards the tip of the droplet, as now its tail becomes pointed while the downstream tip becomes relatively less pointed. At flow rates high enough, the rear

of the droplet may take a concave shape to balance the very strong hydrodynamic force with increased surface tension forces. As the droplet completely exits the flow intersection, it gradually regains a more deformed bullet shape far downstream owing to the higher total flow rate of all intersecting channels.

During this diverse interfacial evolution, the droplet lengths, tip curvatures, its velocity and the additional pressure difference change extensively, depending upon the droplet shape and location in the cross-junction device. We have monitored these parameters during the interfacial evolution of the droplet and have provided qualitative explanations.

(ii) Studying the effects of the droplet sizes on its dynamics, we observed that the minimum distance of the droplet interface from the junction wall plays a significant role in its interfacial evolution. The deformation of droplets with bigger size increases significantly, as the effective capillary number Ca^{eff} acting on the droplet increases. Before the flow intersection, the droplet develops a pointed downstream tip and a flattened rear. When the droplet is in the flow intersection of the cross-junction device, the tip of the droplet becomes more pointed, while the rear of droplet becomes very thin and wide due to incoming flows through the branch channels. We do not observe a concave rear for any of the droplet sizes studied.

(iii) We found the viscosity ratio of the fluids to strongly effect the dynamics of droplets in our cross-junction device. For low viscosity droplets, with λ up to $O(1)$, we found the droplet deformation to increase monotonically with an increase in viscosity ratio, owing to higher inner hydrodynamic forces. However, for high-viscosity droplets with $\lambda = O(10)$, the droplet deformation decreases significantly inside the cross-junction because the droplet does not have the time to accomodate the much slower deformation rate at high λ as it moves fast inside the microfluidic device. We note that, for high-viscosity droplets, the droplet deformation will eventually increase as the viscosity ratio is increased in the straight channel far downstream the cross-junction owing to higher inner hydrodynamic forces.

In addition, our study demonstrates the ability of our computational method to determine the droplet dynamics in intersecting flows accurately. With further

modification in geometry, even more complicated droplet dynamics may be accurately predicted.

Chapter 3

Droplet dynamics in a microfluidic T-junction

3.1 Introduction

The study of the dynamics of droplets has been a topic of extensive research for several decades because they are encountered in a large number of physical and chemical processes [42, 43]. There have been extensive experimental, theoretical and computational studies on the behavior of droplets submerged in another fluid. The growing interest in manipulation of microfluidic droplets is because of its applications in numerous areas ranging from direct contact heat/mass exchangers [30], encapsulation of reactants with droplets acting as micro-reactors [39] and improved drug delivery methods [49, 4]. The research on droplets include studies on formation of droplets [46, 27, 50], droplet deformation [19, 31, 20], bursting [3], coalescence of droplets [33, 53], adherence to solid boundaries [12, 13, 14] and splitting of droplets [5, 7]. For a summary on the current research and applications of microfluidics, the reader is referred to the review articles by Baroud, Gallaire and Dangla [2] and Solvas and deMello [38].

Besides microfluidics, understanding the behavior of non-wetting droplets has great importance in other industrial processes. In lubrication processes, lubricants usually contain a small amount of immersed bubbles which alter the performance of journal bearings and squeezing film dampers [37]. In enhanced oil recovery, foam is generated within the underground porous media during the displacement of oil [34]. An accurate estimation of the wetting film thickness between droplets composing the foam and the pore wall is desired in order to accurately predict the percentage

of recoverable oil. In coating processes, the wetting film thickness is also a direct measure of the load for coating the inner surface of monolithic channels [21, 22]. The physics of bubbles in microchannels is also essential in the operation design of fuel cells, e.g. the removal of CO_2 bubbles in the anode channel of a direct methanol fuel cell (DMFC) [28]. Understanding how bubbles/drops affect the flow resistance in microchannels is a concern for determining the pumping or energy requirement for portable microfluidic devices involving two-phase flows, such as in a direct methanol fuel cell [10].

Microfluidic T-junctions, along with cross-junctions, are one of the most commonly used devices for the production of uniformly sized droplets. T-junctions were first used by Thorsen *et al.* for formation of droplets [44]. Garstecki *et al.* identified a squeezing mechanism for the formation of drops for very low capillary numbers and provided scaling relationships to predict the size of droplets produced [17]. De Menech *et al.* used a phase field model to simulate the flow of two immiscible fluids and identified three distinct regimes of droplet formation: squeezing, dripping and jetting [11]. Christopher *et al.* experimentally studied the effects of viscosity and channel width ratios on droplet breakup in a T-junction and developed a scaling model. There have been extensive studies on the formation and breakup of droplets in microfluidic T-junctions [1, 25]. The critical parameter in certain microfluidic applications is the shape of the particle being transported. In drug delivery applications the surface area and the local curvature of the particle affects the adsorption of drugs [4]. Parameters like velocity, local curvature and surface area are direct functions of the shape of the droplet.

The deformation and displacements of droplets in confined microfluidic geometries when subjected to intersecting flows is a problem of considerable interest as such flow conditions occur in multi-phase flows in porous media and biological systems. Considerable progress has been made in understanding the deformation a single droplet in shear and extensional flows. A review of droplet dynamics in complex flows can be found in the review article by Cristini *et al.* [8]. However, there is very limited information available on the deformation of a single droplet

without breakup in a microfluidic T-junction. The goal of this current study is to develop a better understanding of the dynamics of droplets in a T-junction without interfacial breaking.

To address this issue, we study the dynamics of a single droplet moving along the centerline of a microfluidic T-junction. A three-dimensional spectral boundary element algorithm is used to compute the droplet deformation and motion under Stokes flow conditions in a microfluidic T-junction. We provide a detailed discussion of the junction geometry used in our computations in section 3.2.1. The mathematical formulation of the problem and the boundary conditions are discussed in section 3.2.2. The implicit interfacial spectral boundary-element method used in our computations is discussed in detail in section 3.3. We discuss the results obtained from our numerical calculations in section 3.4. In particular, we study the effects of flow rate, droplet size and viscosity ratio in three different subsections. A summary of our results is presented in section 3.5.

3.2 Mathematical Formulation and Computational Method

3.2.1 Problem Description

A schematic diagram of the T-junction employed in this work is shown in figure 3.1. The T-junction is constructed from intersecting square microfluidic channels. To facilitate our results description, we imagine that the main channel is horizontal, as illustrated in figure 3.1. Thus the flow direction (*i.e.*, the x -axis) corresponds to the channel's or droplet's length, the z -direction will be referred as height while the y -direction will be referred as width (of the channel or the droplet). Seeing the droplet from the positive y -axis, positive z -axis or negative x -axis, represents a front view, a top view or an upstream view, respectively. In addition, we adopt the standard definition of geometric shapes (polygons). Thus we call the droplet's rear edge as convex when the radius of curvature at the middle of the rear edge points inside the capsule (*i.e.*, the local curvature is positive); in the opposite case the edge shape is concave. In general, the half length l_x of the horizontal main channel of the

junction along the x -axis is 9 units. The half lengths of the square cross-section of the main channel, along the y and z -axes are l_y and l_z respectively, with $l_y = l_z = 1$. The length of the vertical branch channel along the positive z -axis is four unit. The origin of the system is placed at the center of the junction.

The droplet (fluid 1) with a density ρ_1 and viscosity $\lambda\mu$ is naturally buoyant in the surrounding fluid (fluid 2) with density ρ_2 and viscosity μ , as $\rho_1 = \rho_2$. The surface tension γ is assumed to be constant throughout the surface of the droplet. The undeformed spherical droplet, at the start of our computations, has a radius a with volume $V = \frac{4}{3}\pi a^3$. The surrounding fluid flows in to the junction towards the junction center through the square cross sections at $-x$, and $+z$ -axes. The incoming flow of the surrounding fluid through the square cross sections at $-x$, upstream of the droplet is the undisturbed flow of fluid through a square channel with an average velocity of \mathcal{U} . The flow of the fluid coming in through the square cross section of the vertical branch channel along the $+z$ -axis is a fraction q of the fluid flow through the main channel of the junction, *i.e.*, the average velocity of the fluid through the vertical channel is $q\mathcal{U}$. At the start of our computations the spherical droplet is placed inside the horizontal channel upstream of the junction. Due to the nonsymmetric nature of the system and the flow, unlike in a straight channel or a cross junction, the droplet velocity along the z -axis is nonzero. As the droplet deforms, it moves downstream through the horizontal main channel. Due to the presence of nonsymmetric intersecting flow, the droplet deformation varies by a great margin to that of deformation of a single droplet in a straight channel or cross junction, under similar external shear and other physical conditions.

The major parameters of interest in this study are the strength of flow rate in the horizontal main channel, viscosity ratio and the size of droplets. Figure 3.2(a) shows the three-dimensional figure of an undeformed droplet while figure 3.2(b) shows a three-dimensional view of a cross junction with the $-y$ elements removed.

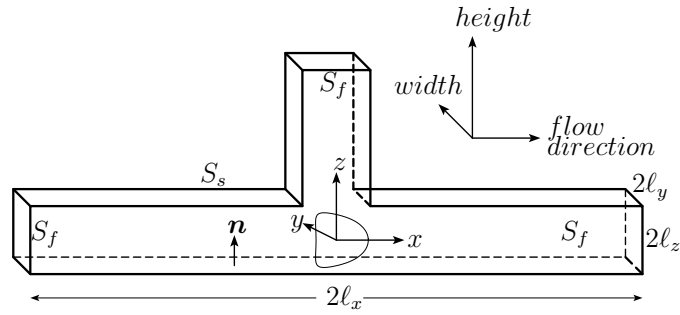


Figure 3.1: Schematic illustration of the geometry of T-junction.

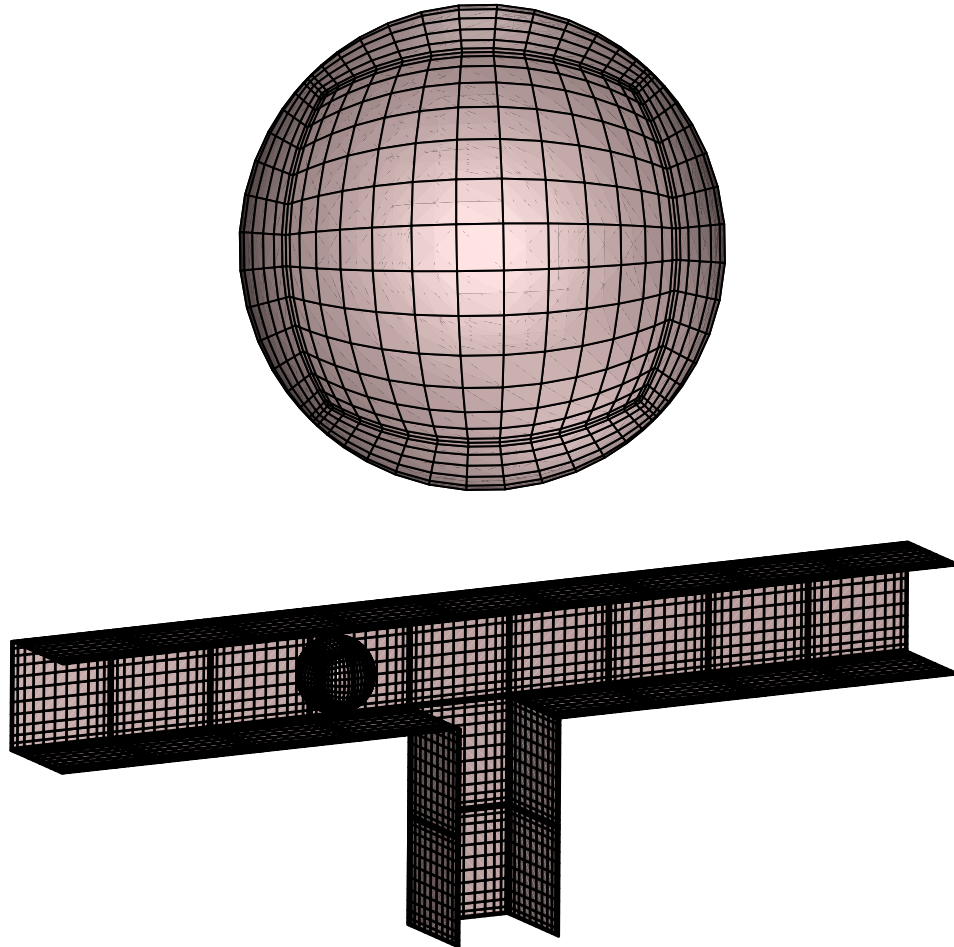


Figure 3.2: Three-dimensional figures of an undeformed droplet and the T-junction used in our computations.

3.2.2 Fluid Dynamics

Due to the very small length scales involved with droplet flow in microfluidics junctions, the Reynolds number is very small and the inertial terms in the Navier-Stokes equations can be neglected. The flow is governed by Stokes equations

$$\nabla \cdot \boldsymbol{\sigma} \equiv -\nabla p + \mu \nabla^2 \mathbf{u} = 0 \quad (3.1)$$

and the continuity equation

$$\nabla \cdot \mathbf{u} = 0 \quad (3.2)$$

where $\boldsymbol{\sigma}$ is the stress tensor, p is the dynamic pressure and \mathbf{u} is the velocity vector.

In this study, the system surface S_B consists of droplet surface S_d , the solid surface of the junction S_s , the fluid surfaces S_f of the junction's inlets and the outlet. At the droplet surface the velocity is continuous and there is an interfacial stress jump owing to the surface tension. As the density of both fluids are same, the contribution of gravity to the interfacial stress jump is zero and thus the boundary conditions on the droplet surface are,

$$\mathbf{u}_1 = \mathbf{u}_2 \quad \text{and} \quad \Delta \mathbf{f} \equiv \mathbf{f}_2 - \mathbf{f}_1 = \gamma \nabla \cdot \mathbf{n} \quad (3.3)$$

Here the subscripts designate quantities related to the fluids 1 and 2 respectively, while \mathbf{n} is the unit normal pointing from the droplet interface into fluid 2. The boundary conditions on the rest surfaces are,

$$\mathbf{u} = 0 \quad \text{on the solid boundary } S_s, \quad (3.4)$$

$$\mathbf{u} = \mathbf{u}^\infty \quad (3.5)$$

where \mathbf{u}^∞ is the undisturbed channel velocity far from the droplet.

The undisturbed velocity profile for flow through a rectangular channel along x -axis, far from the droplet, can be found in the book by Yih [51], which is,

$$\frac{u^\infty(x)}{\Upsilon} = (l_z^2 - z^2) + \sum_{m=1}^{\infty} B_m \cosh\left(\frac{b_m y}{l_z}\right) \cos\left(\frac{b_m z}{l_z}\right), \quad (3.6)$$

where

$$\begin{aligned} \Upsilon &= -\frac{1}{2\mu}, \quad b_m = \frac{(2m-1)\pi}{2}, \quad \text{and} \\ B_m &= \frac{(-1)^m 4l_z^2}{b_m^3 \cosh(\frac{b_m l_y^2}{l_z})} \end{aligned} \quad (3.7)$$

while p is the dynamic pressure. The volumetric flow rate Q can be obtained by integrating over the cross-section, which is,

$$\frac{Q}{\Upsilon} = \frac{8l_y l_z^3}{3} + \sum_{m=1}^{\infty} B_m \left(\frac{2l_z}{b_m}\right)^2 \sinh\left(\frac{b_m l_y}{l_z}\right) \sin(b_m) \quad (3.8)$$

In our study, the incoming flows through the vertical branch channel is half as strong as the flow through the main horizontal channel. The velocity profile from the main channel is copied to the branch channel and scaled after accounting for the direction of flow. Far from the droplet, the average velocity of the undisturbed flow is $\mathcal{U} = Q/(l_y l_z)$, while the maximum undisturbed velocity at the centerline of the square channel is $\mathcal{U}_{max}/\mathcal{U} \approx 2.096$.

In this study, if no scale is present, the horizontal channel's half-height l_z is used as the length scale, the velocity is scaled with the average undisturbed velocity \mathcal{U} , and thus time is scaled with $\tau_f = l_z/\mathcal{U}$.

Based on standard boundary integral formulation, the velocity at a point \mathbf{x}_0 on the system surface S_B may be expressed as a surface integral of the force vector $\mathbf{f} = \mathbf{n} \cdot \boldsymbol{\sigma}$ and the velocity \mathbf{u} over all points \mathbf{x} on the boundary S_B ,

$$\begin{aligned} \Omega \mathbf{u}(\mathbf{x}_0) &= - \int_{S_c} [\mathbf{S} \cdot (\Delta \mathbf{f} - \mu(1-\lambda)\mathbf{T} \cdot \mathbf{u} \cdot \mathbf{n})](\mathbf{x}) dS \\ &\quad - \int_{S_s \cup S_f} (\mathbf{S} \cdot \mathbf{f} - \mu \mathbf{T} \cdot \mathbf{u} \cdot \mathbf{n})(\mathbf{x}) dS \end{aligned} \quad (3.9)$$

where the coefficient Ω takes values $4\pi\mu(1+\lambda)$ and $4\pi\mu$ for points \mathbf{x}_0 on the surfaces S_d and $S_s \cup S_f$ respectively. The tensors \mathbf{S} and \mathbf{T} are the fundamental solutions for the velocity and stress for the three-dimensional Stokes equations, i.e., known functions of the system surface S_B [13]. More details on physical variables can be found in the article by Kuriakose and Dimitrakopoulos [23].

3.3 Implicit Interfacial Spectral Boundary-Element Method

The boundary integral equation, Eq.(3.9), was solved using our three-dimensional fully-implicit interfacial spectral boundary-element method. The boundary is divided into a number N_E of surface elements, each of which is parametrized by variables η and ξ on a square domain of $[-1, 1]^2$. The geometry and physical variables are discretized using Lagrangian interpolation in terms of these parametric variables. The number N_B of basis points (η_i, ξ_i) chosen for interpolation are zeros of orthogonal polynomial. Any point \mathbf{x} on the geometry can be represented by

$$\mathbf{x}(\xi, \eta) = \sum_{i=1}^{N_B} \sum_{j=1}^{N_B} \mathbf{x}(\xi_i, \eta_i) h_i(\xi) h_j(\eta) \quad (3.10)$$

Similarly the physical variables \mathbf{u} and \mathbf{f} can be interpolated at any point \mathbf{x} from their values at the basis points.

Two types of points are used in solving the boundary integral equation by our spectral element method, the collocation points \mathbf{x}_0 where the equation is required to be satisfied and the basis points \mathbf{x} where the physical variables \mathbf{u} and \mathbf{f} are specified. The collocation points \mathbf{x}_0 are of Legendre-Gauss quadrature where the points lie on the interior of the spectral elements. Thus the boundary integral equation is valid even at corners of singular elements. The basis points \mathbf{x} are of Legendre-Gauss-Lobatto quadrature and thus the physical variables are defined in the interior and edges of the spectral elements. Further details on the discretization of system surfaces can be found in these earlier papers [47, 15].

The transformation of the Stokes equations into boundary integral equations and solution by an explicit time integration method has been a common method to determine the droplet shape as a function of time since the pioneering work of Acrivos and coworkers [52, 36]. This results in a great reduction in computational time as a three-dimensional problem can be described and solved using only two curvilinear coordinates. However, the explicit time integration requires a time step smaller than any time scale (numerical and physical) appearing in the problem. To

ensure stability the time step employed has to satisfy the following condition,

$$\Delta t < O(Ca \Delta x_{min}) \quad (3.11)$$

where Δx_{min} is the minimum grid spacing in the computational problem [35, 54]. Dimitrakopoulos developed an efficient, fully-implicit time-integration algorithm for interfacial dynamics in Stokes flow to avoid the computational cost associated with small time steps [15]. This method is based on a mathematically rigorous combination of implicit schemes with the Jacobian-free three-dimensional Newton method developed by Dimitrakopoulos and Higdon [13]. Both multi-step (one-stage) implicit formulae (e.g. Euler and backward differentiation schemes) and multi-stage diagonally implicit Runge-Kutta schemes are employed. By the combination of the an implicit scheme with the Newton method, the interfacial algorithm preserves the stability properties of the corresponding implicit formula, and hence permits the use of very large time steps. In addition, sufficient accuracy can be easily achieved, even with larger time steps, by employing high-order implicit schemes. In this work we use a third-order diagonally implicit Runge-Kutta scheme (DIRK3) with $\Delta t = 10^{-2}$.

By combining the implicit interfacial method with the spectral boundary-element algorithm, the resulting algorithm exploits all the benefits of the spectral methods, i.e., high-order interpolation with exponential convergence and numerical stability with increasing number of spectral points, along with the versatility of the boundary-element method, i.e., the ability to handle the most complicated geometries. In addition, it is not affected by the disadvantage of the spectral methods used in volume discretization; namely the requirement to deal with dense systems, because in boundary-integral formulations the resulting systems are always dense, independent of the form of discretization. We note that the exponential convergence in the numerical accuracy is evident at both the properties of a given shape, such as the interfacial curvature, and the dynamic evolution of the interfacial shape. For more details the reader is directed to the article by Dimitrakopoulos [15].

In our study, the horizontal main channel of the cross-junction is divided into

nine rows with four rows upstream and downstream of the junction, while the vertical branch channel is two-rows long. Each row of the channels are represented by four surface elements, with one element representing a side of the row. Thus the solid walls of the cross junction are divided into forty three elements. In addition the three fluid surfaces for entrance and exit of fluids into the channel are represented by one element each. The droplet surface is divided in a minimum of six elements by cube projection, with each element corresponding to a side of the cube. Our method is also capable of generating more surface elements on the droplet surface and more than one elements per row for each channel side. In most of our computations, we have used ten surface elements for capturing the droplet shape. However, for handling complex shapes of the deformed droplets for high Ca we have used up to 22 surface elements with progressive splitting of an element at the tip of the droplet into five elements. Such discretizations are not needed in most of the cases as the method is accurate, as shown from our convergence runs.

In most of our computations, we utilized $N_B = 8$ basis points on each element. As we have N_E number of surface elements and N_B^2 points per spectral elements, we finally have a system of $3N_EN_B^2$ algebraic equations. For verification of accuracy of our results, we performed some runs with $N_B = 10$ basis points for moderate and high Ca and high droplet sizes a . The convergence runs showed that $N_B = 8$ is sufficient enough to capture the shape of the deformed droplets except for the case with large $Ca = 0.4$.

In all our computations carried out in this chapter, we exploited the symmetry level $z = 0$. Exploiting the symmetry reduce the memory requirements for storage of the system by a factor of 4, the computational time for calculating the system matrices by a factor of 2 and the solution time via direct system solvers by factor of 8.

3.4 Results

In this section, we discuss the results obtained from our numerical computations. The study covers a wide range of flow rates, viscosity ratios and droplet sizes. The computations are started with a spherical droplet which deforms as it moves downstream. Similar to our computations on cross-junction, in all our computations in this chapter, we fix any two of Ca , λ , a at $Ca = 0.1$, $\lambda = 0.2$, $a = 0.7$ and vary the third one over a wide range to study its effects on droplet deformation. At the beginning of all computations, we place the droplet at the center of the horizontal main channel of the T-junction device, at a position of $x_c = -3.0$. After the start of computations, the droplet deforms as it starts flowing downstream due to flow initiation. We compute the droplet dynamics until the droplet centroid reaches $x_c = 8.0$. However, we plot the results of our computations only when the the droplet centroid is in the range of $x_c = [-3.0, 6.0]$ as our main focus is on the dynamics of the droplet near the center of the T-junction where the flow intersection occurs. Also we plot the results as a function of the droplet centroid x_c .

The three-dimensional shapes of a droplet in a T-junction, at different locations of the droplet centroid x_c , are shown in figure 3.3. The three-dimensional views presented here were derived from the actual spectral grid by spectrally interpolating to $N_B = 14-16$. The first shape in figure 3.3 shows the undeformed droplet at the start of the computation, with its centroid at $x_c = -3.0$. After the start of computation, the droplet starts flowing downstream and deforms due to the hydrodynamic forces acting on it. The droplet assumes a bullet shape, similar to a droplet in a cross-junction, with a pointed downstream tip and a flattened rear, while still upstream of the flow intersection. The droplet takes the shape of a bullet as it tries to balance the hydrodynamic forces and the surface tension forces. Again, this can be explained by putting an observer at the center of the droplet, assuming a static frame of reference for the observer. In this case the fluid is flowing upstream in the junction. With a spherical droplet the net surface tension forces is zero. The surface tension force acting at a point on the droplet surface is inversely proportional to its

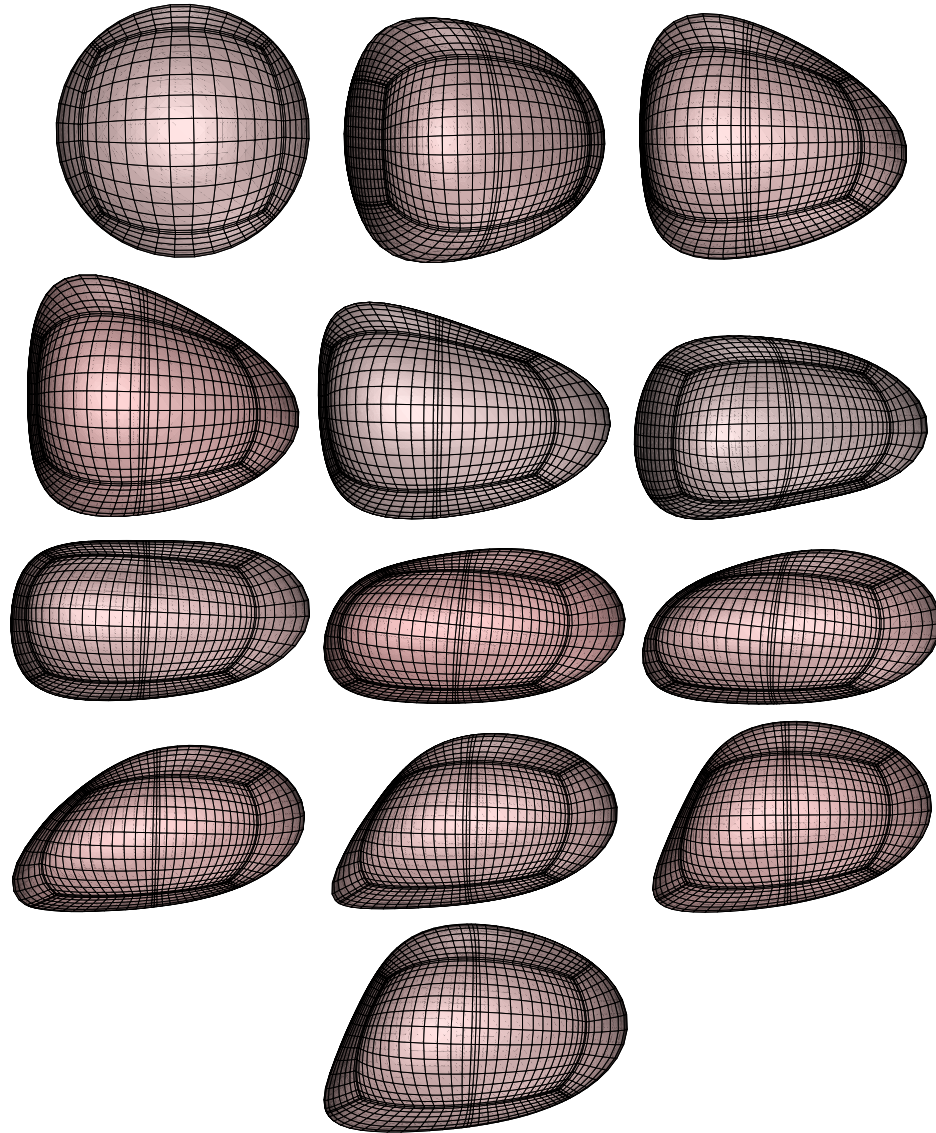


Figure 3.3: Three-dimensional shapes of a droplet (plotted row-wise) with $Ca = 0.4$, $\lambda = 0.2$, $a = 0.7$, $q = 0.5$ in a T-junction at $x_c = -3.0, -1.74, -0.53, -0.37, 0.12, 0.49, 0.90, 1.34, 1.57, 2.26, 3.4, 4.5, 4.9$.

radius of curvature and can be written as

$$F_\gamma \sim \frac{\gamma}{R} \quad (3.12)$$

where R is the radius of curvature of the point on the droplet. As the tip of the droplet becomes pointed and the rear flatter, there is a net surface tension force on the droplet

$$F_\gamma \sim \gamma \left(\frac{1}{R_1} - \frac{1}{R_2} \right) \quad (3.13)$$

where R_1 and R_2 are the radius of curvatures of the center of the tip and the rear of the droplet. This quantity is positive as R_1 is smaller than R_2 .

When the tip of the droplet enters the flow intersection, with its rear still upstream of the flow intersection, its rear becomes flatter, while its tip becomes more pointed and skewed towards the $z = -l_z$ wall of the T-junction as the droplet experiences a stronger hydrodynamic force due to flow coming in through the vertical branch channel of the T-junction, as shown in the third shape of figure 3.3. This causes the droplet centroid x_c to move towards the rear of the droplet. As the drop moves further inside the flow intersection, its tip becomes more pointed as seen in the fourth shape of figure 3.3. The fifth shape of figure 3.3 shows the droplet, with a very pointed tip and a highly flattened rear, when it is completely within the flow intersection. As the droplet moves further downstream, with its rear is still inside the flow intersection while its tip is outside, the droplet becomes bent, as shown in the sixth shape of figure 3.3, to accommodate the flow through the vertical branch channel. The droplet becoming bent is a direct result of the lack of symmetry of flow around the xy -plane of the junction. We observe from the seventh shape of figure 3.3 that skewed tip of the droplet gradually starts moving away from the $z = -l_z$ wall of the T-junction device while its rear becomes thinner, as the droplet moves further downstream with its rear still inside the flow intersection. As the downstream tip of the droplet starts moving towards the centerline of the horizontal main channel, i.e., the x -axis, the rear of the droplet gradually becomes more pointed and skewed towards the $z = -l_z$ wall of the junction, as seen from the eighth and ninth shapes of figure 3.3. As the droplet completely exits the flow intersection the droplet assumes a

slipper shape with a rear which is very pointed and skewed towards the $z = -l_z$ wall of the T-junction, as seen in the tenth and eleventh shape of figure 3.3. Gradually the droplet starts becoming less deformed, as it moves further away from the flow intersection, with both its tip and rear becoming less pointed, as seen in the twelfth and thirteenth shape of figure 3.3, and finally exit the junction.

3.4.1 Effect of flow rate

In this section, we collect the results of our computations studying the effects of varying flow rates in the channels of our T-junction device. We vary the flow rate in the horizontal main channel of the junction, while maintaining fraction of flow rate in the vertical branch channel at $q = 0.5$. A spherical droplet with viscosity ratio $\lambda = 0.2$ and size $a = 0.7$ is placed upstream of the junction at $x_c = -3.0$ and the capillary number Ca varies in the range $[0.01-0.4]$. From our computations we found that the droplet deformation depends strongly on Ca .

Figure 3.4 shows the droplet lengths L_x along the flow direction as a function of the droplet centroid position x_c . We observe, from figure 3.4(a), that the droplet length L_x increases with an increase in flow rate. After the droplet is released in the horizontal main channel, at first L_x shows a small decrease, owing to the formation of the bullet shape, followed by a slow increase as the droplet moves towards the flow intersection. This is followed by a rapid increase in L_x after the droplet enters the flow intersection of the T-junction device. L_x reaches a maximum after the droplet centroid x_c crosses the flow intersection and then rapidly starts decreasing as the droplet moves in to the horizontal channel downstream of the flow intersection. For the very small $Ca = 0.01$, L_x decreases to a steady state downstream of the flow intersection. We also observed from our computations that for all other Ca , L_x does not reach steady state by the time it reaches the end of our T-junction device. In addition, for the range of Ca studied in this chapter, none of the droplets break inside the junction channel.

We also divide the total droplet length L_x into two components, the upstream and downstream droplet lengths, L_x^u and L_x^d , (calculated from the droplet centroid

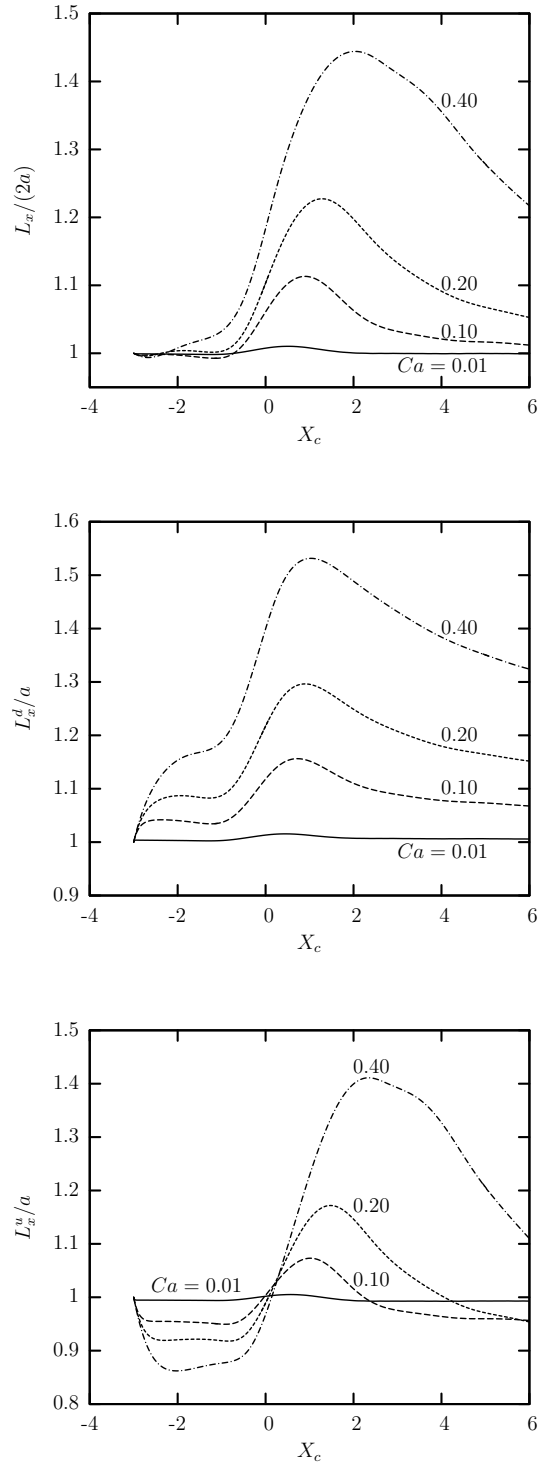


Figure 3.4: Droplet lengths along the flow direction as a function of the droplet centroid x_c for $\lambda = 0.2$, $a = 0.7$, $q = 0.5$ and capillary number $Ca = 0.01, 0.1, 0.2, 0.4$. (a) Droplet length L_x . (b) Downstream droplet length L_x^d . (c) Upstream droplet length L_x^u .

x_c to the rear and front tips of the droplet), and plot them separately in figure 3.4(b, c) as a function of the droplet centroid x_c . It is observed, from figure 3.4(b, c), that before the droplet centroid crosses the center of the cross-junction, they exhibit different behavior, whereas their behavior after that is similar. The upstream droplet length L_x^u at first decreases, and then starts increasing till it reaches a maximum. This initial decrease in L_x^u is because of the appearance of the flattened rear in the bullet shaped droplet, as shown in the third shape of figure 3.3, which causes the droplet's centroid to move backwards. The downstream length of the droplet L_x^d increases, at first slowly and then rapidly till it reaches a maximum, which is again followed by a sharp decrease. This can be attributed to the evolution of the pointed downstream tip in the bullet shaped droplet. The rapid increase in L_x^u and L_x^d is due to the lengthening of the droplet by stronger hydrodynamic forces caused by the additional flow through the vertical branch channel of the T-junction. After reaching a maximum, both L_x^u and L_x^d start decreasing rapidly as the droplet moves further downstream. The decrease in L_x^d is more rapid than that of L_x^u as the droplet centroid x_c moves towards the downstream tip of the droplet in the slipper shaped droplet. In addition, we observe that the final value attained by L_x^u , at $x_c = 6.0$, is higher than the final value of L_x^d due to relative lengthening of the upstream portion of the slipper shaped droplet. The final values of both L_x^d and L_x^u are greater than 1 for all Ca studied.

In figure 3.5 (a) and (b) we plot L_y and L_z , *i.e.*, the droplet lengths along the y - and z -axes respectively as a function of droplet centroid x_c . We observe, from figure 3.5(a,b), that L_y and L_z remain largely unchanged at the very small $Ca = 0.01$ as the droplet undergoes a very small deformation. For all other capillary numbers studied, L_y starts decreasing slowly upstream of the flow intersection, followed by a rapid decrease as the droplet enters the flow intersection. On the other hand, L_z shows a small initial decrease, which is followed by another small increase before the droplet enters the flow intersection. This is due to the formation of the bullet shape and its shortening as the downstream tip of the droplet reaches the flow intersection. L_y and L_z both decrease rapidly under increased hydrodynamic forces due to the

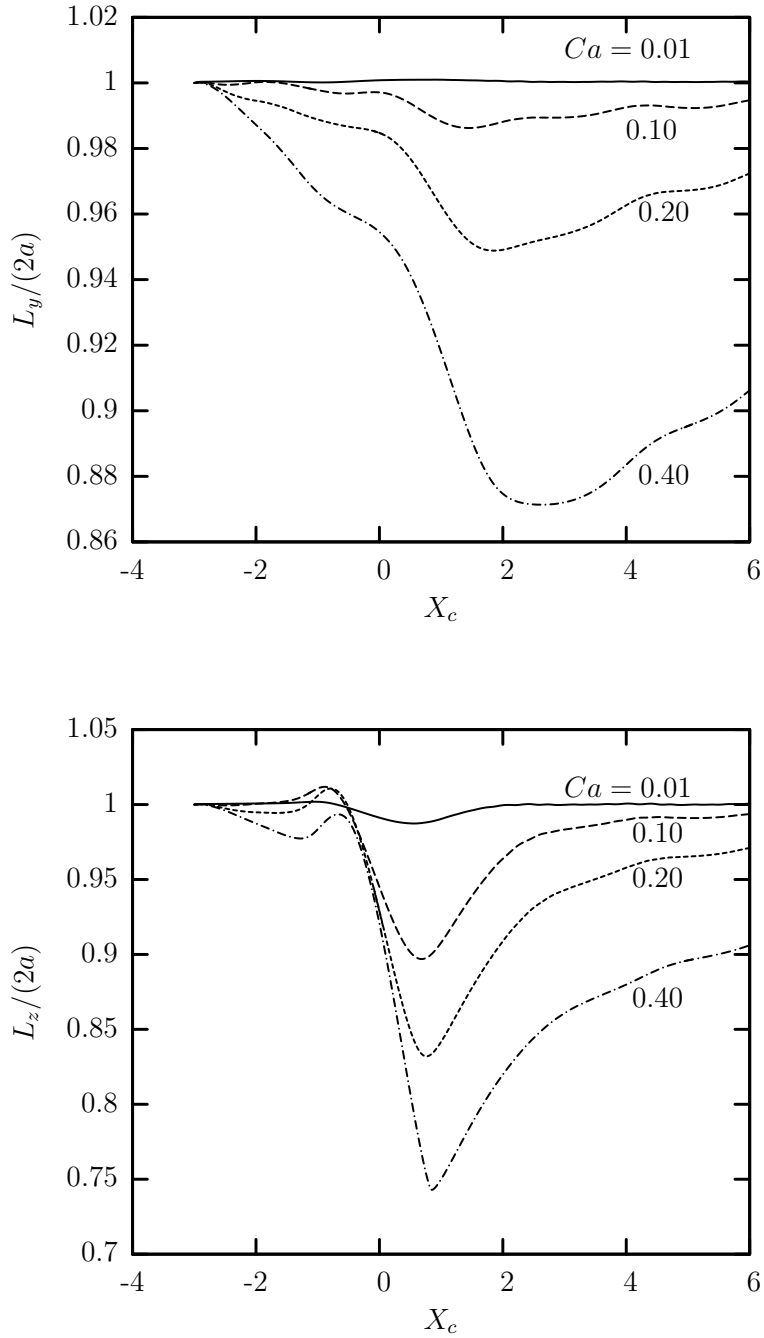


Figure 3.5: Droplet lengths along the y - and z -axes as a function of the droplet centroid x_c for $\lambda = 0.2$, $a = 0.7$, $q = 0.5$ and capillary number $Ca = 0.01, 0.1, 0.2, 0.4$. (a) Droplet length along the y -axis $L_y/(2a)$. (b) Droplet length along the z -axis $L_z/(2a)$.

additional flow coming in through the vertical branch channel of the droplet, as the droplet enters the flow intersection, L_y and L_z both reach minimum downstream of the junction and then start increasing again as the droplet tries to regain its shape from the highly deformed slipper shape. For $Ca = [0.1, 0.4]$, L_y and L_z do not reach steady states as the interfacial evolution of the droplet continues till it reaches $x_c = 6.0$.

We plot the surface area of the deformed droplet S_d , as a function of the droplet centroid x_c , in figure 3.6. The surface area of the deformed droplet S_d is scaled with the undeformed surface area of the originally spherical droplet S_d^0 . For $Ca = 0.01$, S_d remains largely unchanged as the droplet does not undergo any appreciable deformation at such a low flow rate. For all other capillary numbers of $Ca = [0.01, 0.4]$, it is observed that the surface area of the droplets increases with an increase in the flow rate. After a small initial decrease in S_d , upstream of the flow intersection, is followed by a rapid increase inside the flow intersection until it reaches a maximum downstream of the junction. This rapid increase again is due to stronger hydrodynamic forces acting on the droplet due to the flow coming in through the vertical branch channel. With an increase in the flow rate, the hydrodynamic force acting on the droplet increases making the slipper shaped droplet longer, which in turn increases the total surface area of the droplet. As the slipper shaped droplet tries to regain its shape, downstream of the flow intersection, S_d starts decreasing rapidly. In addition, S_d does not reach a steady state by the time the droplet centroid is at $x_c = 6.0$, as the interfacial evolution of the interfacial evolution of the droplet is still not completed.

The curvature of the xz -profile at the center of the downstream droplet tip, \mathcal{C}_{xz}^d is plotted in figure 3.7. The curvature \mathcal{C}_{xz}^d is scaled with the curvature of the undeformed spherical droplet $\mathcal{C}_{xz,0}^d$. We observe from the plots that, after the flow initiation, \mathcal{C}_{xz}^d increases owing to the formation of the pointed downstream tip of the droplet. This is followed by a rapid increase in \mathcal{C}_{xz}^d as the downstream droplet tip enters the flow intersection and becomes more pointed. The curvature \mathcal{C}_{xz}^d reaches a maximum when the droplet centroid is slightly downstream of the junction center.

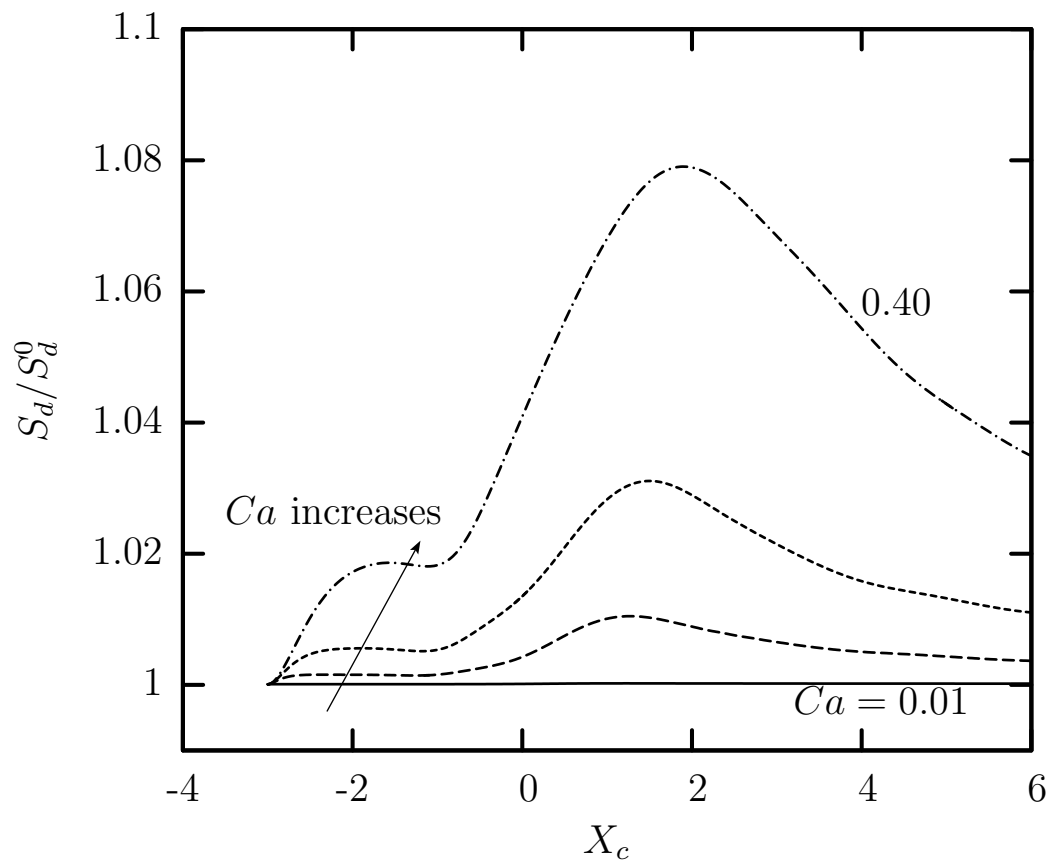


Figure 3.6: Surface area of the droplet (scaled with its undisturbed value) S_d/S_d^0 as a function of the droplet centroid x_c for $\lambda = 0.2$, $a = 0.7$, $q = 0.5$ and capillary number $Ca = 0.01, 0.1, 0.2, 0.4$.

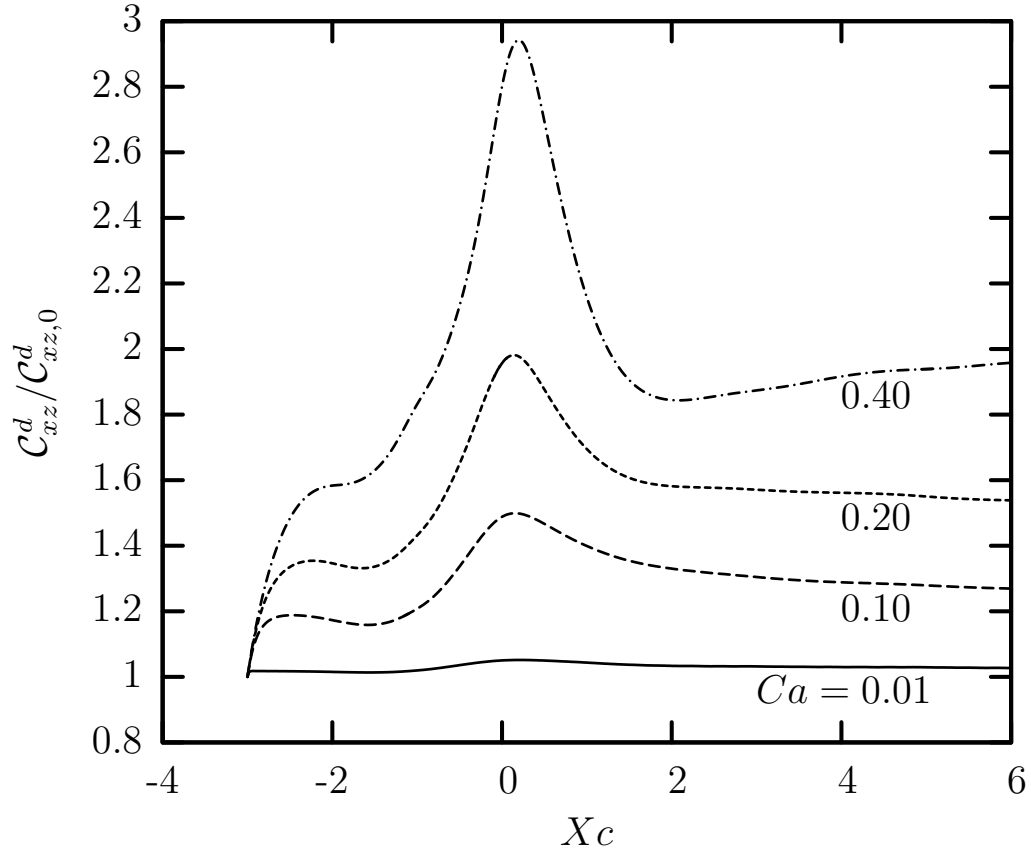


Figure 3.7: Curvature of the xz -profile at the center of the downstream droplet tip (scaled with its undisturbed value) $C_{xz}^d/C_{xz,0}^d$ as a function of the droplet centroid x_c for $\lambda = 0.2$, $a = 0.7$, $q = 0.5$ and capillary number $Ca = 0.01, 0.1, 0.2, 0.4$.

After the downstream droplet tip exits the flow intersection and the droplet assumes the slipper shape, \mathcal{C}_{xz}^d starts decreasing as the downstream droplet tip gradually becomes less pointed. The final value for \mathcal{C}_{xz}^u increases with an increase in Ca .

Figure 3.8 shows the curvature of the xz -profile at the center of the rear of the droplet, \mathcal{C}_{xz}^u , as a function of the droplet centroid x_c . The curvature \mathcal{C}_{xz}^u is scaled with the curvature of the undeformed spherical droplet $\mathcal{C}_{xz,0}^u$. The behavior of the curvature \mathcal{C}_{xz}^u for the rear of the droplet is more complicated than the curvature of the downstream droplet \mathcal{C}_{xz}^d . As the droplet deforms, while moving from through the main channel, the rear of the droplet undergoes a continual change in its shape. For the small $Ca = 0.01$, \mathcal{C}_{xz}^u stays very close to 1, as the droplet is largely undeformed. For all other capillary numbers studied, \mathcal{C}_{xz}^u shows a sharp initial decrease due to the formation of the flattened rear in the bullet shaped droplet. As the droplet moves into the flow intersection, the shape of the droplet changes from a bullet to a bent bullet, as shown in 3.3. This change in shape is the reason behind the rapid increase in \mathcal{C}_{xz}^d , as seen in figure 3.8. However, after the formation of the slipper shaped droplet the curvature at the center of the rear decreases rapidly, as the center of the droplet rear becomes flat, while the pointed shape occurs near to the edge of the droplet rear. The final value of \mathcal{C}_{xz}^d , at $x_c = 6.0$ decreases with an increase in Ca , as the center of the droplet rear becomes more flattened, with the edge becoming more pointed, to balance the stronger hydrodynamic forces with the restoring surface tension forces.

We plot the droplet velocities, U_x and U_z , as a function of the droplet centroid x_c , in figure 3.9(a) and (b) respectively. After the start of computation, as the droplet moves through the horizontal main channel, the droplet centroid deviates from the centerline of the main channel. As the droplet enters the flow intersection its velocity in the flow direction, U_x , increases significantly, as seen in figure. 3.9(a). However, due to the incoming flow through the vertical branch channel, the droplet also gets pushed towards the $z = -l_z$ wall of the T-junction. The magnitude of droplet velocity along the z -axis, U_z , also increases after the droplet enters the flow intersection, and starts decreasing as the droplet experiences a lateral migration

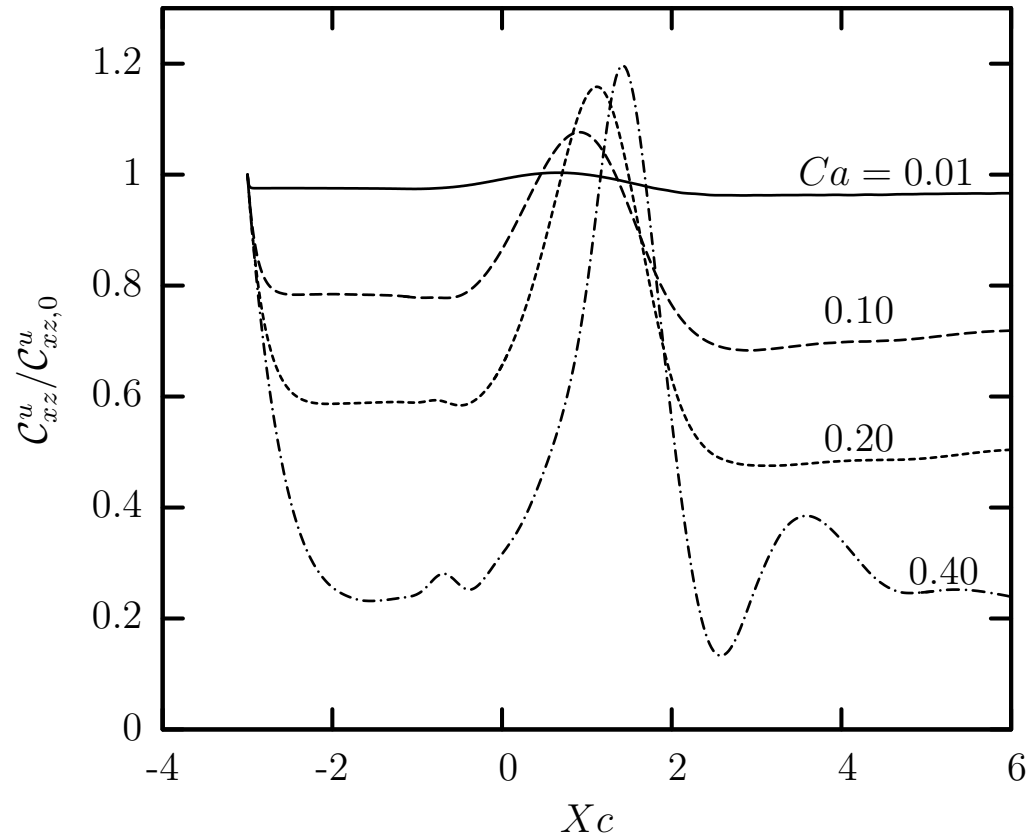


Figure 3.8: Curvature of the xz -profile at the center of the upstream droplet rear (scaled with its undisturbed value) $C_{xz}^u/C_{xz,0}^u$ as a function of the droplet centroid x_c for $\lambda = 0.2$, $a = 0.7$, $q = 0.5$ and capillary number $Ca = 0.01, 0.1, 0.2, 0.4$.

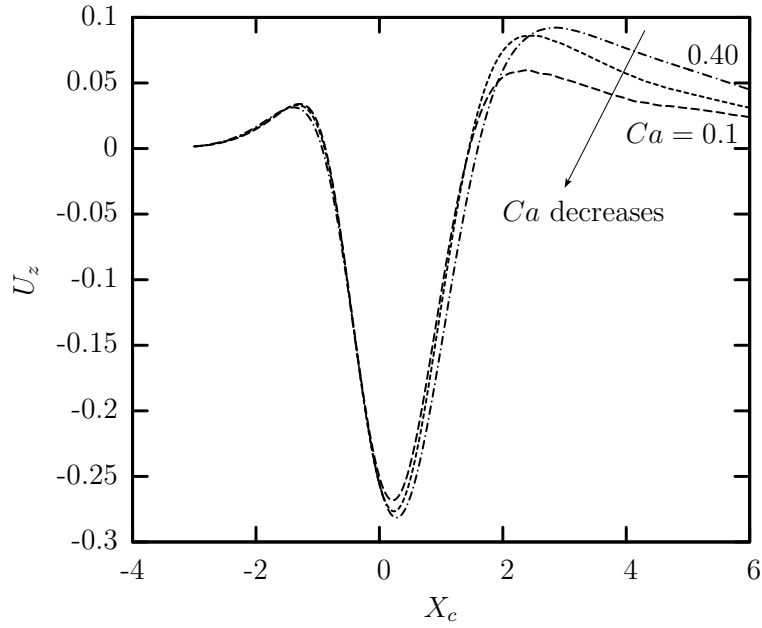
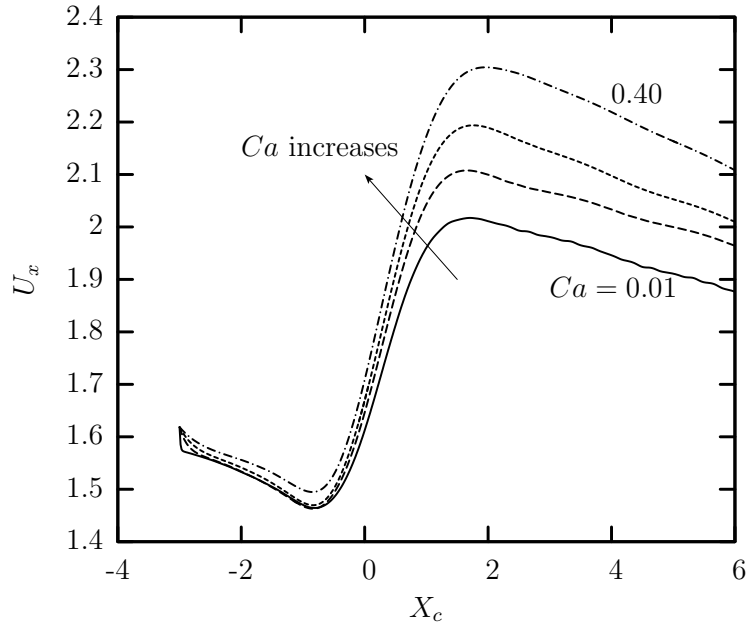


Figure 3.9: Droplet velocities as a function of the droplet centroid x_c for $\lambda = 0.2$, $a = 0.7$, $q = 0.5$ and capillary number $Ca = 0.01, 0.1, 0.2, 0.4$. (a) Droplet velocity along the flow direction U_x . (b) Droplet velocity along the z-axis U_z .

towards the centerline as it leaves the flow intersection. Lateral migration has been observed in the case of droplets and bubbles in wall bounded flows [47, 40, 29]. We observe from figure. 3.9(a) that the droplet velocity along the flow direction U_x , at all locations, increases with an increase in in the flow rate. The droplet velocity along the z -axis U_z remains almost independent of the flow rate, before the droplet centroid x_c is well inside the flow intersection. The final value reached by U_z at $x_c = 6.0$ also increases with an increase in Ca .

Figure 3.10(a) shows the plots of the minimum distance h of the droplet from the $z = -l_z$ wall of the junction, plotted as a function of the droplet centroid x_c as the droplet moves through the horizontal main channel of out T-junction device. At the start of our computations, after releasing the droplet in the main channel of the junction, we observe a slight increase in the minimum distance h . This initial increase in h is due to the lengthening of the droplet, with a bullet shape, which caused the droplet to become thinner due to volume preservation. This initial increase is followed by rapid decrease in h to a minimum, at a position with the droplet centroid x_c downstream of the junction. This decrease to the minimum occurs as the droplet enters the flow intersection and the droplet gets pushed towards the $-z$ wall of the junction by the flow coming through the vertical branch channel along the z -direction, causing h to decrease. This also causes Z_c to move towards the $z = -l_z$ wall of the junction, away from the centerline of the horizontal main channel, which explains its sharp decrease, as seen in figure 3.10(b). After the droplet passes the flow intersection, there is a lateral migration of the droplet towards the centerline of the junction with a decrease in deformation. The lateral migration of the droplet is slow as compared to the fast displacement away from the centerline of the main channel by the vertical flow through the branch channel. The final increase in h and Z_c , when the droplet centroid x_c is well downstream of the flow intersection.

3.4.2 Effect of droplet size

In this section, we collect the results of our computations studying the effect of droplet size on its dynamics in the microfluidic T-junction. The spherical droplets

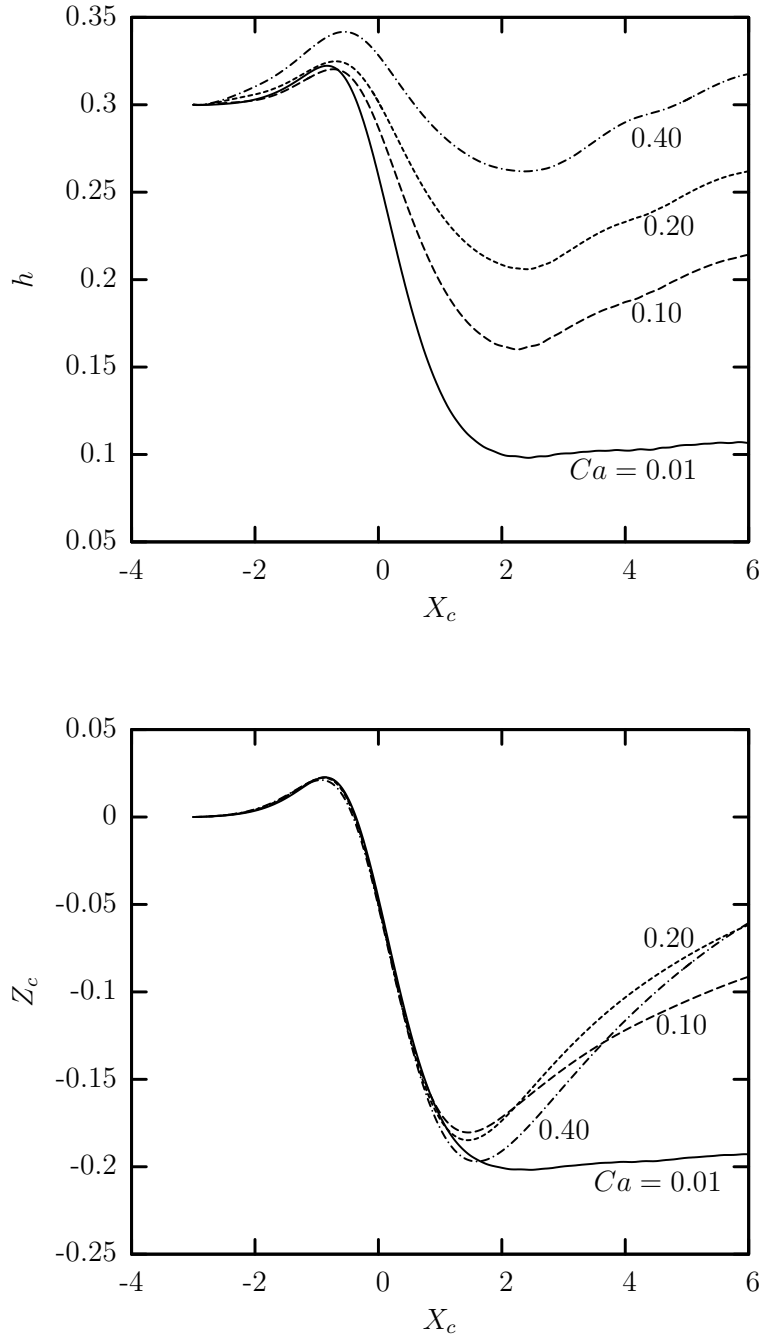


Figure 3.10: Minimum distance of the droplet interface, from the $z = -l_z$ wall of the junction, and droplet centroid position along the z -axis as a function of the droplet centroid x_c for $\lambda = 0.2$, $a = 0.7$, $q = 0.5$ and capillary number $Ca = 0.01, 0.1, 0.2, 0.4$. (a) Minimum distance h . (b) Droplet centroid position along the z -axis Z_c .

with viscosity ratio $\lambda = 0.2$ and capillary number $Ca = 0.1$ are placed upstream of the junction at $x_c = -3.0$, with the flow rate in the vertical branch channel maintained constant at $q = 0.5$. The range of droplet sizes studied in this chapter varies from moderately sized droplets with $a = 0.5$ to large droplets with $a = 0.9$. From our computations we found that the droplet deformation varies strongly as a function of droplet size a .

Figure 3.11(a) shows the droplet lengths L_x along the flow direction, which is the x -axis, plotted against the droplet centroid x_c . We scale the droplet lengths L_x with undisturbed values $2a$, thereby allowing us to compare the deformation of droplets of various sizes. As soon as we release a droplet, at its initial position with $x_c = -3.0$, the droplet moves through the horizontal main channel of the junction and its shape deforms, with an increase in its length and decrease in width. Initially the droplet takes the shape of a bullet, with a pointed downstream tip and a flattened rear. We observe from the plots that the droplet length L_x , till it enters the zone of flow intersection, depends on its size. For the moderately sized droplets ($a = 0.5, 0.6, 0.7$), L_x shows a small decrease, before the downstream droplet tip enters the flow intersection. For the large droplets ($a = 0.8, 0.9$), no such decrease in L_x is observed. In case of the larger droplets, the increase in their lengths is monotonic, as due to their large size the hydrodynamic forces acting on them is considerably large. The deformation of the droplets increase considerably after they enter the zone of flow intersection, as due to the flows coming in through the vertical branch channel the hydrodynamic forces acting on the droplets increase significantly. L_x reaches a maximum slightly downstream of the junction and then starts decreasing. For all droplet sizes studied, the lengths of the droplet L_x at the end of the junction is more than its undisturbed value at the start of computations. It is to be noted that the droplet deformation, hence its length L_x increases significantly with an increase in the droplet size. This is due to the fact that due to the large size of the droplets, the effective capillary number acting on the droplet becomes,

$$Ca^{\text{eff}} \sim \frac{\mu U}{\gamma} \left(\frac{L_z}{h}\right)^n \quad (3.14)$$

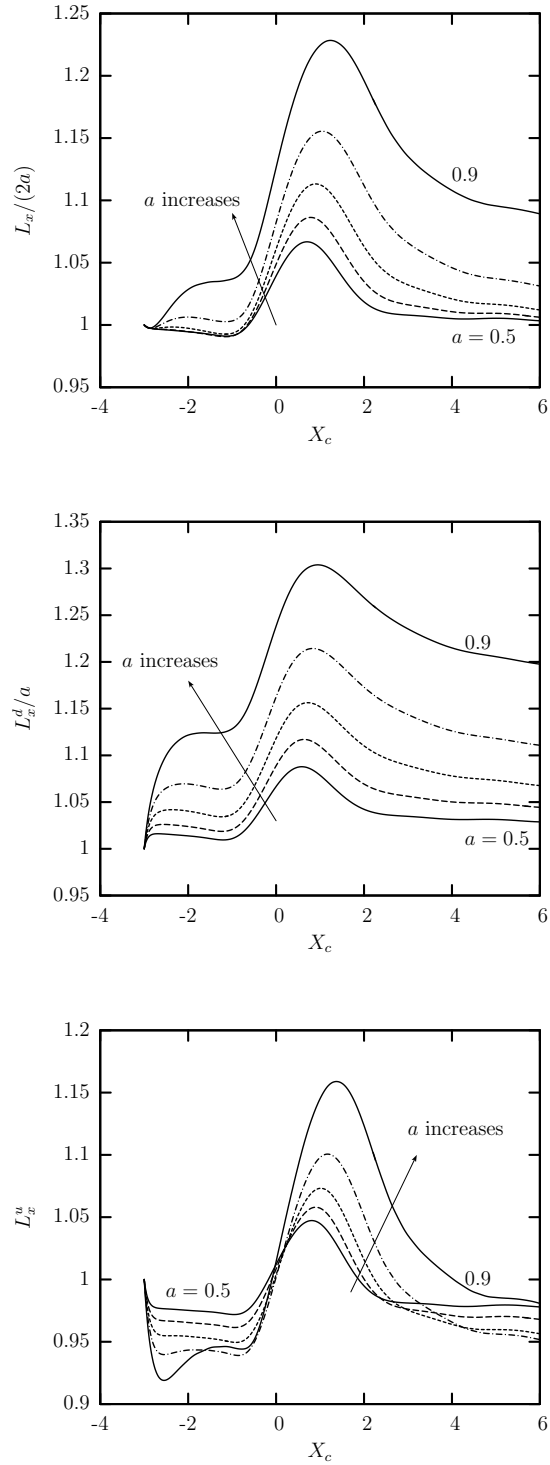


Figure 3.11: Droplet lengths along the flow direction as a function of the droplet centroid for $\lambda = 0.2$, $Ca = 0.1$, $q = 0.5$ and droplet size $a = 0.5, 0.6, 0.7, 0.8, 0.9$. (a) Droplet length $L_x/(2a)$. (b) Downstream droplet length L_x^d/a and (c) Upstream droplet length L_x^u/a .

where L_z is the length of the droplet along the z -axis. For the moderately sized droplets, the factor $(\frac{L_z}{h})^n$ is not significantly greater than 1, while for the larger sized droplets the factor is large as h , the distance of the droplet interface from the $z = -l_z$ wall of the junction decreases with an increase in droplet size, as can be seen in figure 3.12. In addition, due to the lack of a branch channel in the z -direction, the droplet interface gets pushed further towards the $z = -l_z$ wall of the junction. This results in a higher deformation of the larger sized droplets by becoming thinner and longer to preserve its volume while allowing the surrounding fluid to flow through the channel.

We divide the total droplet length L_x into the droplet's upstream length L_x^u and the downstream length L_x^d (calculated from the droplet centroid to the rear and front tips of the droplet) to explain the deformation of the front and rear parts of the droplet. We show the downstream and upstream lengths of the droplets in figure 3.11(b) and figure 3.11(c) respectively. The behavior of L_x^d is very similar to that of L_x , while L_x^u first go through at least one minimum before it starts increasing. The initial increase in L_x^d is due to the evolution of a pointed downstream tip and a flatter rear after the initiation of computation, which causes the droplet centroid to move towards the rear of the droplet. With an increase in the droplet size, the downstream length of the droplet L_x^d monotonically increases due to the lengthening of the downstream portion of the droplet, caused by an increase in Ca^{eff} . L_x^d increases rapidly after it enters the flow intersection, due to the additional flow coming in through the vertical branch channels, and reaches a maximum slightly downstream of the flow intersection. L_x^d starts decreasing rapidly after reaching the maximum, as the droplet gradually becomes less deformed. The final value attained by L_x at $x_c = 6$ increases with an increase in droplet size a , as there is less space for the surrounding fluid to flow through, causing the effective capillary number Ca^{eff} to rise.

From figure 3.11(c) we observe that before the droplet enters the flow intersection zone, L_x^u show a small decrease to a minimum, which is due to the flattening of the rear in the bullet shaped droplet, causing the droplet centroid to move towards

the rear of the droplet. However after the droplet enters the flow intersection, L_x^u increases rapidly as the droplet takes the bent bullet shape and then the slipper shape, causing the rear of the droplet to elongate and the droplet centroid to move towards the downstream tip of the droplet. L_x^u reaches a maximum slightly downstream of the flow intersection, similar to L_x^d . After reaching the maximum, L_x^u starts decreasing slowly when the rear of the slipper shaped droplet starts becoming less pointed. For all droplet sizes studied in this chapter, both L_x^d and L_x^u remain higher than 1 by the time the droplet centroid reaches $x_c = 6.0$. It is also observed from figure 3.11(b) and (c) that L_x^u is larger than L_x^d at $x_c = 6.0$, for all droplet sizes studied. This arises from the fact that in the slipper sized droplet, the pointed upstream portion of the droplet is longer, than the relatively less pointed front tip of the droplet.

In figure 3.12 (a) and (b) we plot L_y and L_z against the droplet centroid x_c . The final values of both L_y and L_z at $x_c = 6.0$ decrease with an increase in droplet size. However the initial behavior of L_y and L_z , before the droplet enters the flow intersection are different. For all droplet sizes studied, after the droplet is released in the horizontal main channel of the junction, L_y decreases monotonically until it reaches a minimum slightly downstream of the junction and then starts increasing again. On the other hand L_z shows different behavior for different droplet sizes studied. For the large droplet sizes studied ($a = 0.8, 0.9$), there is a small decrease in L_z followed by a increase before the droplet enters the flow intersection. For the smaller droplets with $a = 0.5, 0.6, 0.7$, L_z shows a small increase before the droplet enters the flow intersection. This different initial behavior is because of the fact that, in the case of the larger droplets, as soon they are released in the junction, the droplet deforms immediately to enable the surrounding fluid to flow through the channel. Also the front tip of the droplet, when it reaches the flow intersection zone, becomes elongated due to the flow coming through the vertical branch channel, causing the rear of the droplet to become flatter and wider and hence L_z shows the rapid small increase. When the droplet is completely within the flow intersection L_z decreases rapidly to a minimum and then starts increasing

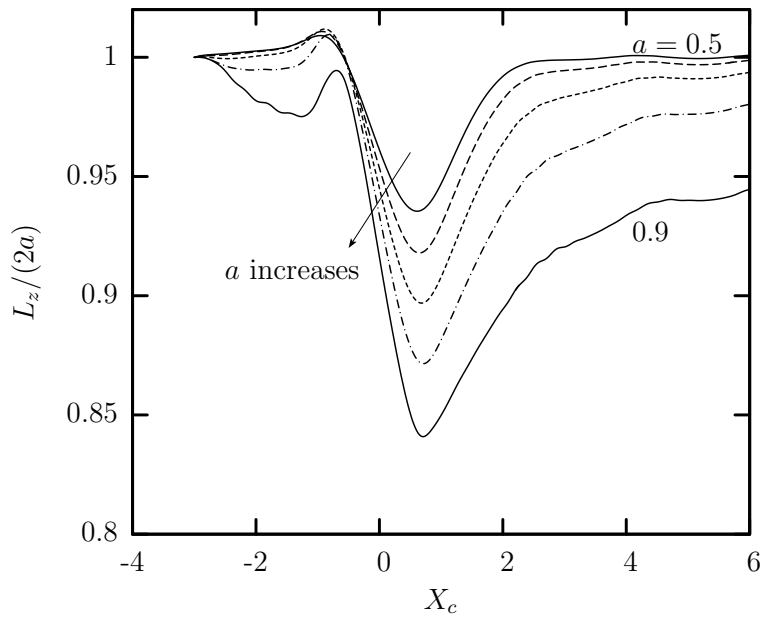
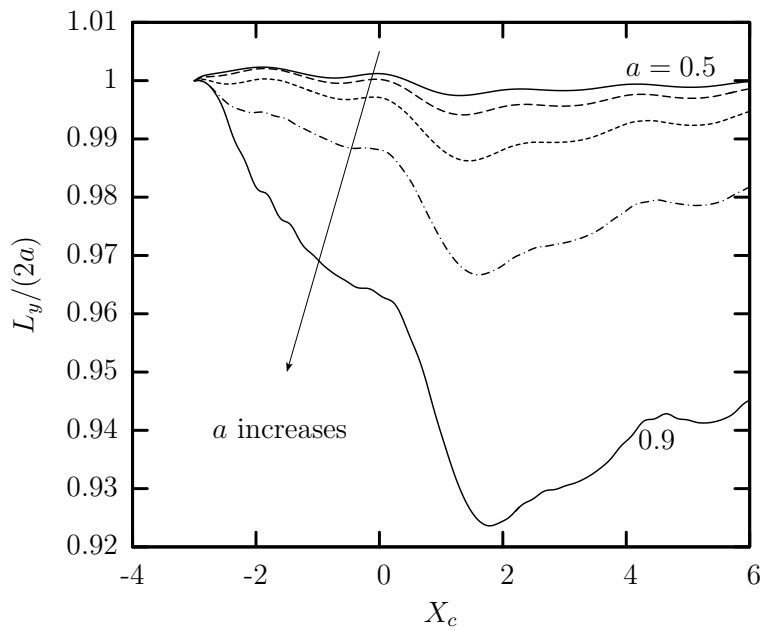


Figure 3.12: Droplet lengths along the y - and z -axes as a function of the droplet centroid x_c for $\lambda = 0.2$, $Ca = 0.1$, $q = 0.5$ and droplet size $a = 0.5, 0.6, 0.7, 0.8, 0.9$. (a) Droplet lengths along the y -axis $L_y/2a$. (b) Droplet lengths along the z -axis $L_z/2a$.

as the droplet moves downstream of the flow intersection. The rapid decrease is due to the droplet becoming becoming slender as it takes up the bent droplet and the slipper shape, while the increase afterwards is due to the droplet becoming less deformed in the downstream channel.

In figure 3.13 we show the plots of droplet surface area against the droplet centroid x_c . The surface area S_d is scaled with the surface area of the undisturbed spherical droplet S_d^0 . The droplet surface area is an important parameter as it gives us a general indication about the deformation of the droplet inside the T-junction. It is observed that S_d/S_d^0 starts increasing as soon as the droplet is released in the junction. For the moderate droplet sizes with $a = 0.5, 0.6, 0.7, 0.8$, S_d/S_d^0 increases monotonically until it reaches a maximum downstream of the flow intersection and then starts decreasing. The rapid increase in S_d/S_d^0 is due to the increased flow coming in through the vertical branch channels. For the large droplet with $a = 0.9$, there is a slight decrease in the droplet surface area before the front tip of the droplet enters the flow intersection which corresponds to the flattening of the front tip, before it enters the flow intersection, and a decrease in the droplet deformation. For all droplet sizes the droplet surface area S_d/S_d^0 increases with an increase in the droplet size a , due to an increase in the effective capillary number Ca^{eff} , at all x_c . In addition, we observe that for the moderately sized droplets ($a = 0.5, 0.6, 0.7$) the increase in S_d/S_d^0 at $x_c = 6.0$ is not significant as compared to the droplets with $a = 0.8, 0.9$.

The curvature of the xz -profile at the center of the downstream droplet tip, \mathcal{C}_{xz}^d is plotted in figure 3.14. The curvature \mathcal{C}_{xz}^d is scaled with the curvature of the undeformed spherical droplet $\mathcal{C}_{xz,0}^d$. The curvature \mathcal{C}_{xz}^d increases with an increase in the droplet size a . This is due to the formation of a pointed downstream droplet tip on deformation, which becomes more pointed with an increase in the droplet size a due to higher deformation caused by an increase in the effective capillary number Ca^{eff} . \mathcal{C}_{xz}^d starts increasing as soon as the droplet is released in the junction upstream of the flow intersection. For the moderately sized droplets with $a = 0.5, 0.6, 0.7, 0.8$, \mathcal{C}_{xz}^d shows a slight decrease, after the initial increase, before the

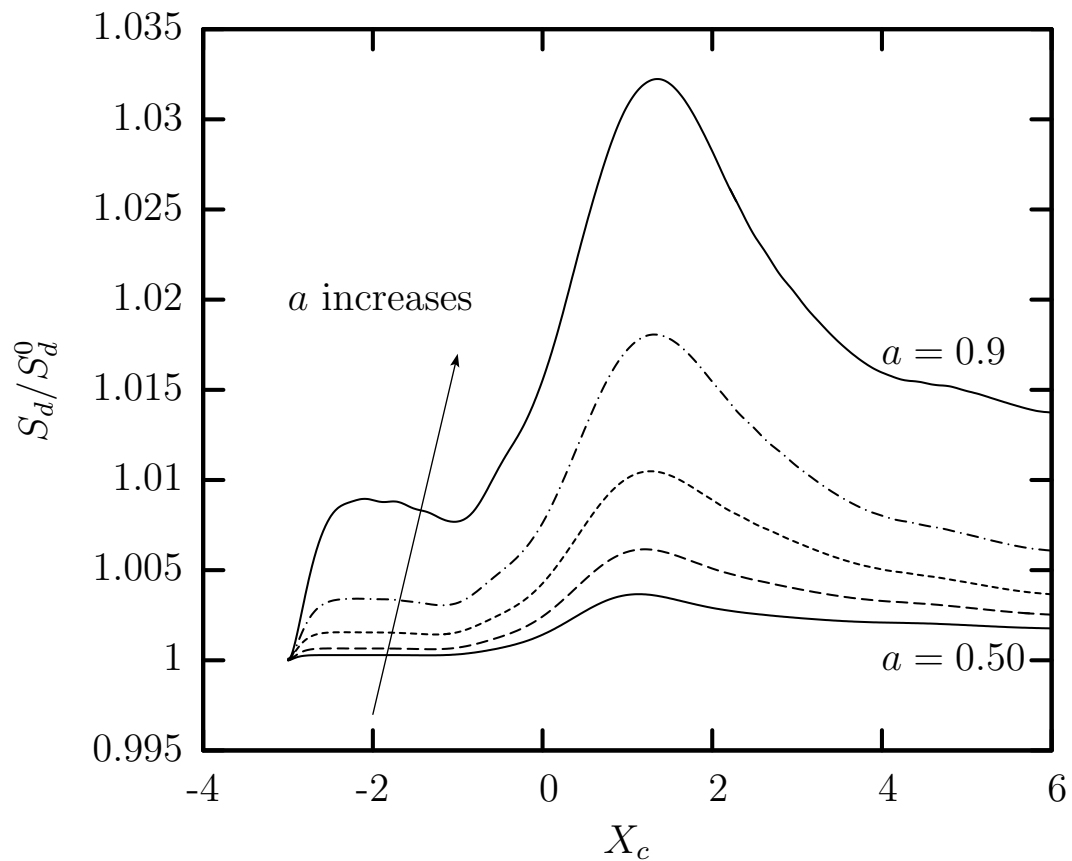


Figure 3.13: Surface area of the droplet (scaled with its undisturbed value) S_d/S_d^0 as a function of the droplet centroid x_c for $\lambda = 0.2$, $Ca = 0.1$, $q = 0.5$ and droplet size, $a = 0.5, 0.6, 0.7, 0.8, 0.9$.

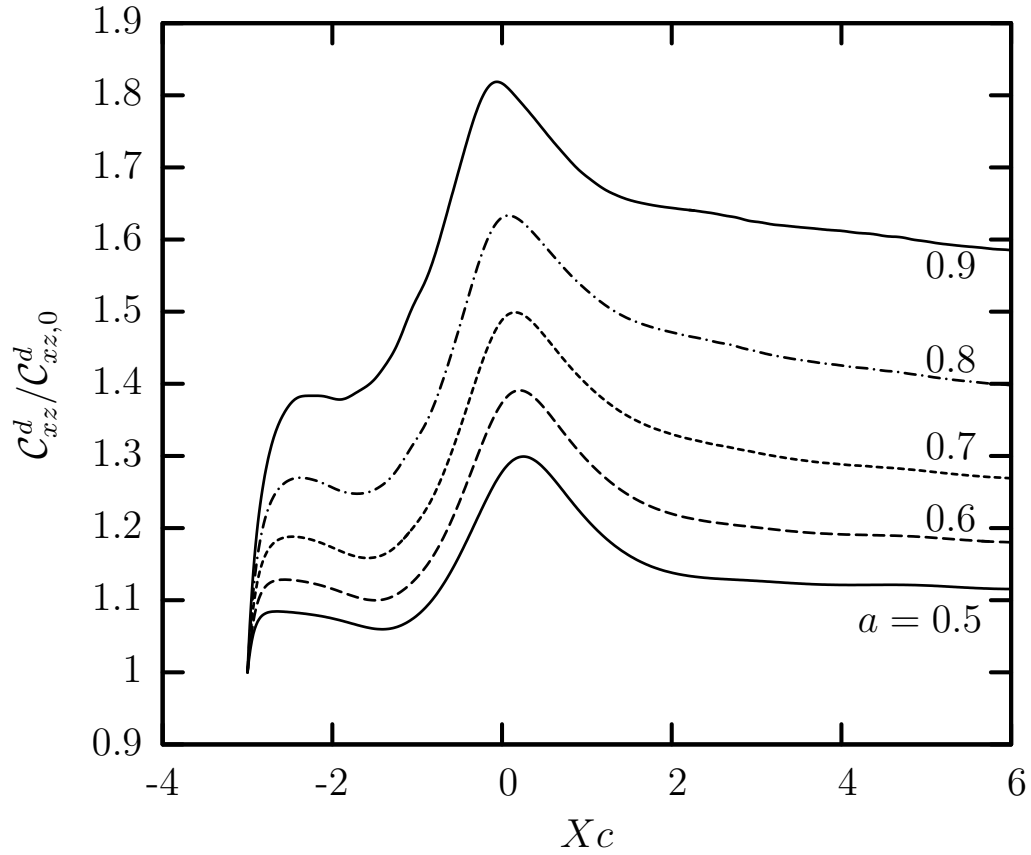


Figure 3.14: Curvature of xz -profile at the center of the downstream droplet tip (scaled with its undisturbed value) $C_{xz}^d / C_{xz,0}^d$ as a function of the droplet centroid x_c for $\lambda = 0.2$, $Ca = 0.1$, $q = 0.5$ and droplet size $a = 0.5, 0.6, 0.7, 0.8, 0.9$.

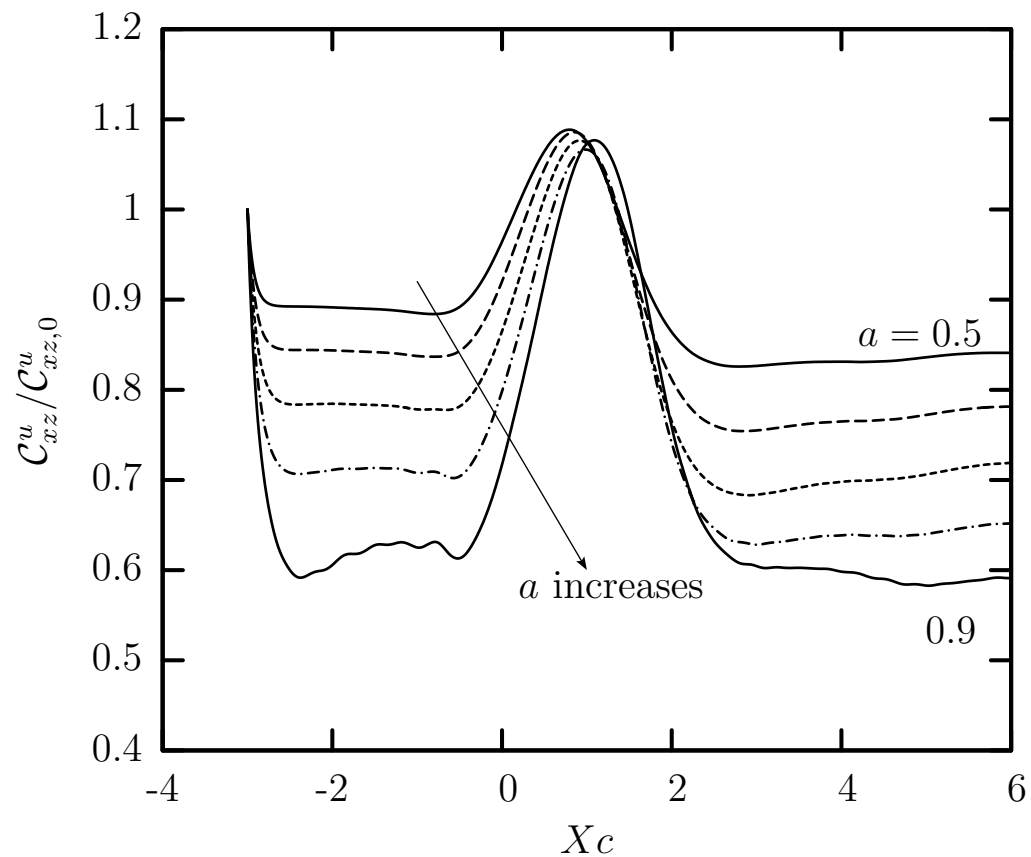


Figure 3.15: Curvature of the xz -profile at the center of the upstream droplet rear (scaled with its undisturbed value) $C_{xz}^u/C_{xz,0}^u$ as a function of droplet centroid x_c for $\lambda = 0.2$, $Ca = 0.1$, $q = 0.5$ and droplet size $a = 0.5, 0.6, 0.7, 0.8, 0.9$.

droplet enters the flow intersection, due to the front tip of the droplet becoming less pointed. \mathcal{C}_{xz}^d starts decreasing as the droplet leaves the flow intersection. The final value reached by \mathcal{C}_{xz}^d at $x_c = 6.0$ increases with an increase in the droplet size a .

Figure 3.15 shows the curvature of the xz -profile at the center of the droplet rear, \mathcal{C}_{xz}^u , as a function of the droplet centroid x_c . The curvature \mathcal{C}_{xz}^u is scaled with the curvature of the undeformed spherical droplet $\mathcal{C}_{xz,0}^u$. We observe, from the plots of figure 3.15, that the final value of the upstream tip curvature \mathcal{C}_{xz}^u , at $x_c = 6.0$, decreases with an increase in droplet size a . This is due to the higher deformation of the larger droplets, which again is due to higher Ca^{eff} . \mathcal{C}_{xz}^u initially shows a sharp decrease after the droplet is released in the junction, followed by an increase to a maximum and then a subsequent decrease after the droplet centroid passes the flow intersection. The initial decrease in \mathcal{C}_{xz}^u is due to the flattening of the rear of the bullet shaped droplet after it is released upstream of the flow intersection. The subsequent increase in \mathcal{C}_{xz}^u is due to the rear of the droplet becoming more pointed, as the droplet changes its shape from a bullet to a slipper. As in the slipper shaped droplet the rear starts becoming more pointed, which occurs at the edge of the droplet rear, the center of the droplet rear starts becoming flatter, causing \mathcal{C}_{xz}^u to drop.

We plot the droplet velocities, U_x and U_z , in figure 3.16(a) and (b) respectively. We observe from figure. 3.16(a) that the droplet velocity along the flow direction, U_x , decreases with an increase in the droplet size a , at all positions of the droplet centroid x_c . Upon release, the droplet velocity decreases to a minimum before the droplet enters the flow intersection zone and then increases sharply to a maximum downstream of the flow intersection, due to the additional flow through the vertical branch channel. This is followed by a slow decrease to a value which is higher than the initial velocity of the droplet.

The droplet velocity along the z -axis, U_z , remains almost independent of the droplet size, before the droplet centroid enters the flow intersection, as seen from figure 3.16(b). As the droplet enters the flow intersection, the magnitude of U_z increases rapidly as the droplet gets pushed towards the $z = -l_z$ wall of the junc-

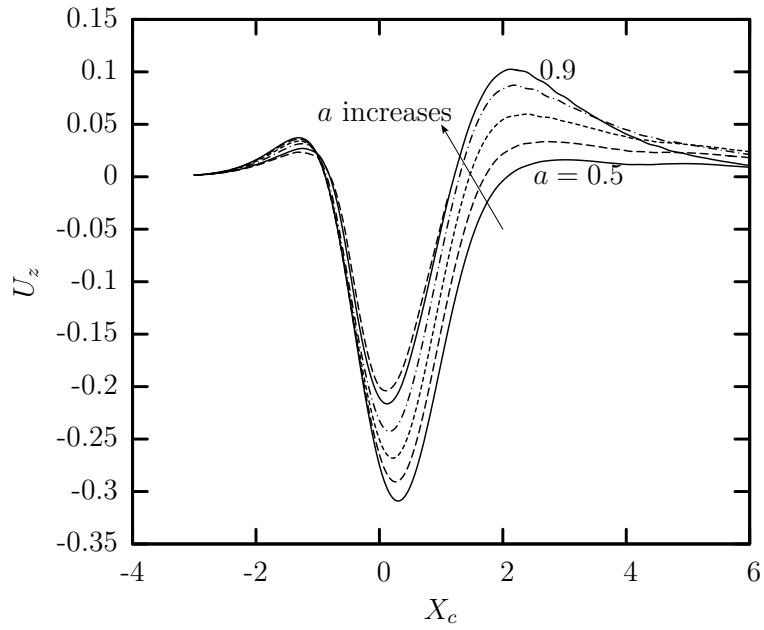
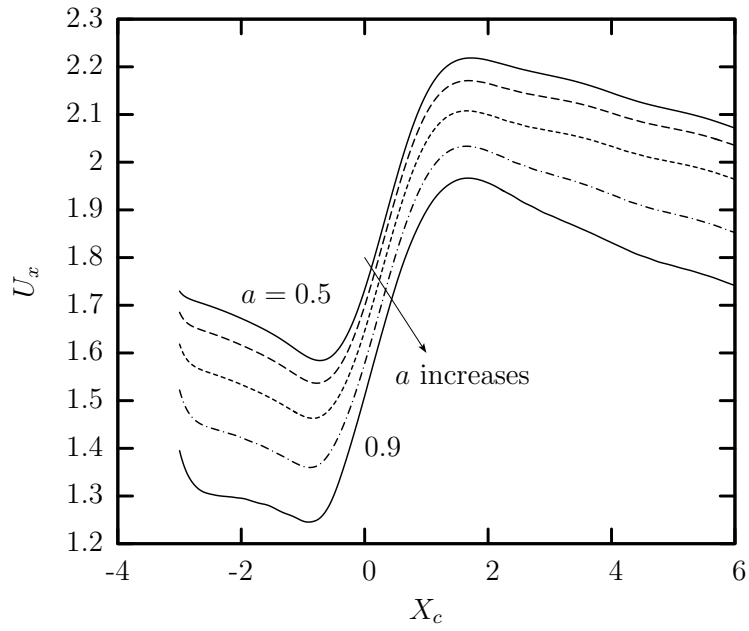


Figure 3.16: Droplet velocities as a function of droplet centroid x_c for $\lambda = 0.2$, $Ca = 0.1$, $q = 0.5$ and droplet size $a = 0.5, 0.6, 0.7, 0.8, 0.9$. (a) Droplet velocity along the flow direction U_x . (b) Droplet velocity along the z -axis U_z .

tion. We observe that the droplets with larger size gets pushed slower towards the $z = -l_z$ wall of the junction by the additional incoming flow through the vertical branch channel. U_z decreases to a maximum as the droplet leaves the flow intersection. As the droplets become less deformed downstream of the flow intersection and starts experiencing a lateral migration towards the centerline of the horizontal main channel, the magnitude of U_z starts decreasing. However U_z does not reach any steady state by the time the droplet centroid reaches $x_c = 6.0$, as the lateral migration continues.

We plot the the minimum distance h of the droplet from the $z = -l_z$ wall of the junction, as a function of the droplet centroid x_c in figure 3.17(a). At the start of our computations, after releasing the droplet in the main channel of the junction, we observe a slight increase in the minimum distance h . This initial increase in h is due to the initial lengthening of the droplet as it takes a bullet shape, which causes the droplet to become thinner due to volume preservation. This initial increase is followed by a rapid decrease to a minimum. This decrease to the minimum occurs as the droplet enters the flow intersection and the droplet gets pushed towards the $-z$ wall of the junction by the flow coming through the vertical branch channel along the z -direction, causing h to decrease. The final increase in h , when the droplet centroid x_c is well downstream of the flow intersection, happens as the droplet becomes less deformed after crossing the flow intersection and slowly moves away from the junction wall.

In figure 3.17(b) we plot the droplet centroid along z -axis Z_c as a function of the droplet centroid position along the flow direction x_c . From the plots we observe that, for all droplet sizes studies, Z_c shows a sharp decrease when the droplet enters the flow intersection, as a result of the droplet getting pushed towards the $z = -l_z$ wall of the T-junction device, which causes Z_c to move towards it. The slow increase in Z_c , after the droplet passes the flow intersection is a result of the lateral migration of the droplet away from the $z = -l_z$ wall of the T-junction. We observe that the droplets with larger size experiences a much smaller displacement in the z -direction, as compared to a droplet with smaller size. In addition, we observe that

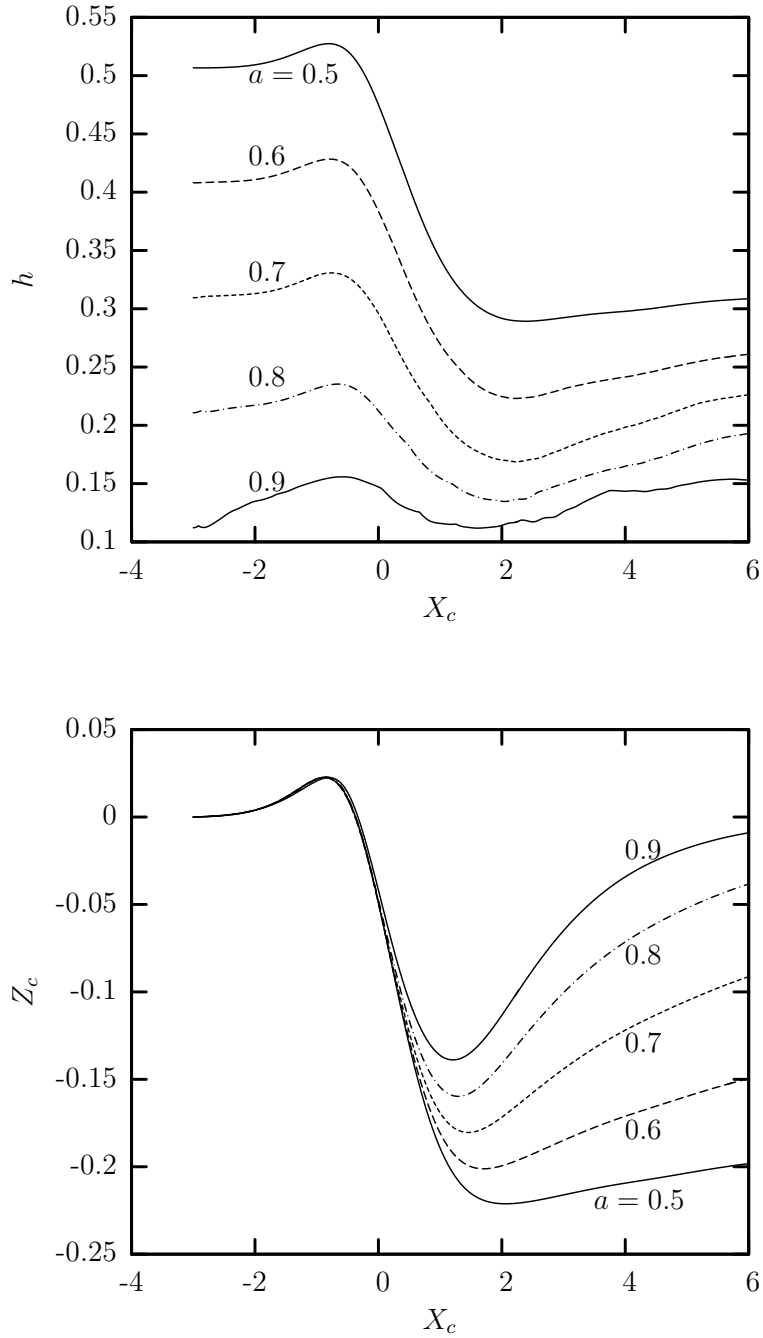


Figure 3.17: Minimum distance of the droplet interface, from the $z = -l_z$ wall of the junction, and droplet centroid along z -axis as a function of the droplet centroid for $\lambda = 0.2$, $Ca = 0.1$, $q = 0.5$ and droplet size $a = 0.5, 0.6, 0.7, 0.8, 0.9$. (a) Minimum distance h . (b) Droplet centroid along z -axis Z_c .

the difference in displacement of different sized droplets becomes pronounced only after the droplet enters the flow intersection.

3.4.3 Effect of viscosity ratio

In this section, we collect the results and study the effects of viscosity ratio on the dynamics of the droplets in the T-junction. The range of viscosity ratio studied here range from very low ($\lambda = 0.01$) to very high ($\lambda = 20$) while keeping the other parameters like capillary number $Ca = 0.1$, droplet size $a = 0.7$, flow rate in branch channel $q = 0.5$ constant. It was observed from our computations that the droplet dynamics varies strongly as a function of the viscosity ratio of the fluids.

Figure 3.18(a) shows the droplet lengths L_x along the flow direction as a function of the droplet centroid x_c for different viscosity ratios. We also divide the total droplet length L_x into the droplet's upstream and downstream length, L_x^u and L_x^d , (calculated from the droplet centroid x_c to the rear and the front tips of the droplet) and plot them separately in figure 3.18(b, c) as a function of the droplet centroid x_c . We observe from the plots of figure 3.18(a) that the total length of the droplet L_x shows behavior dependent upon the viscosity ratio λ . For all viscosity ratios λ studied, the droplet length decreases to a minimum before the droplet enters the flow intersection. After the minimum is reached, there is a rapid increase in L_x to a maximum, as the droplet enters the flow intersection, and then a sharp decrease as the droplet leaves the flow intersection. The initial decrease in droplet length L_x , upstream of the flow intersection, is due to a shortening of the droplet, with a pointed tip and flattened rear, after being released in the horizontal main channel of the junction. The increase to the maximum, downstream of the flow intersection, is because of higher deformation by the additional flow coming in through the vertical branch channel. We observe that for $\lambda = [0.01, 1]$, the maximum value of L_x reached downstream of the junction increases with an increase with an increase in λ , while for $\lambda = 10, 20$ the opposite happens. In the case of deformation of a single droplet in a rectangular straight channel, it has been observed that the deformation of a droplet, and hence L_x , increases with an increase in λ due to an increase in higher

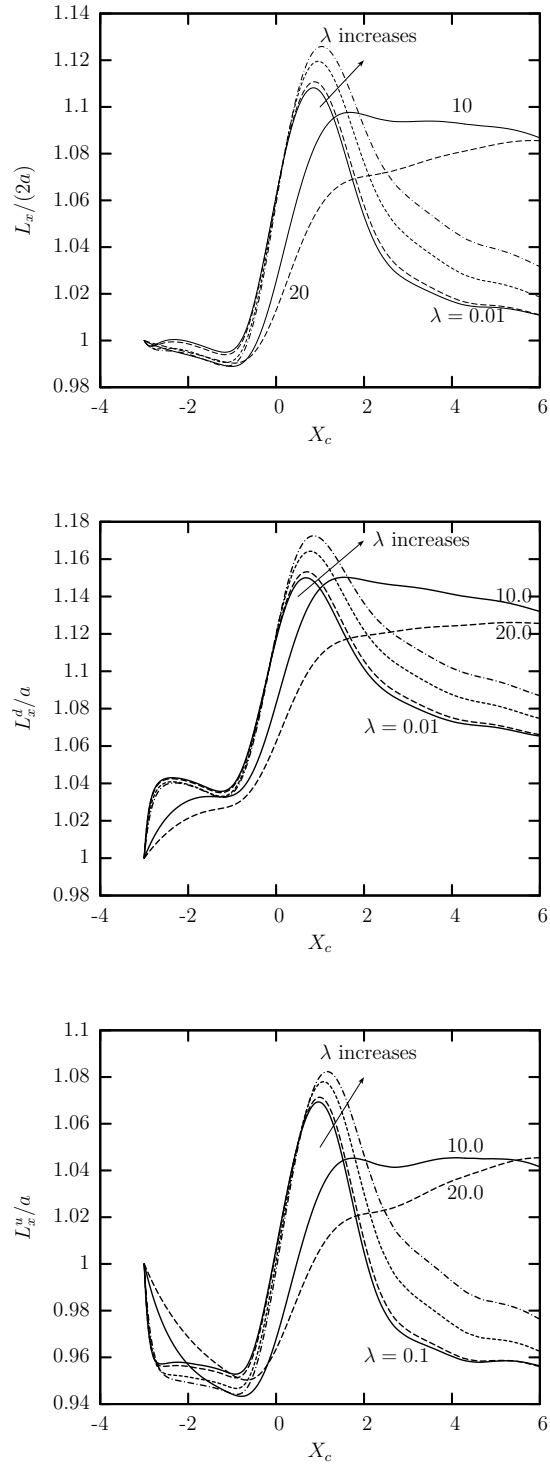


Figure 3.18: Droplet lengths along the flow direction as a function of the droplet centroid x_c for $Ca = 0.1$, $a = 0.7$, $q = 0.5$ and viscosity ratio $\lambda = 0.01, 0.1, 0.5, 1, 10, 20$. (a) Droplet length $L_x/(2a)$. (b) Downstream droplet length L_x^d/a . (c) Upstream droplet length L_x^u/a .

inner hydrodynamic forces [48]. However deformation takes place faster for a droplet with a smaller λ , *i.e.*, a less viscous droplet needs less time deforming from its initial shape. The time needed for a droplet to deform can be expressed as,

$$\tau \sim (1 + \lambda)Ca\tau_f \quad (3.15)$$

When λ is small there is enough time for the droplet to deform and hence the maximum L_x increases with an increase in λ . When $\lambda = 10, 20$, the time needed by the droplet to deform to its maximum is significantly raised as the factor $(1+\lambda)$ becomes dominant and hence we observe the decrease in the maximum L_x with an increase in λ . In our study, the droplets do not reach steady state by the time $x_c = 6$, but if given enough time the final value of L_x will increase with an increase in λ .

The downstream and upstream lengths of the droplet L_x^d, L_x^u , show behavior different from each other, as can be seen from figure 3.18(b, c). We observe that, after the droplet is released in the horizontal main channel of the junction, In general, L_x^d shows a small increase, while L_x^u shows a small decrease before the droplet enters the flow intersection. This behavior of L_x^d and L_x^u is due to the formation of a pointed tip and a flattened rear, followed by a flattening of the pointed downstream tip when the front tip is about to enter the flow intersection. Both L_x^d and L_x^u increase rapidly when the droplet enters the flow intersection, and reach a maximum at a location where the droplet centroid is downstream of the flow intersection. The maximum values attained by L_x^d and L_x^u depends upon the viscosity ratio λ , hence the time needed for deformation. Similar to L_x , for $\lambda = [0.01, 1]$, the maximum values of L_x^d and L_x^u increase with an increase with an increase in λ , while for $\lambda = 10, 20$ the opposite happens, as there is not enough time for the droplet to deform. In addition, we observe that the downstream droplet length L_x^d is greater than the upstream droplet length L_x^u for all viscosity ratios studied.

The plots for the droplet lengths along the y - and z -axes, L_y and L_z , are shown in figure 3.19(a) and (b) respectively as a function of the droplet centroid x_c . In general, as compared to L_x , both L_y and L_z show complex behavior during

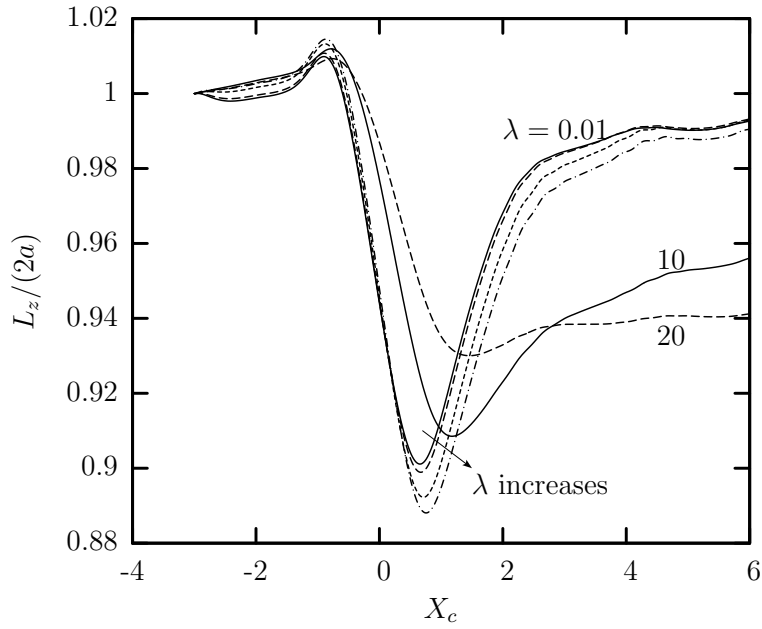
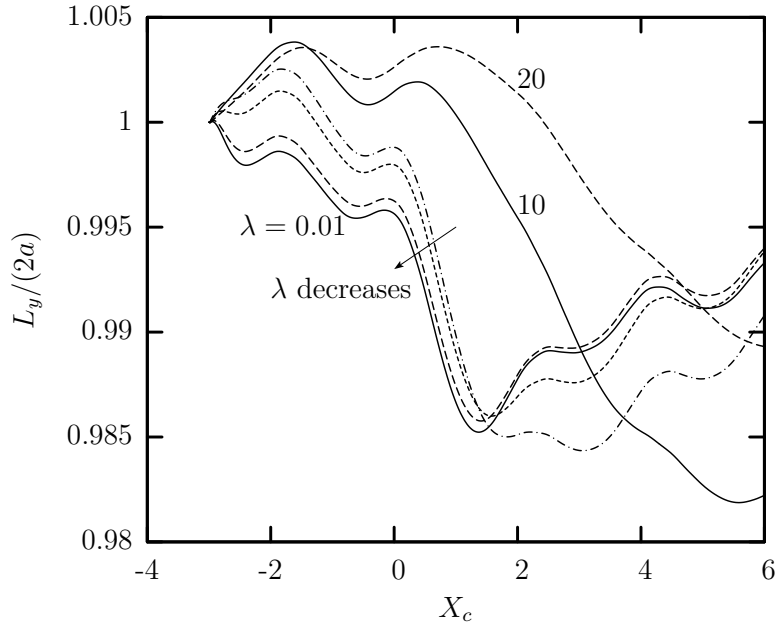


Figure 3.19: Droplet lengths along the y - and z -axes as a function of the droplet centroid x_c for $Ca = 0.1$, $a = 0.7$, $q = 0.5$ and viscosity ratio $\lambda = 0.01, 0.1, 0.5, 1.0, 10.0, 20.0$. (a) Droplet length along the y -axis $L_y/(2a)$. (b) Droplet length along the z -axis $L_z/(2a)$.

the deformation of the droplet. L_y and L_z both decrease rapidly after the droplet enters the flow intersection and reach a minimum. For $\lambda = [0.01, 10]$ L_y reaches a minimum downstream of the flow intersection and then starts increasing. For $\lambda = 20$, L_y does not reach the minimum by the time the droplet centroid reaches $x_c = 6.0$, as there is not enough time for the droplet to deform. Similar to L_y , L_z also reaches a minimum after the droplet centroid crosses the center of the junction and starts increasing as the droplet gradually tries to regain its original shape. The minimum value reached by L_z for $\lambda = [0.01, 1.0]$ decreases with an increase in the viscosity ratio, while for $\lambda = [10, 20]$ it increases with the increase in viscosity ratio. This behavior again can be explained by considering the time needed by a droplet to deform, as explained before.

Figure 3.20 shows the plots of the surface area of the deformed droplet S_d plotted against the droplet centroid x_c for different viscosity ratios. The surface area of the deformed droplet S_d is scaled with its undisturbed value S_d^0 . From the plots we observe that S_d/S_d^0 reaches a maximum downstream of the flow intersection and then starts decreasing. The maximum value of S_d reached by the droplet increases with an increase in the viscosity ratio λ for $\lambda = [0.01, 1.0]$, while for $\lambda = [10, 20]$ the opposite happens. This again can be explained by considering the time τ needed by the droplet to deform from its undisturbed shape, which increases with an increase in viscosity ratio. For the range of viscosity ratio studied, S_d does not reach a steady state at $x_c = 6$.

The curvature of the xz -profile of the center of the downstream droplet tip, \mathcal{C}_{xz}^d , is plotted in figure 3.21. The curvature \mathcal{C}_{xz}^d is scaled with the curvature of the undeformed droplet $\mathcal{C}_{xz,0}^d$. From the plots of figure 3.21, we observe that \mathcal{C}_{xz}^d shows a sharp increase to a maximum when the droplet enters the flow intersection and then starts decreasing. Again, the maximum and the final values of \mathcal{C}_{xz}^d is dependent upon the viscosity ratio λ of the fluids and increase with an increase in λ for $\lambda = [0.01, 1]$, while they decrease for $\lambda = [10, 20]$. This can be explained considering the time τ needed by a droplet to deform to its steady state shape. For small to moderate viscosity ratio of $\lambda = [0.01, 1]$, there is enough time for the droplet to deform and

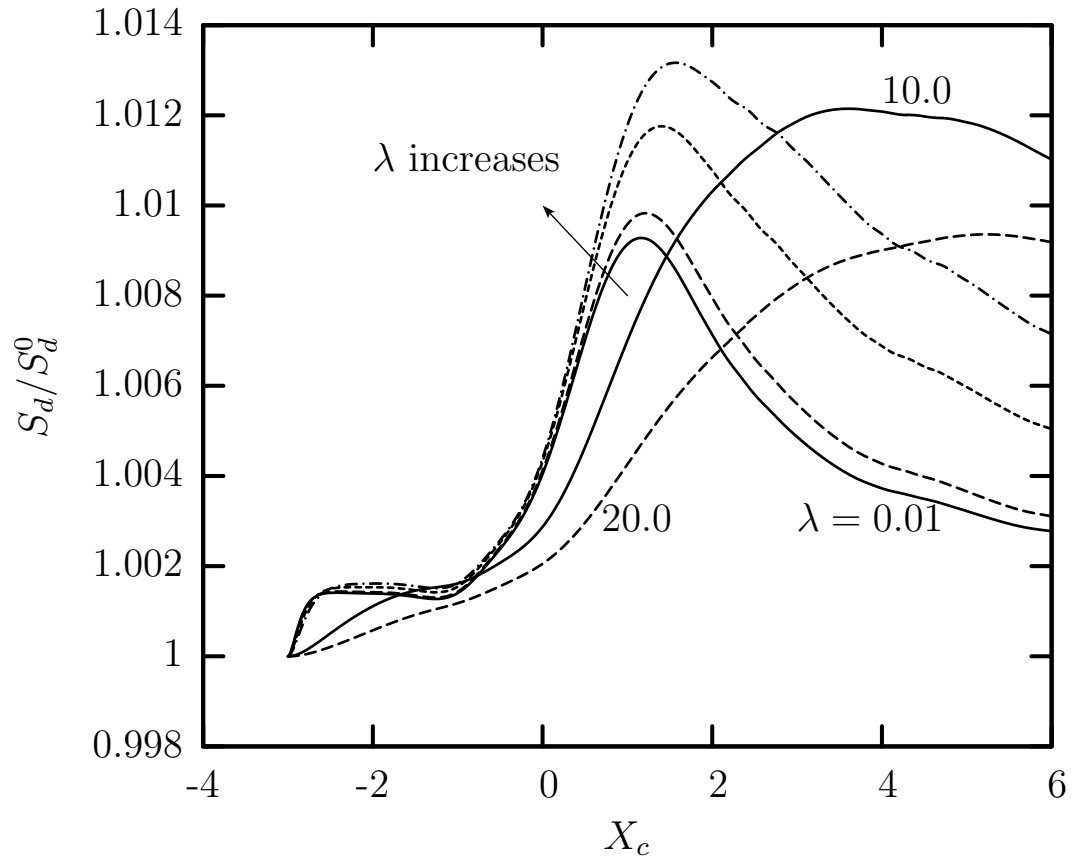


Figure 3.20: Surface area of the droplet (scaled with its undisturbed value) S_d/S_d^0 as a function of the droplet centroid x_c for $Ca = 0.1$, $a = 0.7$, $q = 0.5$ and viscosity ratio $\lambda = 0.01, 0.1, 0.5, 1.0, 10.0, 20.0$.

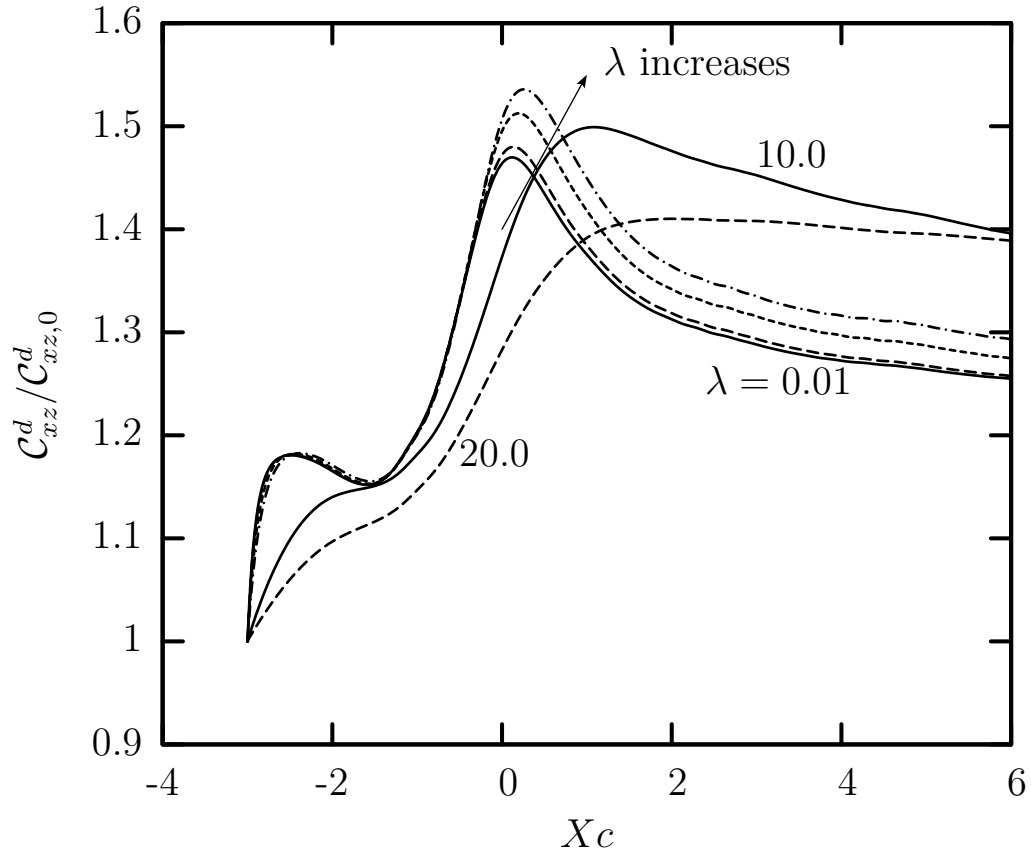


Figure 3.21: Curvature of the xz -profile of the center of the downstream droplet tip (scaled with its undisturbed value) $C_{xz}^d/C_{xz,0}^d$ as a function of the droplet centroid x_c for $Ca = 0.1$, $a = 0.7$, $q = 0.5$ and viscosity ratio $\lambda = 0.01, 0.1, 0.5, 1, 10, 20$.

hence the maximum increases with an increase in λ , while for the very large viscosity ratios of $\lambda = [10, 20]$ the factor $(1+\lambda)$ becomes more dominant and hence a droplet with $\lambda = [10, 20]$ needs more time to deform.

Figure 3.22 shows the plots for curvature \mathcal{C}_{xz}^u of the center of the upstream droplet rear. The curvature \mathcal{C}_{xz}^u is scaled with the curvature of the undisturbed droplet $\mathcal{C}_{xz,0}^u$. From figure 3.22, we observe that for all λ , \mathcal{C}_{xz}^u decreases after the start of computations, due to the formation of a bullet shape. This is followed by a sharp increase to a maximum as the droplet shape gradually changes from that of a bullet to a slipper. For $\lambda = [0.01, 1]$, the maximum value of \mathcal{C}_{xz}^u increases with an increase in the viscosity ratio λ , while for $\lambda = [10, 20]$ the maximum value of \mathcal{C}_{xz}^u decreases with an increase in λ . The final value of \mathcal{C}_{xz}^u , at $x_c = 6.0$, decreases with an increase in viscosity ratio for $\lambda = [0.01, 1]$, while for $\lambda = [10, 20]$ it decreases with an increase in λ . Downstream of the flow intersection, the rear of the slipper shaped droplet maintains its pointed shape at the edge of the rear element. For the low viscosity droplets with $\lambda = [0.01, 1]$, as there is enough time for the droplet to deform, and hence for the center of the rear to become much flatter, final value of \mathcal{C}_{xz}^u decreases with an increase rate. Due to a lack of enough time to deform and have a flattened center at droplet rear, the final value of \mathcal{C}_{xz}^u increases with an increase in viscosity ratio for $\lambda = [10, 20]$.

Figure 3.23(a) shows plots of droplet velocity along the flow direction, U_x , as a function of the droplet centroid x_c for the viscosity ratios studied. We observe that the droplet velocity U_x decreases with an increase in the viscosity ratio λ , at all values of x_c . After the droplet is released, U_x decreases until the droplet enters the flow intersection followed by a rapid increase to a maximum and then a subsequent decrease after the droplet exits the flow intersection. The rapid increase after the droplet enters the flow intersection is due to the flow coming in through the vertical branch channel. The influence of viscosity ratio λ on droplet velocity U_x is qualitatively similar to that reported by Wang and Dimitrakopoulos in their study of droplets in rectangular straight channels [48]. In addition, we plot the droplet velocity along the z -axis U_z as a function of the droplet centroid x_c in figure 3.23(b).

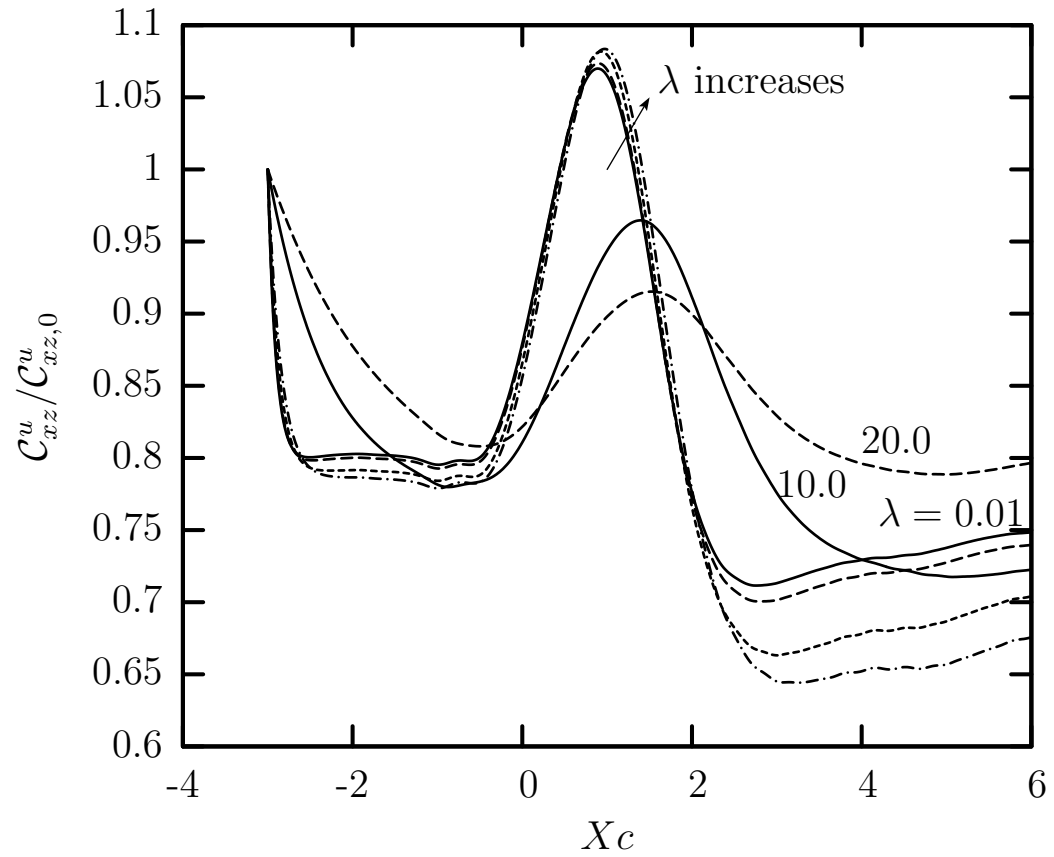


Figure 3.22: Curvature of the xz -profile of the center of the upstream droplet rear (scaled with its undisturbed value) $C_{xz}^u/C_{xz,0}^u$ as a function of the droplet centroid x_c for $Ca = 0.1$, $a = 0.7$, $q = 0.5$ and viscosity ratio $\lambda = 0.01, 0.1, 0.5, 1.0, 10.0, 20.0$.

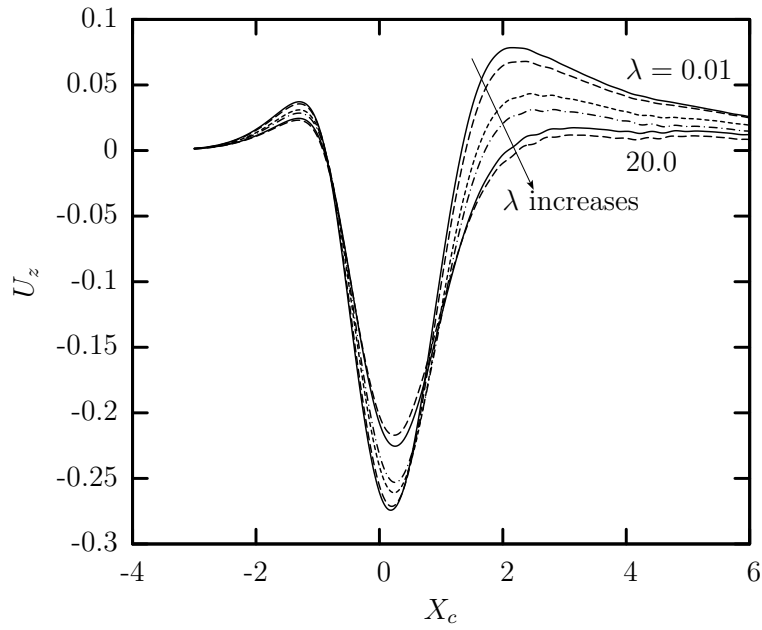
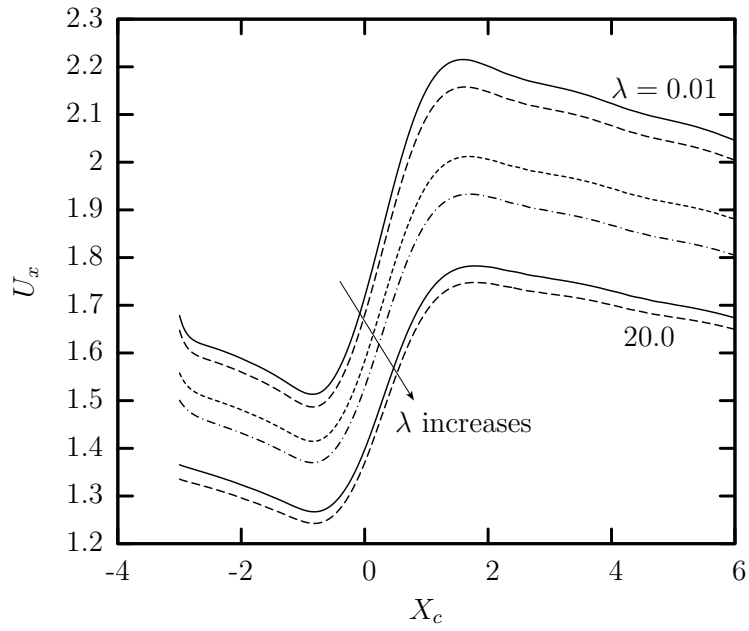


Figure 3.23: Droplet velocities as a function of the droplet centroid x_c for $Ca = 0.1$, $a = 0.7$, $q = 0.5$ and viscosity ratio $\lambda = 0.01, 0.1, 0.5, 1.0, 10.0, 20.0$. (a) Droplet velocity along the flow direction U_x . (b) Droplet velocity along the z -axis U_z .

As the droplet gets pushed towards the $z = -l_z$ wall of the junction by the additional flow through the vertical branch channel in the flow intersection, we observe that the magnitude of maximum velocity reached by droplet in the z -direction decreases with an increase in the viscosity ratio. As the droplet begins its lateral migration towards the centerline of the main channel, the velocity of lateral migration increases with a decrease in viscosity ratio. In case of U_z as well the the final value reached at $x_c = 6.0$ decreases with an increase in the viscosity ratio λ .

Figure 3.24(a) shows the plots of the minimum distance h of the droplet interface from the $z = -l_z$ wall of the T-junction, as a function of the droplet centroid x_c . We observe that the minimum distance increases to a maximum before the droplet enters the flow intersection, which is followed by a decrease to a minimum. This initial increase in h is due to the lengthening of the droplet on flow initiation. The decrease to the minimum occurs as the droplet enters the flow intersection and the droplet gets pushed towards the $-z$ wall of the junction by the flow coming through the vertical branch channel. After reaching the minimum, the minimum distance h starts increasing slowly as the droplet gradually becomes less deformed downstream of the flow intersection. The droplet centroid position along the z -axis, Z_c , also increases to a maximum before the droplet enters the flow intersection, as seen in figure 3.24(b). After the droplet enters the flow intersection, Z_c decreases rapidly to a minimum as the droplet gets pushed towards the $z = -l_z$ wall of the T-junction. This is followed by a slow increase in Z_c as the droplet gradually starts regaining its shape and starts its lateral migration towards the centerline of the horizontal main channel.

3.5 Conclusion

In this chapter, we have investigated computationally the dynamics of microfluidic droplets in a T-junction device comprising of square channels. In particular, we have considered droplets with constant surface tension which are naturally buoyant in the surrounding fluid, and have size smaller than the cross-section of the square

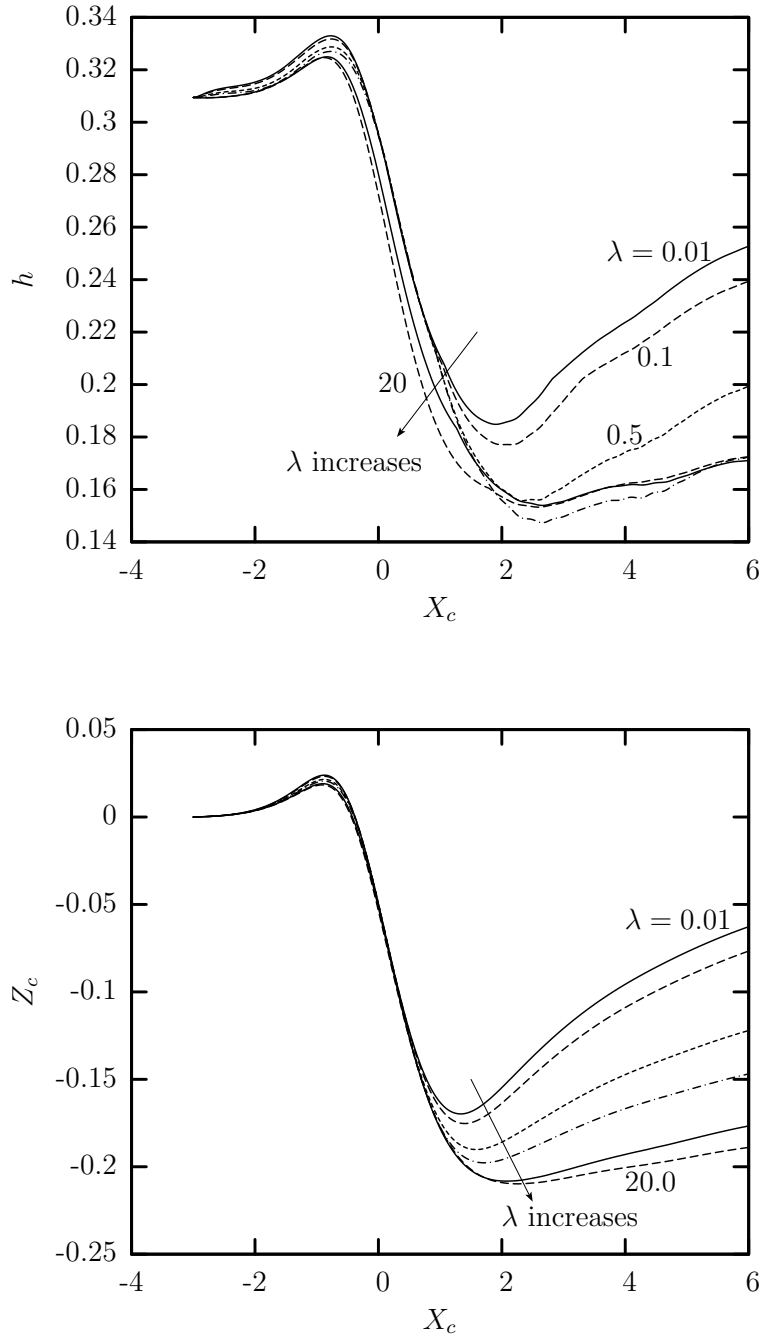


Figure 3.24: Minimum distance h of the droplet interface, from the $z = -l_z$ wall of the junction, and droplet centroid along z -axis as a function of the droplet centroid for $Ca = 0.1$, $a = 0.7$, $q = 0.5$ and viscosity ratio $\lambda = 0.01, 0.1, 0.5, 1.0, 10.0, 20.0$. (a) Minimum distance h . (b) Droplet centroid along z -axis Z_c .

channels comprising the cross-junction. The study is motivated by a wide range of applications including direct contact heat-mass exchangers, encapsulation of reactants with droplets as microreactors, drug delivery methods, coating processes, and of course applications in energy, e.g. enhanced oil recovery processes and direct methanol fuel cells.

To our knowledge, this is the first work to systematically study the dynamics of droplets, without interfacial breaking, in a microfluidic T-junction device. Our investigation complement earlier studies on formation of droplets in a microfluidic T-junction and droplet motion in a straight rectangular microfluidic channel [17, 44, 48]. We summarize briefly some of the more important conclusions.

(i) Our computations investigating the effects of flow rates in the channels of the T-junction, has revealed that the degree of interfacial deformation of the droplet, and hence its dynamics, depends strongly on the strengths of flows in the channels of the T-junction device. In general, upon release, the droplet takes the shape of a bullet after flow initiation with a pointed downstream tip and a flattened rear, so that to increase the restoring surface tension forces and thus balance the deforming hydrodynamic forces. As the droplet enters the flow intersection, the tip of the bullet shaped droplet becomes skewed to accommodate the additional flow through the vertical branch channel. The droplet takes the shape of a bent bullet when it is well into the flow intersection. As the droplet moves further downstream, the droplet centroid moves towards the tip of the droplet, as the droplet becomes slipper shaped with a very pointed rear, while the downstream tip becomes relatively flattened. As the droplet completely exits the flow intersection, the rear of the slipper shaped droplet becomes less pointed as it gradually tries to regain its shape and finally exits the T-junction device.

During this diverse interfacial evolution, the droplet lengths, tip curvatures and its velocity change extensively, depending upon the droplet shape and location in the T-junction device. We have monitored these parameters during the interfacial evolution of the droplet and have provided qualitative explanations.

(ii) Studying the effects of the droplet sizes on its dynamics, we observed that

the minimum distance of the droplet interface from the junction wall plays a significant role in its interfacial evolution. The deformation of droplets with bigger size increases significantly, as the effective capillary number Ca^{eff} acting on the droplet increases. Before the flow intersection, the droplet develops a pointed downstream tip and a flattened rear. When the droplet rear of the droplet enters and flows through the flow intersection of the T-junction device, it gradually becomes more pointed and skewed towards the $z = -l_z$ wall of the junction due to flow through the vertical branch channel. The very pointed slipper shaped droplet is observed only for when the droplet size is large.

(iii) We found the viscosity ratio of the fluids to strongly effect the dynamics of droplets in our T-junction device. For low viscosity droplets, with λ up to $O(1)$, we found the droplet deformation to increase monotonically with an increase in viscosity ratio, owing to higher inner hydrodynamic forces. However, for high-viscosity droplets with $\lambda = O(10)$, the droplet deformation decreases significantly inside the T-junction because the droplet does not have the time to accommodate the much slower deformation rate at high λ as it moves fast inside the microfluidic device. We note that, for high-viscosity droplets, the droplet deformation will eventually increase as the viscosity ratio is increased in the straight channel far downstream the T-junction owing to higher inner hydrodynamic forces.

In addition, our study demonstrates the ability of our computational method to determine the droplet dynamics in intersecting flows accurately. With further modification in geometry, even more complicated droplet dynamics may be accurately predicted.

Bibliography

- [1] S. Afkhami, A. M. Leshansky and Y. Renardy, Numerical investigation of elongated drops in a microfluidic T-junction. *Phys. Fluids* **23**, 022002 (2011).
- [2] C. N. Baroud, F. Gallaireb and R. Dangla, Dynamics of microfluidic droplets. *Lab. Chip.* **10**, 2032–2045 (2010).
- [3] D. Barthès-Biesel and A. Acrivos, Deformation and burst of a liquid droplet freely suspended in a linear shear field. *J. Fluid Mech.* **61**(1), 1–21 (1973).
- [4] J. A. Champion, Y. K. Katare and S. Mitragotri, Particle shape: a new design parameter for micro- and nanoscale drug delivery carriers. *J. Control. Release* **121**, 3–9 (2007).
- [5] G. F. Christopher, J. Bergstein, N. B. End, M. Poon, C. Nguyen and S. L. Anna, Coalescence and splitting of confined droplets at microfluidic junctions. *Lab. Chip.* **9**, 1102–1109 (2009).
- [6] G. F. Christopher, N. Nadia Noharuddin, Joshua A. Taylor, and Shelley L. Anna, Experimental observations of the squeezing-to-dripping transition in T-shaped microfluidic junctions. *Phys. Rev. E.* **78**, 036317 (2008).
- [7] L. Clime, D. Brassard, and T. Veres, Numerical modeling of the splitting of magnetic droplets by multiphase lattice Boltzmann equation. *J. Appl. Phys.* **105**, 07B517 (2009).
- [8] V. Cristini and Y. C. Tan, Theory and numerical simulation of droplet dynamics in complex flows-a review. *Lab. Chip.* **4**, 257–264 (2004).
- [9] T. Cubaud, Deformation and breakup of high-viscosity droplets with symmetric microfluidic cross flows. *Phys. Rev. E.* **80**, 026307 (2009).
- [10] T. Cubaud and C. Ho, Transport of bubbles in square microchannels *Phys. Fluids* **16**(12), 4575–4585 (2004).

- [11] M. de Menech, P. Garstecki, F. Jousse and H. A. Stone, Transition from squeezing to dripping in a microfluidic T-shaped junction. *J. Fluid Mech.* **595**, 141–161 (2008).
- [12] P. Dimitrakopoulos and J. J. L. Higdon, Displacement of fluid droplets from solid surfaces in low-Reynolds-number shear flows. *J. Fluid Mech.* **336**, 351–378 (1997).
- [13] P. Dimitrakopoulos and J. J. L. Higdon, On the displacement of three-dimensional fluid droplets from solid surface in low-Reynolds-number shear flows. *J. Fluid Mech.* **377**, 189–222 (1998).
- [14] P. Dimitrakopoulos and J. J. L. Higdon, On the displacement of three-dimensional fluid droplets adhering to a plane wall in viscous pressure-driven flows. *J. Fluid Mech.* **435**, 327–350 (2001).
- [15] P. Dimitrakopoulos, Interfacial dynamics in Stokes flow via a three-dimensional fully-implicit interfacial spectral boundary element algorithm. *J. Comp. Phys.* **225**, 408–426 (2007).
- [16] M. M. Dupin, I. Halliday and C. M. Care, Simulation of a microfluidic flow-focussing device. *Phys. Rev. E.* **73**, 055701(R) (2006).
- [17] P. Garstecki, M. J. Fuerstman, H. A. Stone and G. M. Whitesides, Formation of droplets and bubbles in a microfluidic T-junctions : scaling and mechanism of break-up. *Lab. Chip.* **6**, 437–446 (2006).
- [18] H. Gu, M. H. G. Duits, F. Mugele, Droplet formation and merging in two-phase flow microfluidics. *Int. J. Mol. Sci.* **12**, 2572-2597 (2011).
- [19] S. Guido, Shear-induced droplet deformation: Effects of confined geometry and viscoelasticity. *Current Opinion in Colloid and Interface Science* **16**, 61–70 (2011).

- [20] D. J. E. Harvie, J. J. Cooper-White and M. R. Davidson, Deformation of a viscoelastic droplet passing through a microfluidic contraction. *J. Non-Newtonian Fluid Mech.* **155**, 67–79 (2008).
- [21] W. B. Kolb, R. L. Cerro, Coating the inside of a capillary of square cross section. *Chem. Eng. Sci.* **46**, 2181–2195 (1991).
- [22] W. B. Kolb, R. L. Cerro, The motion of long bubbles in tubes of square cross section. *Phys. Fluids A* **5**, 1549–1557 (1993).
- [23] S. Kuriakose and P. Dimitrakopoulos, Motion of an elastic capsule in a square microfluidic channel. *Phys. Rev. E* **84**, 011906 (2011).
- [24] E. Lac and J. D. Sherwood, Motion of a drop along the centerline of a capillary in a pressure-driven flow. *J. Fluid Mech.* **640**, 27–54 (2009).
- [25] A. M. Leshansky, S. Afkhami, M.C. Jullien, and P. Tabeling, Obstructed breakup of slender drops in a microfluidic T junction. *Phys. Rev. Lett.* **108**, 264502 (2012).
- [26] J. Liu and N.T. Nguyen, Numerical simulation of droplet-based microfluidics—A review. *Micro and Nanosystems* **2**(3), 193–201 (2010).
- [27] H. Liu and Y. Zhang, Droplet formation in microfluidic cross-junctions. *Phys. Fluids* **23**, 082101 (2011).
- [28] H. Liu and Y. Zhang, Electrochemical and flow characterization of a direct methanol fuel cell. *J. Power Sources* **134**, 33–40 (2004).
- [29] J. Magnaudet, S. Tagaki and D. Legendre, Drag, deformation and lateral migration of a buoyant drop moving near a wall. *J. Fluid Mech.* **476**, 115–157 (2003).
- [30] J. L. Mercier, F. M. da Cunha, J. C. Teixeira and M. P. Scofield, Influence of enveloping water layer on the rise of air bubbles in Newtonian fluids. *J. Appl. Mech.* **41**(1), 29–35 (1974).

- [31] M. Minale, S. Caserta and S. Guido, Microconfined shear deformation of a droplet in an equiviscous non-Newtonian immiscible fluid: Experiments and modeling. *Langmuir* **26**(1), 126–132 (2011).
- [32] M. K. Mulligan and J. P. Rothstein, Scale-up and control of droplet production in coupled microfluidic flow-focussing geometries. *Microfluid. Nanofluid.* **13**(1), 65–73 (2012).
- [33] M. A. Nilsson, J. P. Rothstein, The effect of contact angle hysteresis on droplet coalescence and mixing *J. Colloid Interf. Sci.* **363** 646–654 (2011).
- [34] W. L. Olbricht, Pore-scale prototypes of multiphase flow in porous media *Ann. Rev. Fluid Mech.* **28** 187–213 (1996).
- [35] J. M. Rallison, A numerical study of the deformation and burst of a viscous drop in general shear flows. *J. Fluid Mech.* **109**, 465–482 (1981).
- [36] J. M. Rallison and A. Acrivos, A numerical study of the deformation and burst of a viscous drop in an extensional flow. *J. Fluid Mech.* **89**(1), 191–200 (1978).
- [37] M. Shapira and S. Haber, Low Reynolds number motion of a droplet in shear flow including wall effects. *Int. J. Multiph. Flow* **16**, 305–321 (1990).
- [38] X. C. Solvas and A. deMello, Droplet microfluidics: recent developments and future applications. *Chem. Commun.* **47**, 1936–1942 (2011).
- [39] H. Song, J. D. Tice and R. F. Ismagilov, A microfluidic system for controlling reaction networks in time. *Angew. Chem. Int. Ed. Engl.* **42**(7), 768–772 (2003).
- [40] F. Takemure, J. Magnaudet and P. Dimitrakopoulos, Migration and deformation of bubbles rising in a wall-bounded shear flow at finite Reynolds number. *J. Fluid Mech.* **634**, 463–486 (2009).
- [41] Y. C. Tan, V. Cristini and A. P. Lee, Monodispersed microfluidic droplet generation by shear focusing microfluidic device. *Sensors and Actuators B: Chemical* **114**(1), 350–356 (2005).

- [42] G. I. Taylor, The viscosity of a fluid containing small drops of another fluid *Proc. Roy. Soc. A* **138**, 41–48 (1932).
- [43] G. I. Taylor, The formation of emulsions in definable fields of flow *Proc. Roy. Soc. A* **146**, 501–523 (1934).
- [44] T. Thorsen, R. W. Roberts, F. H. Arnold and S. R. Quake, Dynamic Pattern Formation in a Vesicle-Generating Microfluidic Device. *Phys. Rev. Lett.* **86**(18), 4163-4166 (2001).
- [45] T. M. Tsai and M. J. Miksis, Dynamics of a drop in a constricted capillary tube. *J. Fluid Mech.* **274**, 197–217 (1994).
- [46] P. B. Umbanhowar, V. Prasad, and D. A. Weitz, Monodisperse emulsion generation via drop break off in a coflowing stream. *Langmuir* **16**, 347–351 (2000).
- [47] Y. Wang and P. Dimitrakopoulos, A three-dimensional spectral boundary element algorithm for interfacial dynamics in Stokes flow *Phys. Fluids* **18**, 082106 (2006).
- [48] Y. Wang and P. Dimitrakopoulos, Low-Reynolds-number droplet motion in a square microfluidic channel. *Theor. Comput. Fluid Dyn.* **26**(1-4), 361–379 (2012).
- [49] Z. Z. Wong and J. L. Bull, Vascular bubbles and droplets for drug delivery. *J. Drug Del. Sci. Tech.* **21**(5), 2011.
- [50] L. Wu, M. Tsutahara, L. S. Kim and M. Ha, Three-dimensional lattice Boltzmann simulations of droplet formation in a cross-junction microchannel. *Int. J. Multiphas. Flow.* **34** 852–864 (2008).
- [51] C.S. Yih, Fluid Mechanics, West River Press, (1980).
- [52] G. K. Youngren and A. Acrivos, On the shape of a gas bubble in a viscous extensional flow *J. Fluid Mech.* **76**(3), 433–442 (1976).

- [53] M. Zagnoni, C. N. Baroud and J. M. Cooper, Electrically initiated upstream coalescence cascade of droplets in a microfluidic flow. *Phys. Rev. E.* **80**, 046303 (2009).
- [54] A. Z. Zinchenko and R. H. Davis, A multipole-accelerated algorithm for close interaction of slightly deformable drops. *J. Comp. Phys.* **207**, 695–735 (2005).

Vita

Navadeep Boruah was born in Assam, India. He entered the Department of Chemical Engineering at the National Institute of Technology at Warangal, India in July 2002. He graduated in June 2006 receiving his Bachelor of Technology degree in Chemical Engineering. After receiving his Bachelor's, he joined the Indian Oil Corporation Limited and held various roles in the company between August 2006 and July 2010. He moved to US in August 2010 and enrolled in the graduate program of the Department of Chemical and Biomolecular Engineering at the University of Maryland at College Park. In January 2011 he joined the Bio-Fluid Dynamics Laboratory and conducted research in the area of computational fluid dynamics under the guidance of Dr. Panagiotis Dimitrakopoulos until his graduation. His graduate work involved the study of the interfacial dynamics of droplets in intersecting flows of microfluidic junctions. In December 2012 he received a Master of Science degree in Chemical Engineering with thesis titled "Droplet Dynamics in Microfluidic Junctions".